The Dissertation Committee for Matthew R. Hiatt

certifies that this is the approved version of the following dissertation:

Characterizing hydrological connectivity and channel-island processes in river deltas to inform coastal restoration

Committee:

Paola Passalacqua, Supervisor

David Mohrig

Ben R. Hodges

David Maidment

Charles Werth

Characterizing hydrological connectivity and channel-island processes in river deltas to inform coastal restoration

by

Matthew R. Hiatt, B.S.C.E, M.S.E

Dissertation

Presented to the Faculty of the Graduate School of

The University of Texas at Austin

in Partial Fulfillment

of the Requirements

for the Degree of

Doctor of Philosophy

The University of Texas at Austin

May 2016

Acknowledgments

Firstly, I would like to thank my supervisor, Dr. Paola Passalacqua, for her guidance, support, and friendship. I have had a wonderful experience as a graduate student and she is one of main the reasons why. I would also like to thank the members of my dissertation committee. Dr. Ben Hodges has been particularly helpful and supportive in the development of the numerical modeling portions of my research and I am grateful for our many productive conversations. Dr. David Mohrig has been a joy to work with and he has challenged me to broaden my research scope. I thank Dr. David Maidment for lending his expertise and great insights. It has been great to have Dr. Charlie Werth involved with my research and I appreciate his enthusiasm.

I thank all of the outstanding students, postdocs, friends, and family who have made grad school wonderful experience. I would like to thank Dave Rounce, Harish Sangireddy, Alicia Sendrowski, Fernando Salas, Rachel Chisolm, Man Liang, Anastasia Piliouras, John Shaw, Wayne Wagner, Nathanael Geleynse, Brandon Minton, Anna Kladzyc, Corey Van Dyk, Richard Carothers, Eric C. Cherasia, Tom Wessling and many others for their friendship and advice. My parents and family have been great and I appreciate their support over the years. My fiancée, Alexandra Garcia, has provided tremendous support throughout my PhD and I feel very lucky to have her by my side. Last, but not least, I thank my dog, Tank, for being awesome.

I acknowledge the funding support of the National Science Foundation Graduate Research Fellowship (Grant No. DGE-1110007) and the Environmental & Water Resources Engineering department at UT-Austin.

Characterizing hydrological connectivity and channel-island processes in river deltas to inform coastal restoration

Matthew R. Hiatt, Ph.D.

The University of Texas at Austin, 2016

Supervisor: Paola Passalacqua

River deltas are highly dynamic environments that are made up of distributary channels and interdistributary islands. This dissertation uses field observations at the Wax Lake Delta (WLD) and numerical modeling to improve the understanding of hydrological connectivity and coupled channel-island processes in river deltas, and to inform coastal restoration strategies. The studies presented here show that channel-island hydrological connectivity is a key element of delta dynamics. In the first study, acoustic Doppler current profiler measurements show that 23-54% of the water flux entering the WLD channel network is allocated to the interiors of the deltaic islands, indicating that the islands are important elements of the hydrological network. A dye tracer experiment reveals that travel times within the deltaic islands are significantly longer than that of the distributary channels. Based on these observations, a framework for analyzing hydrological connectivity in coastal river deltas is developed. The second study is an investigation of the controls on hydrological connectivity, residence time distributions, and nitrate removal in a river delta channel-island complex using numerical modeling of the hydrodynamics and a simple model for nitrate removal. The modeling results show that channel-island hydrological connectivity and water residence time distributions are strongly controlled by hydraulic roughness due to vegetation within the

islands. The modeled fractional nitrate removals range from ∼0–87% depending on river discharge, hydraulic roughness, and tidal influences, which compare well with the 47–91% nitrate removal estimated from field data at WLD. In the third study, field measurements and numerical modeling results are used characterize network-scale flow partitioning and water residence time distributions at WLD. The influences of the spring-neap and daily tidal cycles are shown to have a limited influence on the partitioning of discharge through the delta network. Spatial heterogeneity in local water residence times is due to the structure of the delta network and the local channel-island hydrological connectivity. The results from the three studies presented in this dissertation have important implications for understanding the physical controls on hydrological connectivity in river deltas and the management of coastal restoration projects.

Table of Contents

List of Tables

List of Figures

Chapter 1: Introduction

1.1 Motivation

River deltas are considered to be fragile environments that are vulnerable to anthropogenic disturbance, sea level rise, and natural subsidence [*Ericson et al.*, 2006]. Though fragile, deltas are highly productive and house close to half a billion human inhabitants on delta plains worldwide [*Tessler et al.*, 2015]. Not only do deltaic floodplains house large, dense populations, they have significant ecological, economical, and agricultural value [*Ericson et al.*, 2006]. In recent years, an increased interest in the study of river delta surface and subsurface processes has been brought forth by a need to mitigate problems associated with coastal wetland loss [*Day Jr. et al.*, 2000, 2007], increased nutrient export to receiving waters [*Rabalais et al.*, 1996; *Diaz and Rosenberg*, 2008; *Rivera-Monroy et al.*, 2010], and anthropogenic activities such as hydrocarbon extraction [*Morton et al.*, 2002] and the construction of dams [*Syvitski et al.*, 2009].

One of the most telling examples of these environmental issues is the Mississippi River Delta. Substantial land loss has occurred in coastal Louisiana and estimates of wetland loss are reported as being greater than 4900 km^2 [*Day Jr. et al.*, 2007]. Since the 1950s, the nitrogen and phosphorous load in Mississippi River water has significantly increased [*Rabalais et al.*, 1996; *Diaz and Rosenberg*, 2008], which directly contributes to the development of the Gulf of Mexico hypoxic zone [*Rabalais et al.*, 2007; *Turner et al.*, 2008; *Rabalais et al.*, 2010; *Rivera-Monroy et al.*, 2010]. The Gulf of Mexico hypoxic zone is one of the largest in the world and

had an average extent of 16,700 km^2 from 2000–2007 [*Turner et al.*, 2008]. While climate variability and ocean dynamics influence the Gulf of Mexico hypoxic extent [*Rabalais et al.*, 2002b], the temporal increase in the size of the hypoxic zone has been correlated to increases in nutrient loading [*Rabalais et al.*, 2002c; *Scavia et al.*, 2003; *Turner et al.*, 2006]. Despite their apparent vulnerability to these environmental factors, river deltas adapt to changes in the environment [*Muto*, 2001] and form naturally organized, self-maintaining dynamic systems [*Paola et al.*, 2011].

Delta growth is a balancing act among vertical accretion via sediment deposition, organic matter production, and relative sea level rise (the combination of subsidence and eustatic sea level rise) [*Wright*, 1977; *Roberts et al.*, 1997]. Coastal Louisiana wetlands have been lost [*Day Jr. et al.*, 2007] at rates as high as 100 km^2 per year [*Gagliano et al.*, 1984], and that trend is expected to continue due to human activities [*Gagliano et al.*, 1984; *Boesch et al.*, 1994; *Day Jr. et al.*, 2000]. Since coastal river deltas are typically low-gradient systems, it seems obvious that a small rise in sea level would drown a large area of the delta surface. However, deltas have been shown to be rather resilient to relative sea level rise [*Muto*, 2001; *Carvajal et al.*, 2009; *Paola et al.*, 2011] if they are supplied with sufficient sediment from the river. It is natural then to ask why are coastal wetlands disappearing? For coastal Louisiana, most research points to the isolation of the Mississippi River from its floodplain due to extensive leveeing as the major source of the accelerated wetland degradation [*Boesch et al.*, 1994; *Day Jr. et al.*, 2000; *Paola et al.*, 2011]. Leveeing cuts off hydrological connections to the delta plain and impedes the ability of the river to nourish its floodplain with the sediment needed to keep pace with relative sea level rise and erosion. Decreased sediment loadings due to upstream damming is also considered a factor in wetland drowning [*Syvitski et al.*,

2009; *Paola et al.*, 2011]. The extraction of fluid from the subsurface has also accelerated subsidence rates in the region [*Morton et al.*, 2002]. The presence of dredged industrial canals also contributes to coastal wetland loss [*Day Jr. et al.*, 2000] and decreases water retention time [*Templet and Meyer-Arendt*, 1998].

Many researchers have proposed engineered river diversions as a strategy for mitigating wetland loss and restoring coastal ecosystems [*Boesch et al.*, 1994; *Day Jr. et al.*, 2000, 2007; *Kim et al.*, 2009; *Allison and Meselhe*, 2010; *Paola et al.*, 2011]. Engineered river diversions aim to reconnect the channel and its floodplain in order to increase sediment deposition and land-growth [*Day Jr. et al.*, 2000; *Kim et al.*, 2009; *Allison and Meselhe*, 2010; *Paola et al.*, 2011]. The concept behind restoration is to allow the system to naturally create and restore its own wetlands by creating controlled diversion points where water and sediment are delivered onto drowned wetlands [*Paola et al.*, 2011]. Currently implemented diversions have been shown to successfully accumulate sediment and develop subaerial land features [*Kolker et al.*, 2012]. The mass balance model of *Kim et al.* [2009] showed that under a relative sea-level rise of 7 mm yr^{-1} and current rates of sediment delivery, 700–900 km^2 of new land could be built by two river diversions on the lower Mississippi River over the course of 100 years.

Delta restoration through river diversion has important environmental and economic implications. For example, the Mississippi River Delta produces \$12–14 billion in ecosystem benefit (e.g., fresh water, fish, oil, carbon sequestration, nutrient regulation) each year [*Batker et al.*, 2010] and attenuates storm surges from hurricanes [*Barbier et al.*, 2013], preventing significant damage to coastal cities. In the US, coastal wetlands are estimated to prevent \$23.2 billion per year worth of storm protection [*Costanza et al.*, 2008]. Louisiana's Comprehensive Master

Plan for a Sustainable Coast is a multi-billion dollar effort to restore and protect the future of Louisiana's coastal areas comprising river diversions, levee and canal enhancements, and ecological restoration efforts [*Louisiana Coastal Protection and Restoration Authority*, 2012]. In 2015, estimated spending is $725 million on restorative construction and maintenance alone. The plan was developed and is continually updated with the best information available from science and engineering to ensure sustainable practices in restoration and engineered projects affecting the coast. Comprehensive plans like Louisiana's Master Plan encourage scientific research to engage and influence engineering projects that are currently underway.

The prediction of how a restored delta would evolve is not currently known [*Paola et al.*, 2011]. One element requiring attention is hydrological exchange between the channels and islands (or wetlands) in river deltas, which is not well-understood. This exchange is important because it is a vehicle for water, sediment, and nutrient delivery to the delta plain, which is important for land-building and nutrient processes. Large-scale controlled diversions also significantly alter the freshwater hydraulic residence time and nutrient dynamics for coastal systems [*Rivera-Monroy et al.*, 2010]. Deltaic islands and their wetlands serve as important nutrient sinks that reduce the impact of excess nutrient loading on downstream ecosystems [*Luu et al.*, 2012; *Henry and Twilley*, 2014]. Since water residence time is a major factor in determining the nutrient removal capacity of coastal systems [*Nixon et al.*, 1996; *Yu et al.*, 2006; *Rivera-Monroy et al.*, 2010], estimates of the system-scale distribution of water residence times are needed to quantify the potential of engineered river diversions in reducing nutrient export [*Rivera-Monroy et al.*, 2010]. Therefore, improving the understanding of the processes

that modulate water fluxes from distributary channels to the deltaic islands is of great value for the evaluation of restorative river diversion projects.

The reconnection of the channel with the delta plain for restoration purposes lends itself well to analysis within the framework of hydrological connectivity. Hydrological connectivity describes the water-mediated transport of environmental constituents (e.g., sediment, nutrients, organisms, solutes, etc.) through various components of a landscape [*Pringle*, 2003; *Lane et al.*, 2004; *Bracken et al.*, 2013]. Thinking in terms of hydrological connections and their associated fluxes can aid in assessing the processes controlling complex hydrological systems. Although hydrological connectivity is an area of active research for tributary systems [*Bracken et al.*, 2013; *Fryirs*, 2013], less attention has been paid to river delta distributary networks. The channel-floodplain connectivity in tributary systems is integral to sediment transport and deposition [*Walling et al.*, 1998; *Dunne et al.*, 1998; *Day et al.*, 2008; *Trigg et al.*, 2012], nutrient transport [*Tockner et al.*, 1999; *Noe et al.*, 2013], and vegetation dynamics [*Bornette et al.*, 1998; *Pongruktham and Ochs*, 2015]. Similar processes are likely important in river deltas, as well, but the physics of hydrological connectivity of delta networks has not been formally addressed. Since sediment and nutrients are transported by water flux, an understanding of the dynamics of water partitioning in river delta networks is important for estimations of nutrient export and sediment transport.

The goals of the research presented in this dissertation are to (i) characterize and quantify hydrological connectivity in coastal river deltas, (ii) analyze the environmental controls on hydrological connectivity, water residence time distributions, and nitrate removal in a deltaic channel-island complex, (iii) and investigate the influence of environmental forces on network-scale flow partitioning and water

residence time distributions in a natural river delta. This dissertation deepens the current state of knowledge on the ecological and morphological development of deltaic systems through the identification of the importance of hydrological connectivity and coupled channel-island processes. The links among hydrological connectivity, delta hydraulics, residence time distributions, and nutrient removal in river deltas are quantified in this dissertation and the influence of these factors on delta evolution is discussed. The results and conclusions presented in this dissertation have important implications for the design and management of coastal restoration projects.

1.2 Research Questions

This dissertation addresses the following research questions and discusses the relevance to the design and management of coastal restoration projects.

1. How is water partitioned among channels and islands in a river delta network?

2. How does the hydrological connectivity between delta channels and islands influence channel-island hydraulics, water residence time distributions, and nitrate removal? What are the environmental controls on hydrological connectivity in river deltas?

3. How does the structure of the delta network influence network-scale flow partitioning and water residence time distributions at Wax Lake Delta? Do tides influence the flow partitioning?

1.3 Hypotheses

The following hypotheses are tested:

1. *Interdistributary islands convey more water flux to the bay than the distributary channels.* The hydrological connectivity between distributary channels and interdistributary islands is evidenced in significant water delivery from the channels to the island interiors. Tides, wetland vegetation, and upstream river discharge act to modulate the connectivity between the channels and the islands. Water is fluxed to the interdistributary islands over the range of values in the upstream hydrograph. The relative hydraulic roughness between the channel and the island is a stronger control on hydrological connectivity than river discharge and tidal influences.

2. *The water residence time distribution (RTD) for the delta network is controlled by the amount of water entering interdistributary areas.* Travel times within the islands are longer relative to travel times within the channels. The RTD is controlled by the relative hydraulic roughness between the channel and the island, river discharge, and tidal amplitude. Nitrate removal occurs within deltaic islands and the RTD can predict the fractional nitrate removal at the channel-island complex scale. Tides lengthen the RTD and increase nitrate removal within the deltaic islands.

3. *Network structure and channel-island hydrological connectivity control the flow partitioning and water residence time distribution at Wax Lake Delta.* The network-scale partitioning of water is not significantly altered by fluctuations in river discharge and tides. Spring tides act to store water on the

delta plain while neap tides flush water from the system, which results in higher discharges through the delta network than during spring tides.

1.4 Outline

This dissertation is organized as follows. Chapter 2 presents a review of the literature concerning the above research questions and points out the deficiencies in the present state of knowledge. The hydrological connectivity between distributary channels and interdistributary island at WLD is presented in Chapter 3. A discussion of the influences of hydrological connectivity on water travel times through a channel-island complex is also addressed and a novel framework for analyzing hydrological connectivity in river deltas is developed. Chapter 4 contains an analysis of the controls on hydrological connectivity, water residence time distributions, and nitrate removal in a river delta channel-island complex. Network-scale flow partitioning and water residence time distributions are calculated in Chapter 5. Finally, Chapter 6 contains a summary of the contributions of this dissertation and provides recommendations for future work.

Chapter 2: Background

2.1 Hydrological connectivity and channel-island exchange

Hydrological connectivity refers to both the physical connections among landscape components and to the environmental fluxes across those connections. *Bracken et al.* [2013] define structural connectivity as the spatial arrangement of hydrological pathways that connect various components of a landscape and process-based connectivity as the processes that modulate the dynamics of fluxes across those connections. In tributary systems, hydrological connectivity is an area of active research [*Tetzlaff et al.*, 2007; *Bracken and Croke*, 2007; *Bracken et al.*, 2013; *Fryirs*, 2013], but there has not been any formal development of hydrological connectivity in river delta networks. In river networks, the hydrological connectivity is key in understanding the delivery of sediment to the floodplain [*Walling et al.*, 1998; *Day et al.*, 2008; *Fryirs*, 2013] and for nutrient dynamics [*Tockner et al.*, 1999; *Noe et al.*, 2013]. A large body of work exists dealing with the so-called 'sediment delivery problem' [*Walling*, 1983], which questions the fate of sediments within the river basin, which is often addressed through sediment budgets [*Walling*, 1983; *Dunne et al.*, 1998; *Fryirs et al.*, 2007].

Recognizing that channel-floodplain connectivity is a key component of the sediment delivery problem, *Fryirs* [2013] introduced the framework of hydrological disconnectivity to characterize spatial and temporal changes in the erosion and deposition of sediment within tributary systems. The allocation of water and sediment within deltaic systems is also of a critical relevance because islands formed

by sediment deposition comprise the architecture of new land on the delta plain [*Edmonds and Slingerland*, 2007; *Edmonds et al.*, 2011a]. Thus, an understanding of the hydrological connections and the fluxes across them in river delta networks is an important precursor to understanding sediment and nutrient delivery, which informs the management of restored wetlands through river diversions and the assessment of vulnerable wetland systems [*Larsen et al.*, 2012].

Previous work on environmental transport in river deltas has studied in isolation one of two landscape features: the distributary channels or the interdistributary islands. Studies on the channel network have often focused on topology [*Smart and Moruzzi*, 1972; *Morisawa*, 1985; *Jerolmack and Swenson*, 2007; *Edmonds et al.*, 2011a], bifurcation dynamics [*Bolla Pittaluga et al.*, 2003; *Edmonds and Slingerland*, 2007; *Sassi et al.*, 2013], and sediment transport [*Syvitski et al.*, 2005; *Syvitski and Saito*, 2007; *Nittrouer et al.*, 2008; *Shaw et al.*, 2013; *Sassi et al.*, 2013]. The work within islands has been focused on geometry [*Edmonds et al.*, 2011a; *Passalacqua et al.*, 2013] and island biogeochemistry [*Henry and Twilley*, 2014]. The hydrological connectivity between channels and islands in delta systems has not been addressed in the literature.

Hydrological connectivity controls the frequency, magnitude, and duration of inundation of delta islands, which facilitates the transport of sediment and nutrients to the island interiors. External forces such as upstream river discharge, tides, and wind all play a role in the hydrological connectivity of the delta system. Modeling results have shown that water is indeed exchanged between distributary channels and islands [*Liang et al.*, 2015] in river deltas, but the magnitude and direction of this exchange has not been quantified or validated. Thus, measurements of hydraulic fluxes to, within, and out of interdistributary islands under various

environmental settings (riverine input, tidal conditions, and wind conditions) serve as an important advancement for the understanding of river delta dynamics. Field measurements can only represent a subset of environmental conditions, thus numerical modeling supported by robust field measurements must be employed to cover the spectrum of scenarios. This dissertation highlights the importance of channel-island coupled processes in the propagation of fluxes through a delta network, which has implications for the evaluation and management of restored river deltas formed by river diversions.

2.2 Water residence time distributions and nutrient removal in coastal systems

Eutrophication is a growing problem in coastal areas around the globe caused by increases in dissolved reactive nitrate and phosphorous concentrations delivered to coastal zones [*Rabalais et al.*, 2002a; *Diaz and Rosenberg*, 2008; *Turner et al.*, 2008]. Eutrophication has led to a degradation in water quality, hypoxia, and harmful algal blooms in coastal areas around the globe [*Heisler et al.*, 2008]. The rapid acceleration of size and severity of hypoxic zones since the 1950s [*Rabalais et al.*, 1996] has caused mass kills of aquatic species [*Rabalais et al.*, 2002a; *Zhang et al.*, 2010], declines in coastal fisheries [*Rosenberg*, 1985], and habitat loss [*Diaz and Rosenberg*, 2008; *Zhang et al.*, 2010]. Increases in nitrate loading also increase risk to human health from harmful algal blooms [*Diaz and Rosenberg*, 2008; *Rivera-Monroy et al.*, 2010]. A well-documented case is the Gulf of Mexico hypoxic zone, which is one of the largest in the world and its extent averaged 16,700 km^2 from 2000–2007 [*Turner et al.*, 2008]. While climate variability and ocean dynamics influence the Gulf of Mexico hypoxic extent [*Rabalais et al.*, 2002b], the

temporal increase in the size of the hypoxic zone has been correlated to increases in nutrient loading [*Rabalais et al.*, 2002c; *Scavia et al.*, 2003; *Turner et al.*, 2006]. Coastal eutrophication is a major economic and environmental issue and reducing the nutrient export to receiving water via nutrient cycling in coastal wetlands may help partially mitigate the problem [*Mitsch et al.*, 2001; *Turner et al.*, 2008; *Rivera-Monroy et al.*, 2010].

Coastal systems including wetlands, river deltas, and estuaries have the potential to mitigate increased nutrient loading to receiving waters by acting as buffers that reduce impact on downstream ecosystems [*Lane et al.*, 2003; *DeLaune et al.*, 2005; *Rivera-Monroy et al.*, 2010; *Luu et al.*, 2012]. For example, by analyzing the nitrogen and phosphorus budgets at the Red River Delta in northern Vietnam, *Luu et al.* [2012] showed that the delta is efficient at retaining these nutrients and protecting against the eutrophication of receiving waters. Denitrification is a major biochemical pathway for the removal of nitrogen from coastal systems [*Dettmann*, 2001] and has been observed in systems receiving diverted river water [*Lane et al.*, 2003; *DeLaune et al.*, 2005; *Yu et al.*, 2006]. Other pathways for nitrogen removal include plant uptake, burial [*Smith et al.*, 1985], fixation [*Howarth et al.*, 1988], mineralization [*Zak and Grigal*, 1991], nitrification [*Mitsch and Gosselink*, 1993], and annamox [*Erler et al.*, 2008]. In coastal Louisiana, 10 million ha of wetlands must be created or restored to reduce nutrient export to a level that would significantly alleviate the effects of the Gulf's hypoxic zone [*DeLaune et al.*, 2005]. Thus, the coastal restoration effort to mitigate land loss and increased nutrient loading are inevitably connected. Large-scale diversions can significantly alter water residence times and nutrient dynamics [*Rivera-Monroy et al.*, 2010].

At the system scale, water residence time distribution (RTD) [*Nixon et al.*,

1996; *Dettmann*, 2001; *Yu et al.*, 2006] and loading [*Lane et al.*, 2004; *Rivera-Monroy et al.*, 2010] are major controls on the nutrient removal capacity of a coastal system. High concentrations of nitrate (>100 μM) are found in Mississippi River waters and significant nutrient removal occurs in regions subject to such concentrations [*Rivera-Monroy et al.*, 2010; *Henry and Twilley*, 2014], since nitrate removal is dependent on loading rate [*Lane et al.*, 2004]. *Henry and Twilley* [2014] measured N_2 fluxes at Wax Lake Delta and found that denitrification increases with NO_3^- concentration and soil organic matter content. They conclude that river deltas have the capability to remove nitrate and reduce export to receiving waters. The model of the Davis Pond river diversion in coastal Louisiana of *Yu et al.* [2006] showed 42±2.5% and 95±0.5% nitrate removal for residence times of one and five days, respectively. Although local measurements of nutrient removal rates and water velocity exist, there remains a lack of *in situ* measurements of system-scale RTD in coastal Louisiana [*Rivera-Monroy et al.*, 2010]. In addition, there remains the question of how the RTDs of distinct system components influence the RTD of the large-scale system [*Rivera-Monroy et al.*, 2010]. By investigating water fluxes in distributary channels, within the interdistributary island wetlands, and through the entire network at WLD, this dissertation provides the first system-scale estimates of the RTD in a coastal river delta. The RTDs generated in this dissertation are subsequently used to estimate the nitrate removal capacity of a deltaic channel-wetland complex.

2.3 Network-scale flow partitioning

Many of the world's large rivers meet their receiving waters through river deltas composed of a network of distributary channels and interdistributary islands [*Syvit-*

ski and Saito, 2007]. Water flow distributes sediment [*Syvitski et al.*, 2005] and nutrients among the delta channels and islands [*Hiatt and Passalacqua*, 2015], as well as to the receiving basins [*Falcini et al.*, 2012], and the allocation of flow provides a framework for the routing of environmental fluxes through and within the network. Hydrological connectivity also plays a role in the frequency and magnitude of inundation of the island interiors [*Geleynse et al.*, 2015], which facilitates transport into the islands. Overbank deposition is an important element of the land-building mechanisms of river deltas [*Roberts*, 1997], thus the delivery of sediment to the island interiors is essential for the maintenance of the delta platform [*Edmonds et al.*, 2011a]. Therefore, a characterization of the network-scale flow patterns at a prograding delta like WLD would provide a useful benchmark for the development of predictive models of deltaic processes.

The partitioning of water and sediment at single river bifurcations has been extensively studied [*Slingerland and Smith*, 1998; *Zolezzi et al.*, 2006; *Bertoldi and Tubino*, 2007; *Kleinhans et al.*, 2007; *Hoyal and Sheets*, 2009; *Kleinhans and Hardy*, 2013] but partitioning at the network scale is still an area of active research [e.g., *Sassi et al.*, 2011]. The identification of spatial patterns in water discharge may give insight into the functioning of the delta network and its role in the evolution of the delta morphology. Since water carries sediment through the network, an understanding of how water is partitioned among distributary channels and deltaic islands would provide insight into predictions of delta growth [*Wolinsky et al.*, 2010], which would benefit delta restoration projects [*Kleinhans and Hardy*, 2013].

The partitioning of water carrying nutrients through a delta network is important since the delivery of water through the network likely influences the RTD. The RTD has a significant influence on the nutrient removal capacity of

coastal and wetland systems [*Nixon et al.*, 1996; *Dettmann*, 2001; *Yu et al.*, 2006; *Rivera-Monroy et al.*, 2010], so understanding how flow is partitioned among the distributary channels and interdistributary islands is an important for large-scale estimates of nutrient export/retention in coastal zones. The analysis of network-scale flow partitioning provides novel estimates of network-scale flow partitioning and RTD that has important implications for sediment and nutrient dynamics in river deltas.

Chapter 3: Hydrological connectivity in river deltas: The first-order importance of channel-island exchange

3.1 Introduction

Hydrological connectivity refers to flows of matter and energy (water, sediment, nutrients, etc.) through different components of a landscape [*Tetzlaff et al.*, 2007; *Bracken et al.*, 2013]. Frameworks built on the concept of hydrological connectivity can be useful for understanding the processes that drive landscape maintenance and evolution. For tributary systems, the hydrological connection between the channel and its floodplain plays an important role in sediment transport and deposition [*Walling et al.*, 1998; *Day et al.*, 2008; *Trigg et al.*, 2012], nutrient cycling [*Tockner et al.*, 1999; *Noe et al.*, 2013], and biodiversity and productivity [*Bornette et al.*, 1998; *Pongruktham and Ochs*, 2015]. Although hydrological connectivity in river networks is an area of active research, [e.g., *Bracken and Croke*, 2007; *Ali and Roy*, 2009; *Fryirs*, 2013; *Bracken et al.*, 2013], similar work in coastal river deltas has yet to be developed. *Bracken et al.* [2013] summarize hydrological connectivity within two categories: (1) structural connectivity, which refers to the spatial arrangement of the landscape that controls patterns in flux path-

The text and figures from this chapter are published in this article:
Hiatt, M., and P. Passalacqua (2015), Hydrological connectivity in river deltas: The first-order importance of channel-island exchange, *Water Resour. Res., 51*, 2264–2282, doi: 10.1002/2014WR016149.
The authors contributed in the following percentages to study concept and design, data collection, analysis, and article preparation: M.H. $\{60, 100, 100, 90\%\}$ and P.P. $\{40, 0, 0, 10\%\}$.

ways, and (2) process-based connectivity, which refers to environmental processes that produce the magnitude and direction of those fluxes. This paper investigates hydrological connectivity in river deltas by quantifying the hydrological exchange between channels and interdistributary islands (the deltaic equivalent of the tributary floodplain) and discusses its importance for delta morphology and ecology.

In recent years, an increased interest in the study of the processes controlling delta eco-geomorphology has been brought forth by a need to mitigate problems associated with coastal wetland loss [*Day Jr. et al.*, 2000, 2007], increased nutrient loading to receiving waters [*Turner and Rabalais*, 1994; *Rabalais et al.*, 2002a; *Castro et al.*, 2003], anthropogenic influence and other factors [*Syvitski and Saito*, 2007; *Syvitski et al.*, 2009; *Pethick and Orford*, 2013]. Previous work on river delta surface processes has focused on one of two zones: the distributary channels or the interdistributary islands, which are the subaerial manifestation of delta structure due to sediment deposition [*Edmonds and Slingerland*, 2007; *Edmonds et al.*, 2011a]. Work on the distributary channels has primarily been concerned with the network topology [*Smart and Moruzzi*, 1972; *Morisawa*, 1985; *Edmonds and Slingerland*, 2007; *Jerolmack and Swenson*, 2007; *Edmonds et al.*, 2011a; *Tejedor et al.*, 2014a,b], bifurcation dynamics [*Wright*, 1977; *Bolla Pittaluga et al.*, 2003; *Edmonds and Slingerland*, 2007; *Sassi et al.*, 2013], mouth bar formation [*Edmonds and Slingerland*, 2007; *Rowland et al.*, 2010; *Mariotti et al.*, 2013], and the sediment transport within the channel and to the receiving waters [*Syvitski et al.*, 2005; *Syvitski and Saito*, 2007; *Nittrouer et al.*, 2008; *Shaw et al.*, 2013]. Within the islands, research has been concerned with island geometry [*Edmonds et al.*, 2011a; *Passalacqua et al.*, 2013], wetland vegetation [*Neill and Deegan*, 1986; *Keddy et al.*, 2007; *Carle et al.*, 2013], and the island biogeochemistry [*Henry and Twilley*, 2014]

which has highlighted that deltaic wetlands are zones of significant denitrification able to reduce the nutrient export to receiving waters [*Lane et al.*, 1999, 2003; *DeLaune et al.*, 2005; *Yu et al.*, 2006; *Rivera-Monroy et al.*, 2010; *Henry and Twilley*, 2014]. These studies have focused on either the distributary channels or the interdistributary islands and not on the hydrological connectivity between the two. The role of process-based connectivity in coupling channel and island processes has been ignored in the literature and elements of structural connectivity between channels and islands have yet to be defined.

Hydrological connectivity is a controlling factor on the frequency and degree of inundation of delta islands, bringing water, sediment, and nutrients to the island interiors. Inundation of the interdistributary islands is a function of internal and external forces (such as riverine input, tides, and wind). Feedback mechanisms among internal dynamics of water, sediment and nutrients play a fundamental role in deltas. As such, quantification of environmental fluxes to, within, and out of interdistributary islands under a suite of environmental forces is of a critical relevance to the understanding of processes shaping delta evolution. Furthermore, many researchers have pointed to the isolation of the channel from its floodplain due to levee construction, which can be seen as a form of hydrological (dis)connectivity [*Fryirs*, 2013], as the major factor in the acceleration of deltaic wetland degradation [*Boesch et al.*, 1994; *Day Jr. et al.*, 2000, 2007; *Paola et al.*, 2011]. Engineered river diversions have been proposed as a restoration strategy [*Kim et al.*, 2009; *Allison and Meselhe*, 2010; *Paola et al.*, 2011]. Thus, an understanding of the dynamics of hydrological connections and their associated fluxes in deltaic networks would provide a context for evaluating restored wetlands and assessing the status of vulnerable deltaic systems [*Larsen et al.*, 2012].

The goal of this study is to characterize structural and process-based connectivity in a coastal river delta by measuring water fluxes through the delta network of channels and islands at the Wax Lake Delta (WLD) in coastal Louisiana (Figure 3.1). The rapid formation of WLD since the 1970s with little human influence has made this delta a model for land-building river diversions in the Mississippi Delta region [*Kim et al.*, 2009; *Paola et al.*, 2011]. In order to assess the hydrological connectivity at WLD, we (1) quantify the amount of water delivered to the interdistributary islands, (2) identify internal and external drivers of flow pathways within an interdistributary island by monitoring the propagation of a hydraulic dye tracer, (3) calculate travel times through a channel-island complex, and (4) establish measures of structural and process-based connectivity in coastal river delta environments. The conclusions drawn from these analyses advance the understanding of hydrological connectivity and eco-geomorphology in coastal deltaic systems.

The remainder of the paper is structured as follows. The field site is presented in Section 3.2 followed by a description of the instrumentation and data collection in Section 3.3. Section 3.4 analyzes the velocity cross sections collected along two major distributary channels and within the interdistributary islands, the propagation of the hydraulic dye tracer released on a deltaic island, and travel times through a channel-island complex. Section 3.5 contains a discussion of the results in the context of hydrological connectivity and delta eco-geomorphology and presents a framework for the analysis of hydrological connectivity in coastal delta systems. We state the conclusions of this contribution in Section 3.6.

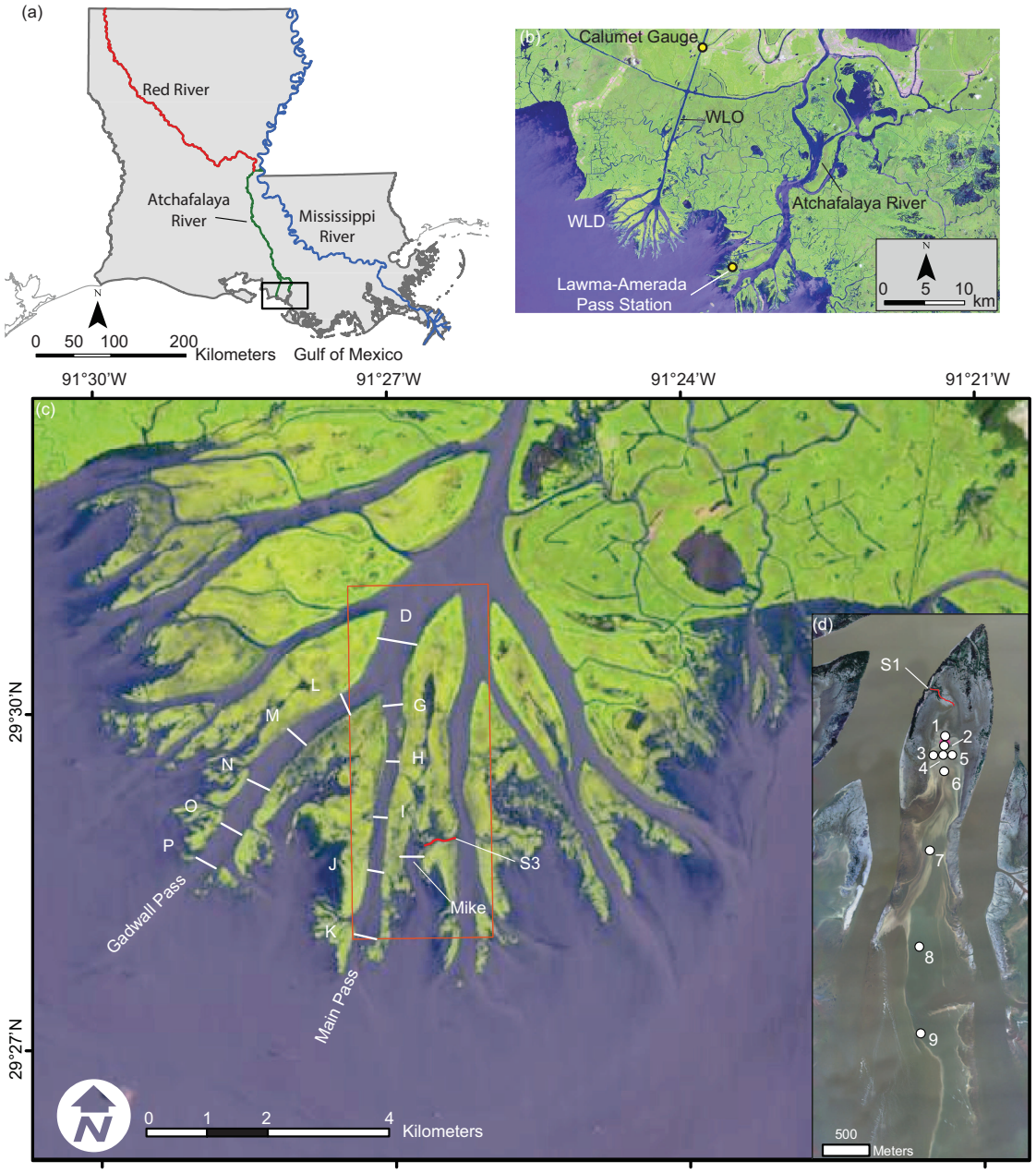

Figure 3.1: (a) Map of Louisiana and the major rivers contributing to the discharge at the Wax Lake Outlet (WLO) and the Wax Lake Delta (WLD). The WLO debouches into the Atchafalaya Bay at WLD and receives its discharge from

Figure 3.1 (cont.): the Atchafalaya River, which is fed by the Red and Mississippi Rivers. (b) The lowermost portion of the Atchafalaya River Basin. The USGS Gauge #07381590 in Calumet, LA is located about 18 km upstream of WLD along the WLO. The NOAA Lawma-Amerada Pass station (NOAA #8764227) is located in the adjacent Atchafalaya delta about 12 km ESE of the study region. (c) Map of the field measurements at Wax Lake Delta. Locations of ADCP transects traversed in Main and Gadwall Passes (06/16/2014–06/29/2014) and on Mike Island (07/23/2012–07/24/2012) are marked. The extent of the S3 channel has been mapped. Image specifications: LANDSAT 8 image from 06/19/2014 at 30 m resolution obtained from the USGS Global Visualization Viewer (available online at http://glovis.usgs.gov/). (d) Sensor locations for the dye tracer study performed on Mike Island from 02/07/2014 through 02/11/2014. The pink hexagon between sites 1 and 2 marks the location of the dye release point. Site S1 is the location of a secondary channel measured on 07/22/2012 and its extent has been mapped. The image is aerial photography from 11/06/2009 with 0.30 m resolution.

3.2 Site Description

WLD is an $O(100\ \mathrm{km}^2)$ delta located in coastal Louisiana (Figure 3.1) at the mouth of the 40-km long Wax Lake Outlet (WLO), which debouches into the Atchafalaya Bay about 140 km WSW of New Orleans. The WLO is a 1941 diversion dredged by the U.S. Army Corps of Engineers in an effort to reduce flooding of the Atchafalaya River [*Fisk*, 1952]. The diversion subsequently carried and deposited sediment, causing the delta to become subaerially emergent in 1973 [*Roberts et al.*, 1997]. The delta has been steadily building land since, making it one of the few deltas formed during an observable time period. Sediment input to WLD is estimated to be 38.4 Mt yr^{-1} with 18% being sand [*Kim et al.*, 2009]. Sand deposition caused most of the WLD's 270 mm yr^{-1} vertical accretion from 1981 to 1997 [*Edmonds et al.*, 2011a] and the deltaic deposit is estimated to be 50–70% medium sand [*Roberts et al.*, 1997]. Mixed semidiurnal microtides (average range of 0.35 m) modulate water levels on the low-gradient delta. The average annual flow

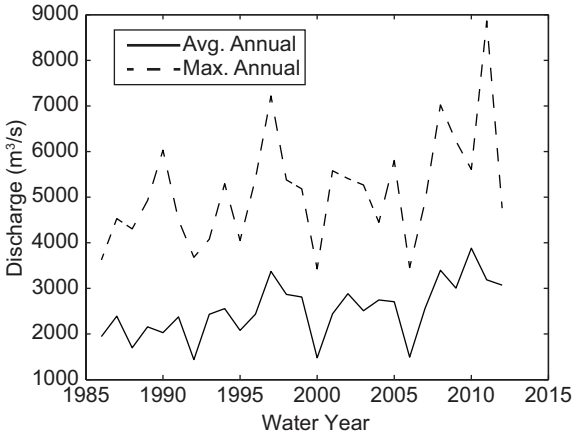

Figure 3.2: Average and maximum annual flows in the Wax Lake Outlet at the USGS Gauge #07381590 in Calumet, LA [*USGS*, 2016]. Average annual flows tend to be 2000 - 3000 m^3/s and annual floods peak above 5000 m^3/s.

in the WLO is 2500 m^3 s^{-1} and the annual flood tends to peak above 5000 m^3 s^{-1} (Figure 3.2). Estimates of delta progradation rate, the rate of land building, and the total subaerially exposed land obtained through remote sensing analysis [*Roberts et al.*, 2003; *Allen et al.*, 2011] and morphodynamic modeling [*Parker and Sequeiros*, 2006] are quite variable among studies. For more complete descriptions of the formation, evolution, and sedimentology of WLD, see the works of *Fisk* [1952], *Roberts et al.* [1997, 2003], and *Shaw et al.* [2013].

The WLD is comprised of channels and partially-inundated interdistributary islands (Figure 3.1). The channel network can be divided into primary (>100 m width) and secondary channels. Primary channels distribute water through the system to the Atchafalaya Bay, while secondary channels connect the primary channels to the inundated island interiors [*Shaw et al.*, 2013]. At the initial bifurcation of WLD, a large flow asymmetry exists and the downstream topology of the two branches differs greatly. The downstream topology of the eastern branch

is characterized by elongated channels with relatively few bifurcations [*Edmonds et al.*, 2011a], while the western branch receives a smaller percentage of the flow and its downstream topology includes shorter channels with more bifurcations and confluences. The islands in the eastern portion tend to have greater rates of lateral and downstream migration as compared to the islands downstream of the western branch of the initial bifurcation [*Shaw et al.*, 2013]. Island levees within 4 km of the delta apex are populated with *Salix nigra* (black willow) and seem to be more stable than those without *Salix nigra* [*Shaw et al.*, 2013]. The low-relief islands are characterized by natural levees that transition from subaerial to subaqueous with increasing distance from the island apices and downstream boundaries that are open to the bay. Levees in both the subaerial and subaquaeous regions are intersected by secondary channels. Near the island apices, vegetation is dense and the elevation is high in comparison to the more bayward portions of the islands, which are deeper and less vegetated.

A pictorial summary of the levee types and their relation to channel-island connectivity is presented in Figure 3.3. In the most upstream portions of the WLD channel network, *Salix nigra* (black willow) is present on the subaerial levees (e.g., Figure 3.3a). Moving downstream, the levees initially remain subaerial (e.g., Figure 3.1c, Figure 3.3b–f). Further downstream, both subaerial and subaqueous levees are observed, with the amount of submerged levees increasing downstream. At the channel mouths, the levees are mostly subaqueous, but less than one meter in depth. Some of the subaqueous levees have dense vegetation (Figure 3.3g), while others are sparsely vegetated (Figure 3.3h). There are multiple secondary channels along the banks of both distributary channels (e.g., Figure 3.3c–f). Secondary channels are present in the subaqueous portion as well. While these observations

refer to the time and conditions at which the pictures were taken, an overall trend of increasing structural connectivity (secondary channels and subaqueous levees) moving towards the bay characterizes WLD.

3.3 Field Data Collection

A field campaign at WLD aimed at capturing the channel-island hydrological connectivity was comprised of three trips spanning from February 2012 to June 2014. We measured (1) flow into and out of interdistributary islands via secondary channel flow, (2) the discharge along two primary channels and the allocation of water to the islands, and (3) the hydraulic behavior of an interdistributary island.

Field measurements of fluxes through hydrological connections prove difficult in deltaic systems where a suite of environmental forces influence the dynamics of the system. Relatively rapid changes in water level due to tides and wind can drastically alter the connectivity at WLD [*Geleynse et al.*, 2015], which is problematic when attempting to quantify connectivity measures. However, the relatively small area of WLD and the microtidal regime make WLD an ideal location to measure fluxes through hydrological connections on a system scale while controlling for water level fluctuations due to tides.

3.3.1 Secondary channel and island discharge measurements

Velocity transects on Mike Island (marked by transects in Figure 3.1c) were measured on 07/23–07/24/2012 during both rising and falling tides. Measurements of flow in secondary channels were made at transects S1 and S3 (Figure 3.1c) on 07/22 and 07/24, respectively, while the Mike transect (Figure 3.1c) was measured

Figure 3.3: Examples of channel-island surface water connectivity at Wax Lake

Figure 3.3 (cont.): Delta. The date on which each photo was taken is in parentheses. Locations are mapped in Figure 3.1c. (a) East bank of transect D (06/19/2014). The vegetated subaerial bank limits hydrological connections to high water events. *Salix nigra* (black willow) line the levees in this region. (b) Mike Island subaerial vegetated levee (06/20/2012). Dense vegetation limits flow exchange over the levee top. (c) A secondary channel on the bank east of the island in the northeast corner of WLD (06/20/2014) with a vegetated flow path. (d) A secondary channel off Main Pass (05/18/2014). Vegetation within the secondary channel can limit connectivity. (e) A secondary channel with partially vegetated banks leading into Mike Island (06/20/2012). (f) A secondary channel with vegetated banks leading into the island in the northeast corner of WLD (05/08/2013). (g) A vegetated subaqueous levee near the east bank of transect J (06/19/2014). (h) The partially vegetated subaqueous levee on the east bank of transect K (06/19/2014).

during both falling and rising tide on 07/23. A 2 MHz RDI StreamPro operating in water mode 12sp (a multi-ping version of water mode 1) [*Mueller et al.*, 2013] was towed across the transects. Each ping was comprised of eight subpings and an ensemble output rate of 1 Hz was maintained. Bin sizes ranged from 0.03 to 0.10 m, depending on the maximum depth of the transect and towing speed ranged from 0.5 to 0.9 m s^{-1}. The transducer sat 0.05 m below the water surface and had a blanking distance of 0.03 m. At least two duplicate transects were traversed at each location. The average discharge measured at the USGS gauge #07381590 [*USGS*, 2016] in Calumet, LA (18 km upstream of the WLD apex) was 1021 m^3 s^{-1} for the duration of the measurements (the discharge at the Calumet station is given for each field trip to give context, but the magnitude is not assumed to be the discharge entering the WLD apex). Water levels averaged every six minutes from the NOAA Lawma-Amerada Pass tide gauge #8764227 [*NOAA*, 2016] were referenced to mean lower-low water datum (MLLW) and used to relate the measured discharges to the tidal cycle.

3.3.2 Distributary channel discharge measurements

Hydrographic surveys were performed in two major distributary channels at WLD from 06/16/2014 to 06/19/2014. A boat-mounted acoustic Doppler current profiler (ADCP) measured velocity transects in both Gadwall and Main Passes. The transects were labeled 'L–P' for Gadwall and 'G–K' for Main (Figure 3.1c). Velocity transects at the feeder channel upstream of the two passes (location D) were also measured. The 2 MHz RDI StreamPro with the long-range upgrade measuring in water mode 12sp was mounted and floated from the bow of the *R/V Bluerunner*. Eight subpings comprised each ping and the data output rate was maintained at 1 Hz. The ADCP transducer sat 0.05–0.06 m below the water surface and had a blanking distance of 0.03 m. The bin size was 0.15–0.20 m, depending on the maximum depth of the transect. Boat speed averaged to about 1.0 m s^{-1}. ADCP transects were collected during both rising and falling tides, and were marked accordingly. Quadruplicate transects were traversed for each measurement, unless otherwise noted, to ensure precise results in accordance with USGS standards [*Mueller et al.*, 2013]. On average, traversing four transects took about 30 minutes (1800 s). To calculate discharge, the measured velocities were projected onto the average flow direction for each transect and the depth profiles to the banks were linearly extrapolated. To relate the velocity measurements with the tidal cycle, water levels were collected from the NOAA Lawma-Amerada Pass tide gauge [*NOAA*, 2016]. Average discharge from 06/16 to 06/19 at the Calumet gauge was 3344 m^3 s^{-1} [*USGS*, 2016] and the discharge entering the WLD downstream of the initial bifurcation was 2880 m^3 s^{-1} during falling tide on 06/20.

Site selection for the discharge measurements was based on spatial and

temporal feasibility. As changes in water level due to tides, river discharge, and wind may greatly alter the hydrodynamics at WLD, measurement of transects under similar conditions throughout the entire channel network is not feasible. In addition, the presence of distributary channel confluences adds considerable complexity to the measurement of discharge along the length of a primary channel. Therefore, we selected Gadwall and Main Passes due to their manageable spatial extent and because of the lack of confluences downstream of the initial bifurcation (location D in Figure 3.1c).

3.3.3 Mike Island tracer experiment

A dye tracer study was performed on Mike Island from 02/07/2014 through 02/11/2014. Nine measurement stations were deployed in the arrangement shown in Figure 3.1d, which extended 3200 m longitudinally along the axis of Mike Island and spanned 200 m laterally. Sites 1, 2 and 4 were placed in intervals of 100 m longitudinally and Sites 3 and 5 were laterally spaced 100 m from Site 4. Site 6 was 175 m south of Site 4 and Sites 7–9 were spaced at 800–1000 m intervals, depending on site conditions, along the longitudinal axis of the island. Each measurement site was equipped with a YSI 600 OMS optical rhodamine sensor (accuracy: greater of ±5% reading and 1 μg L^{-1}) measuring at 45-second intervals and Sites 1, 3, 5, 7, 8, and 9 were equipped with Solinst Levelogger Junior Edges (accuracy: ±10 mm) collecting a reading every 60 seconds. In addition, we collected wind velocity measured at six-minute intervals from the NOAA Lawma-Amerada Pass station (measured at a height of 10 m) [*NOAA*, 2016]. The average discharge at the Calumet station was 2130 m^3 s^{-1} for the duration of the experiment.

On 02/07 at 15:14 CST, 1700 mL of rhodamine dye tracer was released 60

m south of Site 1 and 40 m north of Site 2. The dye was stirred at the injection point to promote vertical mixing throughout the water column. Dye propagation was observed by measurement stations until 9:40 on 02/11.

Mike Island was selected as the study location for the tracer experiment based on its potential as a hot spot for denitrification. Relatively long residence times on the relatively large and long island may promote the cycling of nitrogen [*Nixon et al.*, 1996]. A time series analysis of satellite imagery at WLD reveals that Mike Island is relatively old, which has been linked to higher organic matter content and rates of denitrification [*Henry and Twilley*, 2014].

3.4 Results

3.4.1 Hydrological connectivity via secondary channels

Flow direction in relatively small secondary channels at WLD was modulated by tides. Discharge at S1 was 0.65 m^3 s^{-1} during falling tide on 07/22/2012. The flow direction pointed out of the island (northwest), but reversed during rising tide yielding a discharge of 0.63 m^3 s^{-1} with a flow direction pointing into the island interior (southeast). The magnitudes of the discharge were essentially unchanged. At S3, the discharge was 9.90 m^3 s^{-1} during falling tide. The flow direction pointed into the island interior (west) for S3 regardless of tidal regime, supporting the notion of discharge being carried from the channels to the islands via secondary channels. With a width of about 45 m, S3 represents a relatively large secondary channel at WLD, roughly four times wider than S1.

3.4.2 Hydrological connectivity via primary channel leakages

The results of the discharge measurements in Gadwall and Main Passes are summarized in Table 3.1. Discharges at the bifurcation creating Gadwall and Main Passes showed good agreement between the feeder channel (transect D) and the downstream branches (transects G and L). On 06/18 during falling tide, measurements at D yielded discharges of 970 and 1126 m^3 s^{-1} separated by 1.7 h. Temporally bounded by the measurements at D, transects G and L had discharges of 277 and 779 m^3 s^{-1}, which computes to a 94–109% agreement between upstream and downstream. Similar behavior was captured on 06/19 during rising tide when the discharges had a 97% agreement between D and the sum of G and L.

Figure 3.4 shows the downstream velocity structure for the five locations along Gadwall Pass on 06/18/2014. The figure spans a time period between falling tide until just after low tide. For each transect the velocity core follows the thalweg of the channel and is near the surface. Maximum velocities tend to decrease moving downstream, but there are also changes due to the transition from falling to rising tide. Channel area and maximum depth decrease in the downstream direction, along with the discharge. A similar structure was observed for all of the measured transects (not shown).

Discharge measurements in Gadwall Pass on 06/16 are shown in Figure 3.5a,b together with the water level at the time of each measurement. During falling tide, the average discharge at transect L-fall was 775 m^3 s^{-1}. An increase in discharge was observed when moving downstream to transect M, which had an average discharge of 836 m^3 s^{-1}. This increase was likely due to increased velocities in Gadwall Pass associated with the falling of the tide. After the measurement at transect

Table 3.1: Summary of discharge measurements from June 2014. Quantities are averaged among the quadruplicate transects at each location. The average computed over fewer than four transects is given in italics and values in parenthesis are the standard deviations of the measurements.

Time and Date	Location	Tide	Q (m^3 s^{-1})	A (m^2)	W (m)
10:30 16 Jun	L	Fall	774 (24)	1440 (69)	394 (17)
11:10 16 Jun	M	Fall	836 (11)	1348 (37)	433 (12)
12:16 16 Jun	N	Fall	725 (12)	1184 (17)	410 (9)
14:13 16 Jun	O	Rise	533 (16)	1166 (40)	403 (12)
15:14 16 Jun	P	Rise	359 (10)	1044 (90)	397 (18)
09:30 17 Jun	G	Rise	*208* (4)	*760* (13)	*359* (3)
12:12 17 Jun	G	Fall	272 (8)	746 (11)	368 (8)
12:50 17 Jun	H	Fall	268 (10)	601 (11)	222 (4)
14:03 17 Jun	I	Slack	256 (5)	602 (19)	228 (17)
14:45 17 Jun	J	Fall	254 (11)	588 (5)	269 (9)
15:42 17 Jun	K	Fall	195 (1)	614 (15)	400 (10)
16:55 17 Jun	G	Fall	279 (7)	715 (24)	376 (12)
10:22 18 Jun	D	Fall	970 (13)	2307 (30)	706 (8)
11:20 18 Jun	L	Fall	*779* (11)	*1468* (31)	*431* (7)
11:39 18 Jun	G	Fall	*277* (2)	*734* (14)	*369* (4)
12:03 18 Jun	D	Fall	*1126* (27)	*2259* (15)	*696* (5)
13:42 18 Jun	M	Slack	780 (15)	1379 (20)	462 (4)
14:45 18 Jun	N	Fall	751 (11)	1223 (21)	445 (9)
16:40 18 Jun	O	Slack	630 (16)	1157 (11)	412 (10)
17:17 18 Jun	P	Rise	*486* (9)	*1064* (48)	*397* (37)
17:42 18 Jun	L	Rise	*746* (4)	*1445* (32)	*427* (5)
08:27 19 Jun	D	Rise	*972* (12)	*2341* (28)	*714* (1)
09:07 19 Jun	G	Rise	251 (7)	747 (14)	375 (4)
09:52 19 Jun	L	Rise	698 (13)	1488 (31)	429 (19)
11:10 19 Jun	H	Slack	244 (3)	626 (13)	228 (11)
11:50 19 Jun	I	Fall	253 (4)	607 (12)	233 (8)
13:08 19 Jun	J	Fall	290 (6)	604 (24)	298 (11)
13:43 19 Jun	K	Fall	242 (6)	612 (21)	413 (8)
14:24 19 Jun	G	Fall	313 (7)	733 (21)	389 (9)

M, a steady decline in average discharge in Gadwall Pass was observed. Transect N had an average of 725 m^3 s^{-1}, transect O had an average of 533 m^3 s^{-1}, and transect P was measured at an average of 359 m^3 s^{-1}. During rising tide, the flow

at L was measured, but rough water surface conditions including waves caused inaccurate measurements. Increasing winds from the southeast (average above 3 m s^{-1} [*NOAA*, 2016]) were observed during the rising tide measurements at L. The discharge exiting Gadwall Pass at transect P was 46% of that measured at L-fall. This percentage, however, does not account for the changes in discharge induced by the tide, which were measured on the second series of Gadwall Pass measurements.

On 06/18, repeat measurements were made in Gadwall Pass (Figure 3.5c,d). Little deviation in the discharge measurements at L was induced by the change in tidal regime: falling tide average discharge at L (L-fall) was 779 m^3 s^{-1}, compared to an average of 746 m^3 s^{-1} during rising tide (L-rise). Discharges downstream of L followed a similar pattern as that observed on 06/16. Transect P was measured at an average of 485 m^3 s^{-1}. When considering the change between the two discharges (falling and rising) measured at L and the average at P, 62–65% of the discharge entering at L flowed through P.

Velocity transects in Main Pass were traversed on 06/17 and 06/19/2014. Measurements on 06/17 were performed predominantly during the falling limb of the tidal cycle (Figure 3.6a,b). The falling and low tide discharges (marked G-fall and G-low in Figure 3.6, respectively) were 272 m^3 s^{-1} and 279 m^3 s^{-1}, respectively. The discharge did not significantly change throughout the falling limb of the tidal cycle at this location. However, during rising tide (G-rise), the average discharge was 208 m^3 s^{-1}, which shows that tides do affect the primary channel discharges. After the G-fall measurement, discharge decreased with downstream distance, ending with an average discharge of 195 m^3 s^{-1} at transect K (Figure 3.6a,c). For the falling limb of the tidal cycle, the discharge exiting Main Pass at K was 70–72%

of that entering at G (G-fall and G-low).

Figures 3.6c,d display the results from the velocity transects in Main Pass on 06/19/2014. At G, the rising (G-rise) and falling tide (G-fall) average discharges were 251 and 313 $m^3\ s^{-1}$, respectively. Discharges did not steadily decrease moving downstream as measured on 06/17. This was likely due to the transects G-rise, H, and I being taken during rising tide and J, K, and G-fall being measured during falling tide. Transects H and I had discharges of 244 and 253 $m^3\ s^{-1}$, respectively, and discharge increased to 290 $m^3\ s^{-1}$ at J, then dropped at K to 242 $m^3\ s^{-1}$. This trend is in line with the measured water levels. Discharges were relatively low during rising tide at H and I, then increased at J in tandem with a decrease in water level due to falling tide. When comparing the falling tide discharges at G-fall and K, 77% was retained, which is in agreement with the observations on 06/17.

These results suggest that for Gadwall and Main Passes, 46–77% of the discharge entering the channel exited the mouth of the channel into the bay, indicating that a significant volume of water was delivered to the interdistributary islands (23–54%). Secondary channels and subaqueous levees likely served as conduits for flow from the channels to the inundated interdistributary islands. The reduction in flow within Gadwall and Main Passes coincided with a decrease in bank vegetation cover and a transition from subaerial to subaqueous levees (Figure 3.3). This channel-island surface water exchange highlights the hydrological importance of the WLD islands.

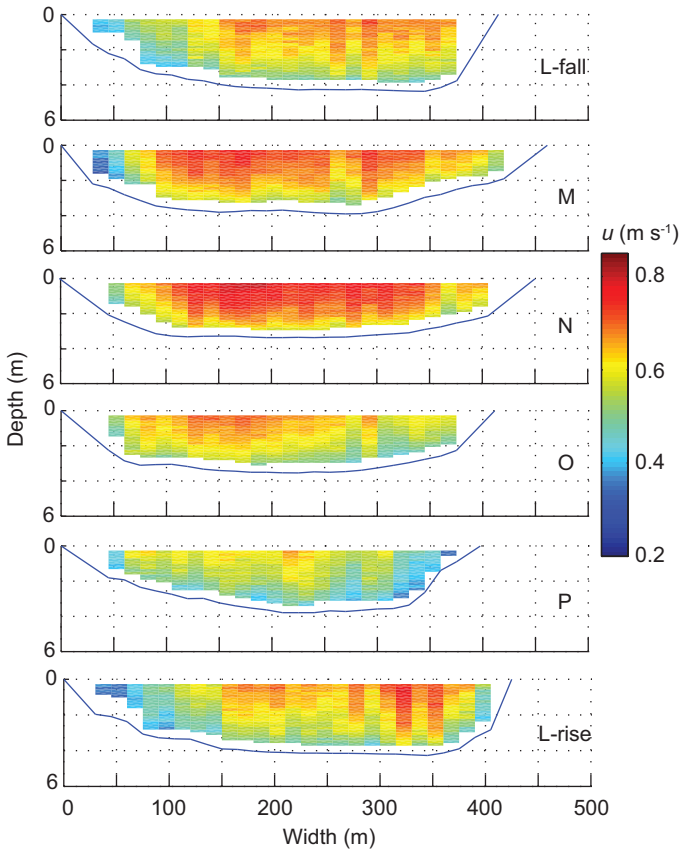

Figure 3.4: Spatio-temporal sequence of projected downstream velocity, u (m s^{-1}), in Gadwall Pass on 06/18/2014. The location of each transect is labeled. The bed (solid line) is linearly extrapolated to the banks. The vertical resolution of the velocity profile is 0.15 m. For visualization, the projected downstream velocity and depth profiles are horizontally binned at 15 m and averaged over repeat transects.

3.4.3 Hydraulic behavior of an inundated island

After its release, the dye rapidly propagated upstream to Site 1, peaking above the detection limit of 200 μg L^{-1} (Figure 3.7a). Once the water levels began to fall on 02/07 (Figure 3.7b) due to falling tide, the dye was again detected at Site 1 and subsequently Sites 2 and 4, which were located on the longitudinal axis of Mike Island directly downstream of Site 1 (Figure 3.1d). The plume of dye

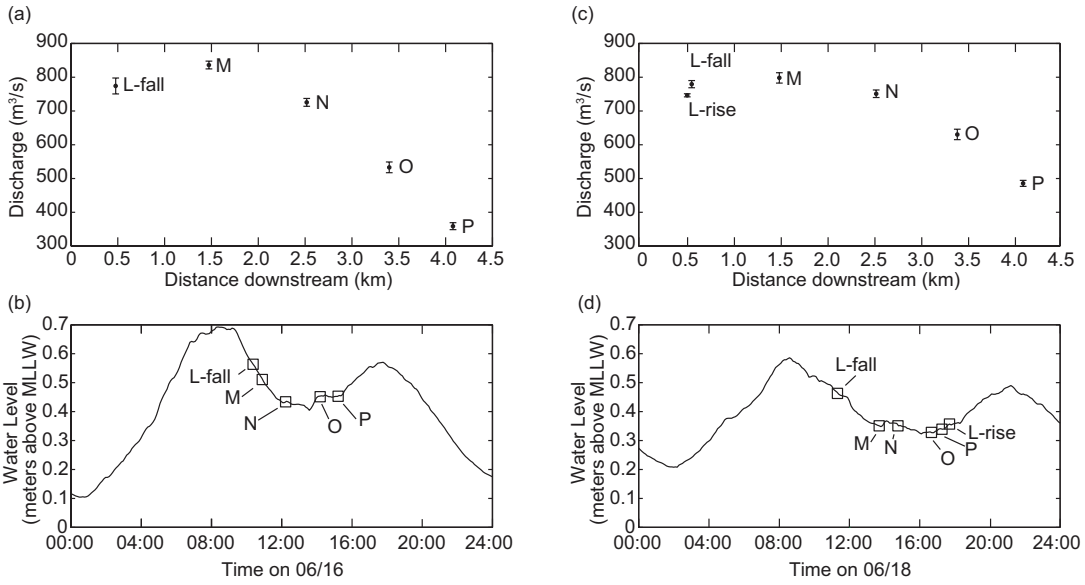

Figure 3.5: Discharge summary for Gadwall Pass. The top panels show the average discharge at each transect with the standard deviation of the measurements. The lower panels show the measured water levels at the Lawma-Amerada Pass station (NOAA #8764227).

passed through Site 4 just after the higher-low tide, about 5 hours after the dye was released. At the lower-high tide occurring at 22:20 CST (all subsequent times listed are CST), the dye moved back upstream and Site 4 saw an increase in rhodamine, peaking at 7.4 μg L^{-1}. About 0.3 hours later, Site 2 detected rhodamine with a maximum concentration of 14.7 μg L^{-1}. The dye moved north at least 150 m during this rising limb despite the predominantly ENE winds leading up to lower-high tide (Figure 3.7c). Dye was also detected at Site 6 at a peak concentration of 5.6 μg L^{-1} at lower high tide. The subsequent falling tide stretching into 02/08 induced a rapid downstream propagation of the plume to Sites 7, 8, and 9, resulting in an average falling tide velocity from Site 1 to 9 of 0.11 m s^{-1}. For the period of time described above, winds were less than 5 m s^{-1} from the east to east-northeast

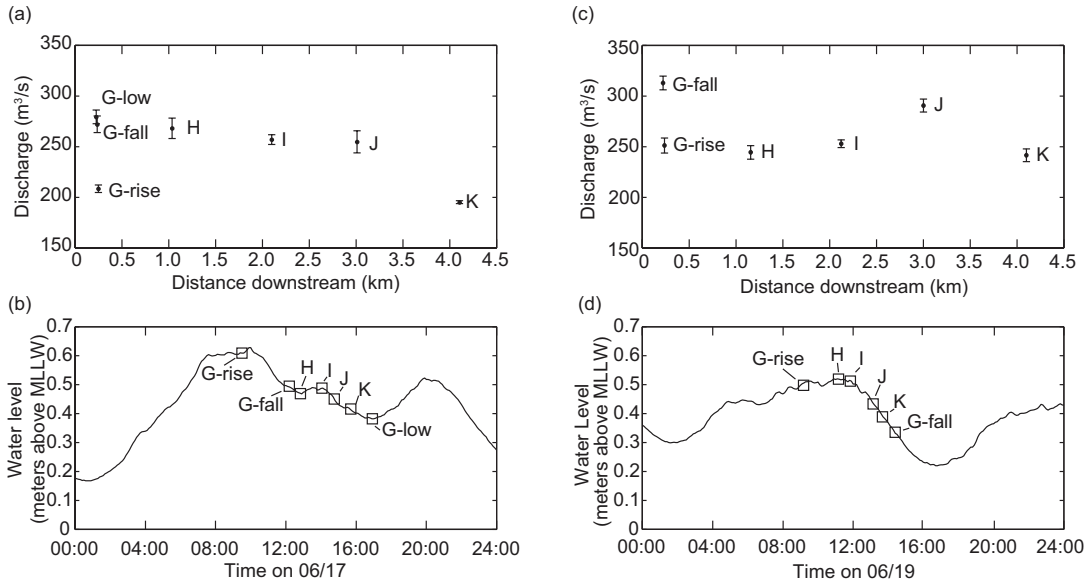

Figure 3.6: Discharge summary for Main Pass. The top panels show the average discharge at each transect with the standard deviation of the measurements. The lower panels show the measured water levels at the NOAA Lawma-Amerada Pass station (NOAA #8764227).

(Figure 3.7c).

After the low tide on 02/08, rhodamine was detected in small concentrations at Sites 1 - 6 and 9 at various times until high tide was reached. During this time period, wind rapidly changed direction but remained at relatively mild speeds under 5 m s^{-1}. A small peak of dye at Site 6 appeared at 18:27 on 02/08 lasting about 0.5 h with a peak of 5.1 μg L^{-1}.

The next flurry of dye spikes occurred in the first half of the day on 02/09. At 1:32, a concentration averaging 3.0 μg L^{-1} passed through Site 9 in five minutes (300 s). Small concentrations were expected because of dilution and the limited spatial resolution of the sensors. About 1.5 h later at 3:04, an average of 4.5 μg L^{-1} passed through Site 8. The next detection was upstream at Site 7 at 3:53,

with an average concentration of 4.5 μg L^{-1} passing through in 13 minutes (780 s). Time of detection from this point in time until high tide on 02/09 were as follows: Site 3 at 4:49, Site 4 at 5:49, Site 6 at 6:07, Site 5 at 7:39, and at Sites 1, 2, 4, 5, 6, and 9 between 8:47 and 10:31. All locations detected rhodamine before high tide on 02/09. Winds were low during this time period, mostly less than 2.5 m s^{-1}, blowing from between ENE and ESE. No dye was detected until a similar trend in concentration readings was observed on 02/10 (Figure 3.7a).

On 02/11, high concentrations of dye were observed in the upstream portion of the island, although there were readings at all of the sensors. Increasing winds speeds from the NE were observed before and during the morning on 02/11. As water levels fell, Site 9 detected rhodamine for 1.3 h starting at 3:05 with a peak concentration of 15.4 μg L^{-1}. Starting at 5:23, concentrations above the detection limit were measured at Sites 2 and 3 and lasted until 8:23. From 7:03 to 9:18 a steady concentration of 3.9 μg L^{-1} on average was measured at Site 4. Discrete peaks in concentration were detected at all other sites. Dye remained in the island for the duration of the experiment which lasted 3.8 days.

The Mike transect velocity measurements taken in July 2012 show a reduction in average velocity from 0.14 m s^{-1} during falling tide to 0.09 m s^{-1} at rising tide. A similar reduction in velocity was observed between falling and rising tides at transects L, G, and D during the June 2014 measurements. The associated rising tide and falling tide discharges for the Mike transect were 24.7 m^3 s^{-1} and 46.2 m^3 s^{-1}, respectively. The flow exited the island to the south, toward the bay, and the direction was unaltered by the turning of the tide. Although the measured velocities were relatively low compared to those of the distributary channels, the agreement was good between the repeat measurements at the Mike

transect. These results support the observed flow modulation due to tidal effects in the tracer experiment.

3.4.4 Travel times through the WLD network

Average velocities in the channels tend to decrease moving toward the bay (Figure 3.4). For example, averaging over the measured transects at L-fall results in a velocity of 0.53 m s^{-1} while the average at P is 0.40 m s^{-1}. Velocities are more consistent along Gadwall Pass, but do range from 0.46 to 0.36 m s^{-1}.

To calculate the travel times of water parcels through the channel-island complexes at WLD, we consider a simple network-based approach that includes both the distributary channel and an adjacent island (Figure 3.8). The lengths of the channels and the island longitudinal axis are derived from the 06/19/2014 LANDSAT 8 image and the delta front bathymetry of *Shaw and Mohrig* [2014]. Channel nodes represent velocity transect measurement locations. Channel centerlines are delineated and extended to their subaqueous mouths to form the channel links while island links followed the longitudinal axis of the island. The derived geometries are assigned to each channel link along with an average falling tide velocity based on measured values at its respective upstream transect. The island is discretized similarly, with nodes being placed at the same downstream distance from transect D (Figure 3.1c) as their channel counterparts. Allocation of water to the islands is assumed to be symmetric, so only one island is represented in the graph (Figure 3.8). The island links are assigned the falling tide tracer discharge of 0.11 m s^{-1}. Therefore, this simplified model does not account for the complexity in island flows observed in the tracer study nor tidal effects and serves as a conservative estimate of travel times of water parcels through a channel-island complex at

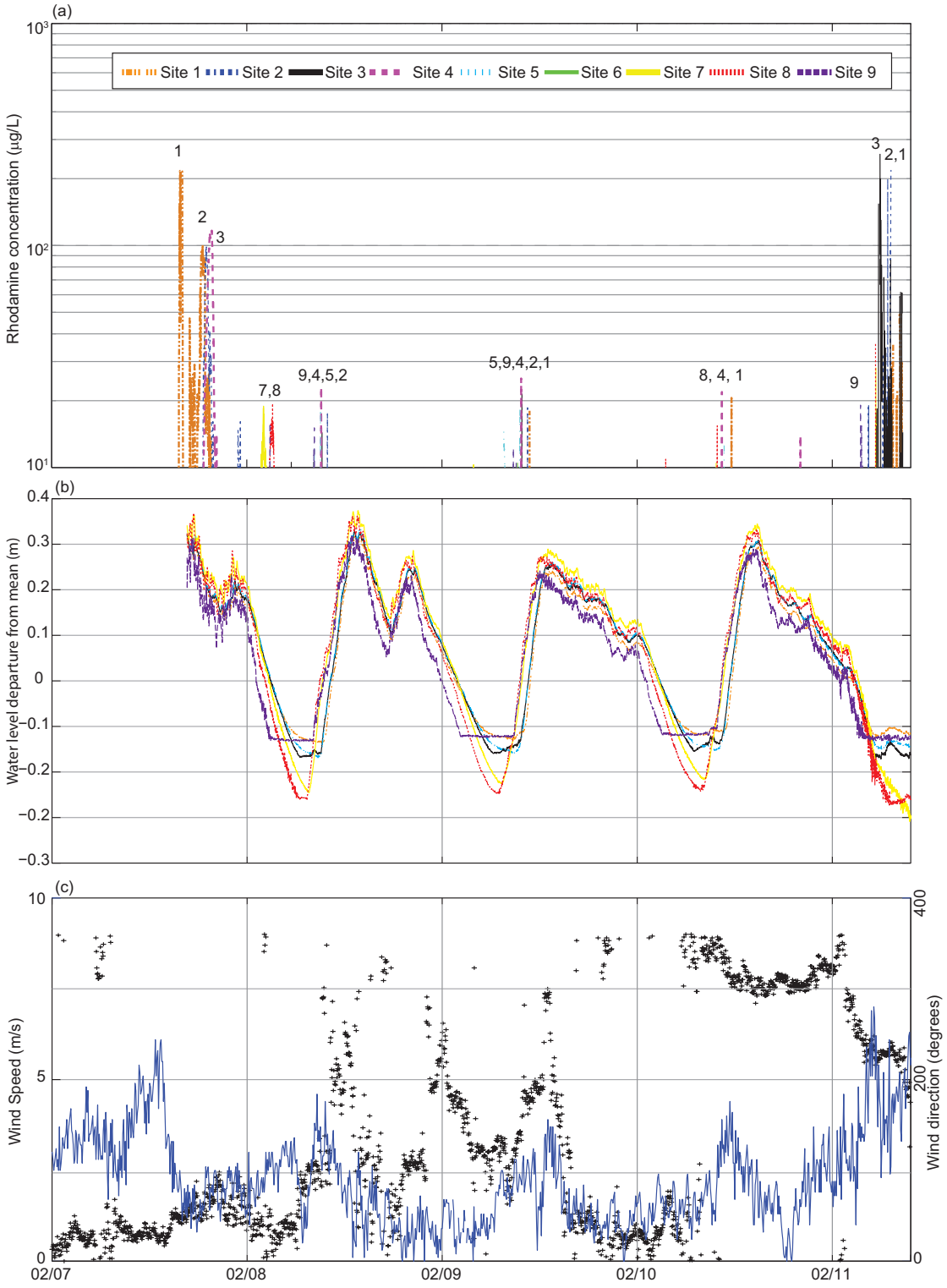

Figure 3.7: Summary of the tracer study performed on Mike Island in February

Figure 3.7 (cont.): 2014. (a) The dye concentration at each measurement location for the duration of the tracer experiment on Mike Island. Initial upstream propagation was observed after the high tide release of dye, followed by downstream movement during falling tide from late evening on 02/07 to early morning on 02/08. On 02/11, a spike in concentration is observed at nearly all stations, pointing to the probable control of wind and trapping of dye by vegetation (see text for further discussion). (b) The deviation from mean water depth at Sites 1, 3, 5, 7, 8, and 9 (same color scheme as in (a)). Flat areas in the troughs of the curves indicate that the water level dropped lower than the pressure transducer on the water level logger. (c) Time series of wind speed and direction measured in six-minute averages at the NOAA weather station at Lawma-Amerada Pass [*NOAA*, 2016]. The crosses indicate direction and the line represents the wind speed.

WLD under the measured conditions. Both Gadwall and Main Passes are considered. A water parcel is allowed to enter the island downstream of transects G and L, where the allocation to the island was observed in the discharge measurements. Lateral travel times between the channel and the island were ignored.

The estimated travel times through the channel-island complex are significantly increased with water entry onto the island (Table 3.2). The minimum travel time of a water parcel from transect D to the bay is 4.4 hours and the maximum travel time is 14.3 hours, which is over three times the minimum. Water parcel travel times are increased by entry into the island for both Gadwall and Main Pass channel-island complexes (Table 3.2). The 14.3-hour travel time does not include flow direction changes within the island, though water remaining on the island for this amount of time would likely be subject to tidal effects.

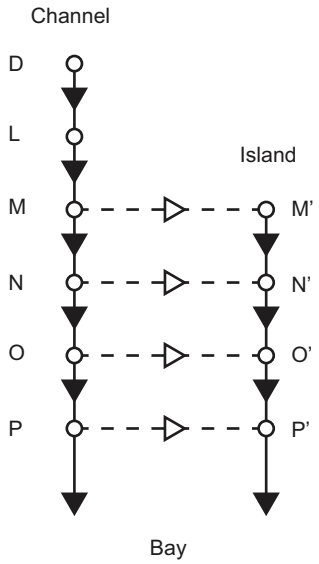

Figure 3.8: Travel time calculation through a channel-island complex at WLD represented here by the locations (nodes) at which measurements were taken along the channels (Figure 3.1c) and their island counterparts (located at the same radial distance from transect D as the channel nodes). Average velocities from the channel velocity transects and the average falling tide tracer velocity were used in the travel time calculation for the channel and island segments, respectively. In this case, the channel-island complex along Gadwall Pass is depicted.

Table 3.2: Summary of the simplified travel time calculation for the channel-island complexes along Gadwall and Main Passes (Figure 3.8). Locations in parenthesis represent paths within the island.

Path	Travel Time (hr)
DLMNOP	4.4
DLMNO(P')	8.7
DLMN(O'P')	10.0
DLM(N'O'P')	11.7
DL(M'N'O'P')	13.8
DGHIJK	5.9
DGHIJ(K')	8.6
DGHI(J'K')	10.9
DGH(I'J'K')	12.6
DG(H'I'J'K')	14.3

3.5 Discussion

3.5.1 Hydrological connectivity in river deltas

To summarize our hydrological connectivity analysis at WLD, a schematic depicting the flow pathways within the channel-island complex based on structural and process-based connectivity is presented in Figure 3.9. In the upper portion of the channel-island complex, there is limited exchange between the channel and the island interior. Secondary channels maintain the hydrological connection between the primary channel and the island interior (structural), but tidal processes control the direction of the flux (process-based). Small secondary channels (such as S1) are examples of the dynamic nature of process-based connectivity at WLD, as tides modulate flow direction. Larger secondary channels (such as S3) tend to be unidirectional because the water flux momentum tends to be greater than the momentum of tidally- or wind-driven fluxes. Further downstream, the transition from subaerial to subaqueous levees promotes overbank flow from the distributary

channel to the island. Gadwall and Main Passes at WLD allocated 23–54% of their water fluxes to the interdistributary islands. This suggests that substantial volumes of water at WLD are transported from the distributary channels to interdistributary islands. Surface water is carried to the island interiors from the primary channels via secondary channels and overbank flow over subaqueous levees (Figure 3.9). Delta islands, the recipients of this flow, are thus important portions of the hydrological network of WLD, and should, therefore, be included as part of the deltaic network for the routing of water, sediment, and nutrients. It should be noted that this overbank flow is not necessarily associated with flood discharges as in tributary systems, but was observed during relatively average riverine discharge conditions. Since water levels near the shoreline in backwater zones are relatively insensitive to discharge changes [*Chatanantavet et al.*, 2012], channel-island flow exchange is expected to persist over the range of discharges entering WLD. This mechanism of channel-island exchange is thus distinct with respect to flood-induced overbank flow in tributary systems. We note also that while the channel network is 'distributary,' and thus fluxes diverge from the apex to the bay, island fluxes converge towards the island center suggesting a 'tributary' character of the island portion of the network. The channel-island network shows a mixed divergent-convergent network behavior and should be investigated in future studies on environmental transport.

Elevation is the main control on vegetation type at WLD [*Carle et al.*, 2013], which has an effect on the hydrological connectivity between channels and islands. Near the island apices, relatively high elevation and well-established levees are populated by *Salix nigra* that stabilize the bank [*Shaw et al.*, 2013]. Hydrological connection between the primary channels and island interiors near the island

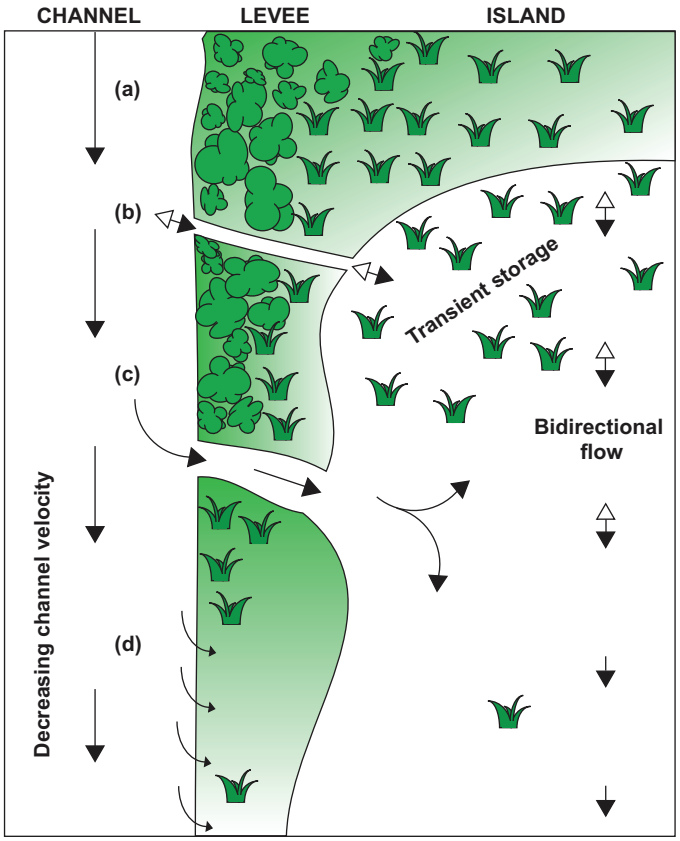

Figure 3.9: Schematic diagram of surface water pathways for a generic and idealized channel-island complex at WLD. Flow directions are representative of the dominant flows. (a) Zone of negligible surface water connectivity between the channel and island during average flow conditions. In this region channel velocities are relatively high, the levees are heavily vegetated and subaerial, and the island interior is characterized by vegetated subaerial marshland. (b) An example of a bidirectional secondary channel which can bring flow into or out of the island interior, based on differential water level setups due to tides, wind, or riverine input. Flows in the island interior are also bidirectional, depending on the above conditions. Vegetation influences flow within the island portion of this zone (see text). (c) An example of a large unidirectional secondary channel that continually brings flow into the island. Tidal/wind induced velocities are unlikely to counteract the momentum from the channel input. (d) Zone of significant flow partitioning from the channel to the island interior. The levee zone is characterized by a transition from subaerial to subaqueous and by a decrease in vegetation. Channel velocities tend to decrease due to spreading and flow within the island interior tends to be unidirectional.

apices is limited because the elevation of the banks discourages over-topping. The decrease in vegetation in the distal portion of the delta may influence the presence of secondary channels and subaqueous levees, both of which are forms of channel-island structural connectivity. The probability of significant fluxes across hydrological connections is higher in the areas with limited vegetation compared to those areas where vegetation is dense.

The direction of flow within the island is controlled by the tide, the magnitude of flux from the primary channel, and wind. Surface water within the island is slow moving and is populated by emergent vegetation. In areas receiving little flux from the primary channels, wind and tides exert significant effects on the flow dynamics because the ambient water has little momentum input from the channel. For example, upstream propagation of the dye was observed during the rising limb of the tidal cycle directly after injection and dye returned upstream during the next rising limb (Figure 3.7), which points to the control of tides. Increased winds likely have caused the large spikes in dye concentration on 02/11 (Figure 3.7). The northeast winds may have released dye in transient storage within vegetation patches (Figure 3.10) in the northern portion of the island near Sites 1, 2, 3, and 4, leading to high concentrations of dye being sporadically released from transient storage. The upstream portion of the island responds to the tidal cycle and wind events. Tidal momentum, however, may not be able to reverse flow directions near large secondary channels or in the presence of overbank flow. Upstream tidal amplification and spatial differences in island water depths may also play a role in determining where flow inversion due to tides occurs. These observations support the introduction of hydrological connectivity into the study of river deltas. Complex behavior driven by several external drivers, as well as the internal complexity

of the system, necessitate system-scale observations that can be analyzed within the context of hydrological connectivity.

Tidal action affects discharge within the distributary channels by lowering velocities during rising tide and increasing them during the falling limb. Rising tide discharges were 74–96% of their falling tide counterparts and no effect on flow direction was detected in our observations. The discharge at transect Mike during rising tide was 53% of the falling tide discharge and the bayward flow direction was unchanged. Secondary channels may instead exhibit flow inversion, depending on topographic and environmental conditions. Channel S1, characterized by a small discharge, exhibited a flow inversion. Channel S3 carried a larger discharge and consistently flowed into the islands regardless of tidal regime. The secondary channel flows were measured during a period of very low flow (1021 m^3 s^{-1} measured upstream at Calumet) and the relatively small river forcing may have enhanced the effect of the tides.

Because of the large spatial domain of Mike Island and the limited spatial resolution of the sensors, dye likely entered unmeasured portions of the island or followed pathways circumventing the sensor locations. Velocities on the island are small and thus the dye tracer was likely weakly mixed in the transverse direction. The significance of the tracer study does not hinge on lateral mixing, as the convergent nature of the island fluxes likely contained the bulk of the tracer to the island longitudinal axis, where our sensors were located, which allowed the behavior of the dye to be measured.

This study does not address the groundwater component of hydrological connectivity. Hyporheic flow across the levee likely comprises a portion of the discharge reduction observed in the distributary channels. This study also ignores

the effects of the spring and neap tide and significant changes in riverine input. These factors should be addressed in future studies.

3.5.2 Implications to delta morphology

The presence of significant hydrological connections between the primary channels and interdistributary islands at WLD has important implications for delta evolution both morphologically and ecologically. As water flows into the islands at WLD, it carries sediment and nutrients. We argue that this hydrological connection is of first-order importance to delta eco-geomorphic evolution.

The allocation of flow to WLD islands suggests that hydrological connectivity between channels and islands (or floodplains) influences delta morphology, as the delivery of sediment via water flow is crucial for developing and maintaining delta form [*Edmonds et al.*, 2011a]. Since the primary channels at WLD can be erosional [*Edmonds et al.*, 2011b; *Shaw et al.*, 2013; *Shaw and Mohrig*, 2014], deposition within the islands is important for the maintenance of the delta platform. During large floods, which likely increase channel-island connectivity, sand is transported in suspension [*Shaw et al.*, 2013] and can deposit on the subaqueous island interiors [*Shaw and Mohrig*, 2014]. During below-average flows, sand is deposited on the levees, while channels extend and bifurcations remain stable [*Shaw and Mohrig*, 2014]. The significant water flux to islands facilitates sediment transport to island levees and interiors. Thus, increased connectivity to deltaic floodplains may provide a possible avenue for mitigating wetland loss. Various investigators have proposed increasing channel-floodplain connectivity through engineered river diversions [*Day Jr. et al.*, 2000; *Kim et al.*, 2009; *Allison and Meselhe*, 2010; *Paola et al.*, 2011]. Of such implemented diversions, the West Bay diversion in

Louisiana has been shown to retain 30–70% of the sediment supplied, leading to sub-aerial land formation [*Kolker et al.*, 2012]. A system-scale analysis of hydrological connectivity is a vital piece in understanding the evolution of natural deltas and engineered river diversions.

The water flux to the islands decelerates the channel flow due to spreading and friction, which decreases the momentum of the channel flow. This has important implications for the prediction of delta distributary network structure. The slowing of velocities due to flow expansion in a turbulent jet has been identified as the driving process in the development of river mouth bars [*Wright*, 1977; *Edmonds and Slingerland*, 2007; *Mariotti et al.*, 2013] and subaqueous levees [*Rowland et al.*, 2010]. At WLD, the expansion of flow is occurring over several kilometers as water is fluxed over subaqueous levees and, thus, may not rapidly expand like a turbulent plane jet in a standing body of water. The overbank flux may favor subaqueous levee formation over mouth bar formation [*Rowland et al.*, 2010], which would lead to the elongated channel pattern observed in the east-central portion of WLD [*Edmonds et al.*, 2011a] since sand can be deposited on levees during low-flow conditions [*Shaw and Mohrig*, 2014]. Since centerline velocity exhibits an effect on the distance to a river mouth bar [*Edmonds and Slingerland*, 2007], the effect of water flux to islands must be accounted for in models for predicting bifurcation length scales. Due to the complexity of the problem, modeling studies often treat distributary channel mouths as turbulent jets with no overbank flow upstream of the mouth [e.g., *Edmonds and Slingerland*, 2007], but future work should include this condition of upstream overbank flow.

3.5.3 Implications to delta ecology

At the landscape level, hydraulic travel times through aquatic systems are relatively unknown in coastal settings [*Rivera-Monroy et al.*, 2010], but are essential to the prediction of denitrification at large scales [*Yu et al.*, 2006; *Rivera-Monroy et al.*, 2010]. At WLD, we have quantified the travel times of water parcel through a channel-island complex by including the islands in the hydrological network, which significantly increases travel times. Currently, WLD contains few islands that tend to be relatively large [*Edmonds et al.*, 2011a]. As river deltas grow according to river mouth bar models, bifurcation distance decreases with increasing distance from the delta apex [*Edmonds and Slingerland*, 2007; *Jerolmack and Swenson*, 2007], creating a large number of smaller islands. As islands grow and more are formed, fluxes from the primary channels into the islands will increase travel times as more island area is available for transport of material. Island sizes in a mature delta have been shown to have a power-law distribution [*Passalacqua et al.*, 2013], which may lead to a heavy-tailed distribution of travel times.

High concentrations of nitrate are present in the Mississippi and Atchafalaya River waters [*Rivera-Monroy et al.*, 2010; *Lane et al.*, 2011] and ambient concentrations in WLD have been measured at >60 μM [*Henry and Twilley*, 2014]. Since a significant portion of the water at WLD enters the islands, nitrate transport to the islands is likely significant as well. The connectivity between channels and islands represents an important ecological link at WLD that may modulate nitrate cycling. In the Davis Pond river diversion near WLD, *Yu et al.* [2006] modeled 42$\pm$2.5% and 95$\pm$0.5% nitrate removal for travel times of one and five days, respectively. These results provide a context for understanding the ecological impact

Figure 3.10: Image looking downstream taken 30 minutes after the rhodamine dye release on 02/07/2014. The rhodamine dye plume is bright pink due to high concentrations near the release point.

of travel times at WLD. For the case of transport exclusively by primary channels from transect D to the bay, travel times are in the order of a few hours (Table 3.2), which indicates that denitrification in channels is likely limited by the travel time at WLD. However, the tracer study revealed that dye remained in the system after 3.8 days. Increased travel times associated with water parcels entering islands within the channel-island complex model (Table 3.2) and the tracer result suggest that significant denitrification may occur when nitrate is transported to the islands.

3.6 Conclusions

In this study, we have quantified the surface water component of hydrological connectivity between distributary channels and interdistributary islands at WLD over tidal time scales and related that exchange to delta evolution and environmental transport. We find that a significant portion of the WLD water flux passes through the interdistributary island interiors and that travel times within the islands are controlled by a suite of environmental forces, which subsequently influence system travel times. The conclusions we draw from the analyses of flow partitioning and island hydrologic pathways at WLD provide new insight into channel-island coupled processes in river deltas, linking for the first time distributary channels and interdistributary islands, previously analyzed as separate entities at different spatial and temporal scales. We find this coupling to be fundamental to delta eco-geomorphic evolution. The results of this work can be used to validate predictive models of environmental transport in natural river deltas and engineered river diversions.

Transects surveyed with a boat-mounted ADCP along two distributary

channels at WLD were used to quantify the volumetric water exchanged with interdistributary islands over tidal time scales during relatively average upstream discharge conditions. The ADCP was also used to measure flows within secondary channels connecting the primary channels to an island interior and the discharges exiting the bayward boundaries of two islands. A hydraulic dye tracer was deployed on an inundated island in the delta network to quantify the hydraulic residence time and to characterize the flow of the island interior subject to wind and tidal forces. A simplified model of a channel-island complex was used to calculate travel times. From analyses of these data, we make the following conclusions:

(1) Interdistributary islands have a significant hydrological connection with distributary channels and play an important role in the hydrological network at WLD. Discharge measurements within primary channels indicate that 46–77% of the water flux at the initial bifurcation is conveyed to the bay. The remaining discharge (23–54%) is allocated to the interdistributary islands, which indicates that islands deliver a volume of water to the bay that is on the same order of magnitude as the distributary channels. Secondary channels and overbank flow over subaqueous levees act as the avenues for the channel-island connectivity and vegetation likely plays a role in determining the spatial distribution of flow exchange. Channels consistently allocate water to the islands regardless of the tidal regime for the measured upstream flow conditions. Since the islands convey significant discharge to the receiving waters, network analyses of WLD and similar deltas must include the inundated interiors of islands and their connections to the major distributary channels in order to appropriately represent the hydrological behavior of the system. Ignoring islands as part of the delta network would result in a reduction of fluxes measured at the system outlet and anomalously short travel

times. For example, at WLD, ignoring islands would result in 23–54% less flux to the bay and at least three times shorter travel times through the system;

(2) Tides affect the process-based connectivity of surface water between the distributary channels and islands at WLD. Flow into and out of the islands is modulated by the tidal cycle. However, since flow exchange was observed regardless of the tidal regime, structural connectivity in the form of secondary channels and flow over subaqueous levees controls the flow exchange at WLD. Discharges exiting the bayward boundaries of an interdistributary island were reduced by the rising tide to 53% of the falling tide discharge. In a small secondary channel, the tide modulated the flow direction, but the flow direction in a large secondary channel was unaltered;

(3) Water flux into the island interiors increases the time for a water parcel to travel through the WLD network. Travel times calculated with a simplified model of water transport through a channel-island complex range from 4.4 to 14.3 hours, depending on flow path. A dye tracer experiment revealed dye was present in high concentrations 3.8 days after the release of the dye, which points to the complex hydraulic behavior of the island interiors and potential for increased travel times for water entering the interdistributary islands. The significant allocation of water to the islands and the increased travel times enhance the denitrification potential of deltaic systems such as WLD.

Chapter 4: Controls on hydrological connectivity, water residence time distributions, and nitrate removal in a river delta channel-island complex

4.1 Introduction

The physics of hydrological connectivity are important for understanding the ecological and morphological effects of water, sediment, and nutrient transport across a landscape [*Pringle*, 2003; *Tetzlaff et al.*, 2007; *Fryirs*, 2013]. In coastal river deltas, hydrological connectivity between the channels and deltaic islands is subject to a complex interplay among environmental processes including river discharge, tides, wind, and vegetation [*Hiatt and Passalacqua*, 2015; *Geleynse et al.*, 2015]. Recent field work at the Wax Lake Delta (WLD) in coastal Louisiana (Figure 4.1) has shown that 23–54% of the water flux entering WLD is allocated to the deltaic islands [*Hiatt and Passalacqua*, 2015], rendering deltaic islands key elements of the delta's hydrological network. Surface water residence times are highly influenced by the hydrological connectivity between the distributary channels and deltaic islands [*Hiatt and Passalacqua*, 2015].

Deltaic islands are zones of relatively high rates of nutrient removal [*Henry and Twilley*, 2014] and freshwater hydraulic residence time is a major control on nutrient removal in coastal wetland systems [*Nixon et al.*, 1996; *Dettmann*, 2001;

This chapter has been submitted as an article to Water Resources Research with Matthew Hiatt, Edward Castañeda-Moya, Robert Twilley, Ben R. Hodges, and Paola Passalacqua as authors.

Yu et al., 2006]. Deltaic islands at WLD are a home to shallow, vegetated wetlands [*Carle et al.*, 2013] that maintain a significant surface water connectivity with the distributary channels [*Hiatt and Passalacqua*, 2015; *Shaw et al.*, 2016]. Thus, understanding the hydrological connectivity between deltaic channels and islands is an important precursor to estimating the nutrient removal potential of both natural deltas and those formed downstream of engineered river diversions. In this article, we investigate the processes controlling hydrological connectivity and water residence time distributions (RTD) in a river delta channel-island complex using numerical modeling and make estimates of nitrate removal supported by field measurements.

A conceptual model of hydrological connectivity in a river delta channel-island complex was developed by *Hiatt and Passalacqua* [2015] based on their field observations at WLD (Figure 4.2a). In their conceptual model, (1) a significant fraction of the incoming flow departs the channel and enters the deltaic island leading to a decrease in flow velocity within the channel; (2) flow between distributary channels and deltaic islands is modulated by river discharge and tides; (3) flow within the island is subject to directional changes owing to tides and wind; and (4) a zone of transient storage is present in the vegetated portion of the island. At coastal tidal junctions, the flow allocation between channels is affected by bed roughness, river discharge, and tidal amplitude [*Buschman et al.*, 2010; *Sassi et al.*, 2011], and similar controls may exist for channel-island hydrological connectivity in river deltas. Within wetlands, vegetation slows the flow by increasing the hydraulic roughness [*Kadlec*, 1990; *Nepf*, 1999; *Nepf and Vivoni*, 2000; *Leonard and Croft*, 2006], which may alter both the flow allocation within the detaic island wetland and the hydrological connectivity with the distributary channel. Wetland

vegetation can also influence the water surface slope and water residence times [*Jadhav and Buchberger*, 1995]. With the model developed herein, we add new understanding of the effects of river discharge, tides, and hydraulic roughness due to vegetation on hydrological connectivity, RTD, and nitrate removal.

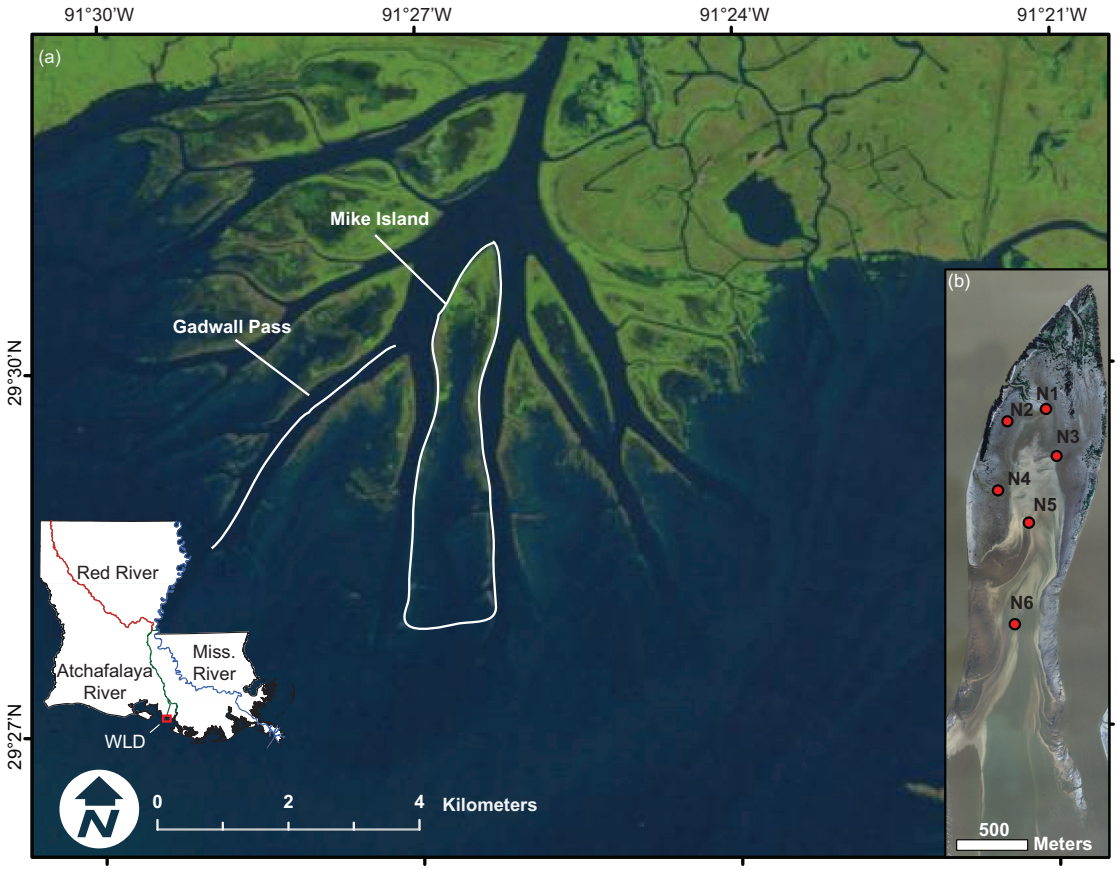

Figure 4.1: Map of field data collection sites. (a) Wax Lake Delta (WLD) in coastal Louisiana with Gadwall Pass and Mike Island delineated. Image specifications: LANDSAT image from 02 November 2011 at 30 m resolution obtained from the USGS Global Visualization Viewer (available online at http://glovis.usgs.gov/). (b) Locations of the nitrate sensors on Mike Island. The image is aerial photography from 6 November 2009 with 0.30 m resolution.

The transport of nutrients in coastal systems is currently a pressing environ-

mental issue. Coastal eutrophication is a growing worldwide problem [*Smith*, 2003] due to increasing dissolved reactive nitrogen and phosphorous concentrations being delivered to the coast, which can lead to excessive phytoplankton blooms that can cascade to hypoxia, as well as other environmental issues [*Rabalais et al.*, 2002a; *Boyer et al.*, 2006; *Diaz and Rosenberg*, 2008; *Heisler et al.*, 2008; *Turner et al.*, 2008]. Coastal wetlands, river deltas, and estuaries can mitigate increased nutrient pollution in receiving waters by using, transforming, or burying nutrients to reduce impacts on downstream ecosystems [*Dettmann*, 2001; *Lane et al.*, 2003, 2004; *DeLaune et al.*, 2005; *Yu et al.*, 2006; *Luu et al.*, 2012]. Wetlands serve as important nutrient sinks [*Yu et al.*, 2006; *Luu et al.*, 2012], and the removal capacity of these systems is known to be coupled to wetland hydrology [*Bowden*, 1987]. However, system-scale RTDs are unknown in most areas in coastal Louisiana, which makes the estimation of nutrient removal at large scales challenging [*Rivera-Monroy et al.*, 2010].

Engineered river diversions have been suggested as a restoration strategy to partially reduce coastal wetland loss and excess nutrient delivery to the coastal zone [e.g., *Kim et al.*, 2009; *Paola et al.*, 2011; *Mitsch et al.*, 2001]. River diversions are currently being implemented in coastal Louisiana as outlined in the Louisiana Coastal Master Plan [*Louisiana Coastal Protection and Restoration Authority*, 2012]. Diversions are thought to significantly alter nutrient allocation and RTD [*Rivera-Monroy et al.*, 2010] by increasing the volume of river water passing through coastal wetlands, which can significantly reduce nutrient export to downstream receiving waters [*Mitsch et al.*, 2001; *Lane et al.*, 2004; *Yu et al.*, 2006]. Thus, it follows that improved predictions of the ecological and water quality impacts of proposed river diversions should be facilitated by improved understanding

of the physical controls on coastal system RTD and nutrient export.

To quantify and improve our understanding of the environmental controls on hydrological connectivity in river deltas, we (1) measure surface water nitrate concentrations within the islands at Wax Lake Delta (WLD) in coastal Louisiana (Figure 4.1), (2) use numerical modeling to quantify the coupled channel-island hydraulics and the influence of hydraulic roughness, river discharge, and tidal amplitude on hydrological connectivity in an idealized channel-island complex, (3) calculate surface water residence time distributions, and (4) estimate nitrate removal. We chose to investigate nitrate in this study because it is the dominant form of excess nitrogen entering coastal regions [*Twilley and Rivera-Monroy*, 2009].

This paper is organized as follows. We first introduce the Wax Lake Delta field site and summarize the field observations of surface water nitrate that motivate our modeling study (Section 2). We then describe our two-dimensional hydrodynamics and scalar transport model (Section 3) followed by a summary of the modeling approach within an idealized channel-island complex (Section 4). Then we investigate the effects of river discharge, tides, and hydraulic roughness on channel-island hydrological connectivity, RTD, and nitrate removal (Section 5). A discussion of the results and implications for the restoration of coastal islands follows (Section 6) and finally we state our conclusions (Section 7).

4.2 Field Measurements

4.2.1 Site Description

The WLD (Figure 4.1) is a naturally prograding delta that has been considered an analog for successful land-building river diversion projects [*Kim et al.*, 2009; *Paola*

et al., 2011; *Allison and Meselhe*, 2010]. The WLD is located at the mouth of the Wax Lake Outlet (WLO), a 25-km long channel dredged in by the U.S. Army Corps of Engineers to reduce flooding risk in the Atchafalaya Basin [*Fisk*, 1952]. The WLO transported and deposited sediment at its mouth, causing WLD to develop emergent land starting in 1973 [*Roberts et al.*, 1997]. The average annual flow in the Wax Lake Outlet (U.S. Geological Survey Gage #07381590 in Calumet, Louisiana—18 km upstream of the WLD apex) is about 2700 m^3 s^{-1}, and floods annually exceed 5000 m^3 s^{-1} [*USGS*, 2016]. As is the case for the entire Gulf of Mexico [*Grace*, 1932], the WLD is microtidal. The typical diurnal tidal amplitude in the area is 0.24 meters [*NOAA*, 2016], but storm surges, other tidal components, the secular (seasonal) water surface variation affect the overall water surface level, leading to larger fluctuations in water level.

The WLD network consists of primary distributary channels, islands with interior islands, and secondary channels that connect distributary channels to islands. The primary distributary channels grow shallower in the seaward direction to about 30% of the initial channel depth and can extend 2–6 km beyond the sub-aerial portion of the delta [*Shaw and Mohrig*, 2014]. The islands are flanked by natural levees that transition from sub-aerial to sub-aqeuous extending downstream towards the Atchafalaya Bay. The islands are inundated and populated with common freshwater wetland vegetation species [*Carle et al.*, 2013].

Recent field work has shown that 23–54% of the water flux entering WLD is allocated to the deltaic islands via overbank and secondary-channel flow [*Hiatt and Passalacqua*, 2015]. This hydrological connectivity between the primary distributary channels and the islands is exemplified by secondary channels and overbank flow along the western margin of Mike Island (Figure 4.2a). Within the islands,

water travel times are relatively long compared to their channel counterparts because of decreased velocities, flow resistance due to vegetation, wind effects, and tidal contributions [*Hiatt and Passalacqua*, 2015]. Ambient surface water nitrate concentrations at WLD have been measured at >62 μM by *Henry and Twilley* [2014], who found that WLD's islands possess a significant capacity for removing nitrate. Therefore, the hydrological connectivity between the primary distributary channels and deltaic islands is important for estimating RTD and nitrate removal [*Hiatt and Passalacqua*, 2015].

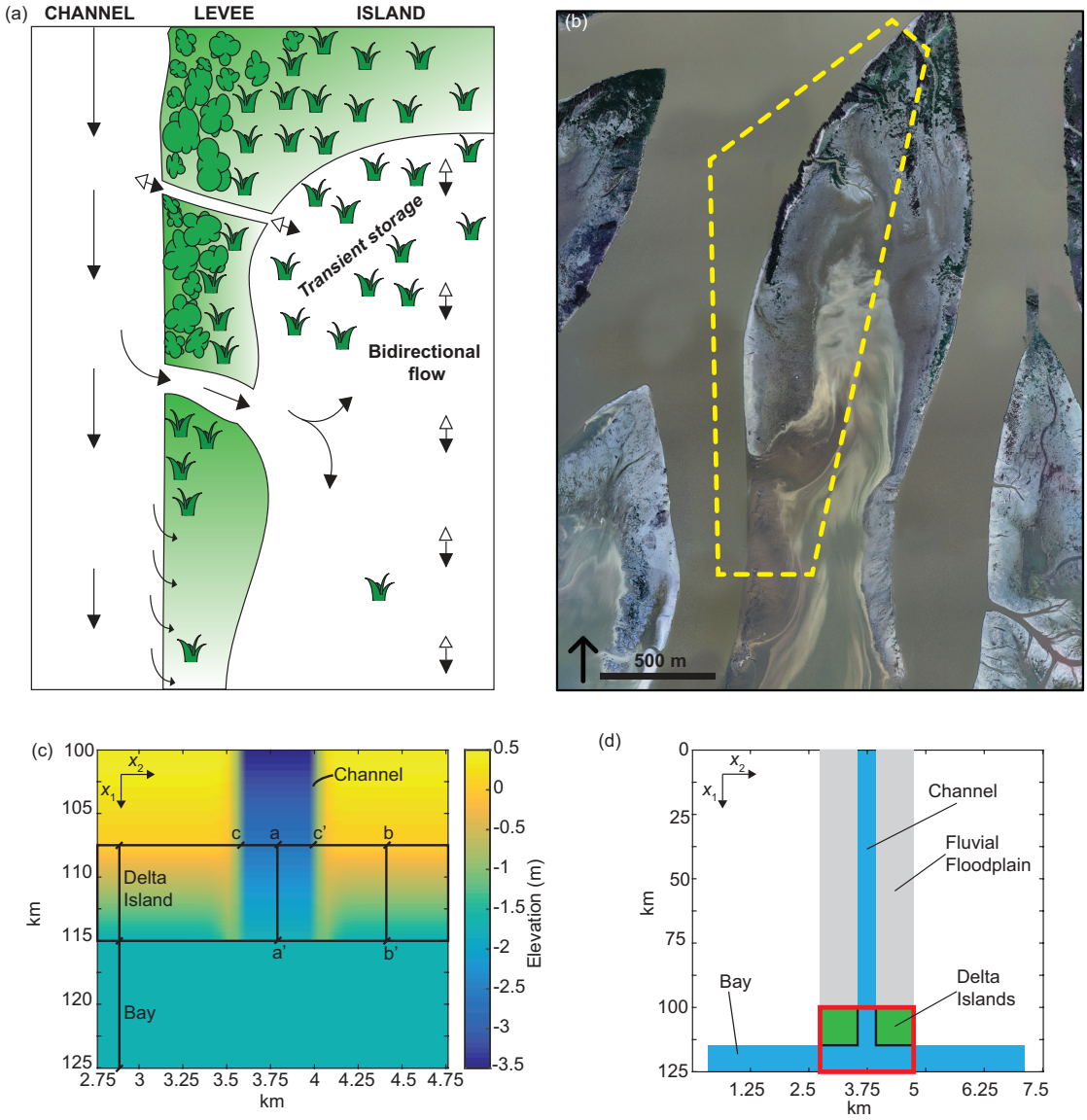

Figure 4.2: Examples of the idealized channel-island complex for a river delta and the computational domain. (a) Conceptual cartoon of an idealized channel-island complex. Adapted from *Hiatt and Passalacqua* [2015]. (b) Example of (a) from Mike Island at WLD. (c) The idealized delta channel-island complex test domain. A central channel with a linear adverse gradient is flanked by islands with levees and beds that are linearly decreasing in elevation to the bay. The bay is flat-bottomed. A numerical tracer is released within the channel along transect $c - c'$ and the tracer propagation is monitored at the boundary between the deltaic islands and the bay, where the RTD is calculated. (d) Cartoon of buffer domain including the 100-km upstream channel and extended bay at the seaward boundary. The upstream end of the buffer domain, the model is forced

Figure 4.2 (cont.): with a constant discharge. At the downstream end, the boundaries are open with water level prescribed. The channel-island complex test domain is outlined in red.

4.2.2 Nitrate data

To quantify the nitrate dynamics within the WLD islands, we measured surface water nitrate concentrations at Mike Island (Figure 4.1c) from 1 April to 11 June 2015 (two sensors began recording in May). Six submersible ultraviolet nitrate analyzers (SUNA) measured ambient nitrate concentrations at 1-hr intervals in the island water column. Location $N1$ provided an upstream boundary condition because it was located 400-m from the mouth of a secondary channel that flows into the island interior. The nitrate data are presented as raw and filtered time series, along with a spatially-interpolated mean concentration field in Figure 4.3. To quantify the general spatial patterns in nitrate concentration within the island a 7-day frequency low-pass Butterworth filter [*Roberts and Roberts*, 1978] was applied to the raw time series (Figure 4.3b). Consistently high concentrations of nitrate were observed at locations $N1$ and $N6$ during the observation period and had mean concentrations of 64.6 and 66.3 μM, respectively. Downstream of $N1$ nitrate concentrations generally decreased, suggesting that nitrate removal had occurred. Using mean concentrations and taking the mean concentration at $N1$ as the baseline concentration from which to calculate fractional removal of nitrate, locations $N2$, $N3$, $N4$, and $N5$, saw nitrate removals of 47%, 91%, 55%, and 52%, respectively. Location $N6$ had concentrations that were similar to $N1$, which is due to the channel-island connectivity near the sensor that introduced significant inflow from the main channel. These in situ measurements offer a meaningful

comparison for the nitrate removal estimates generated in section 4.5.

4.3 Numerical Model Description

4.3.1 Hydrodynamic model description

A hydrodynamic model is used to quantify the channel-island hydraulics, the water flux between the channel and the island (i.e., the hydrological connectivity), and the RTD for the idealized channel-island complex. The hydrodynamics are modeled in two horizontal dimensions with the Fine Resolution Environmental Hydrodynamics model (Frehd), which is a numerical code that implements the established computational schemes of *Casulli and Cheng* [1992], *Casulli and Cattani* [1994], *Hodges et al.* [2000], *Stelling and Zijlema* [2003], *Hodges* [2004], *Hodges and Rueda* [2008], and *Hodges* [2014].

4.3.2 Hydrodynamic model governing equations

The present work uses Frehd options for depth-integrated solution of the hydrostatic Navier-Stokes equations with the Boussinesq approximation (i.e. shallow-water equations), which can be written as

$$\frac{\partial u_i}{\partial t} + u_j \frac{\partial u_i}{\partial x_j} + g\frac{\partial \eta}{\partial x_i} - \nu_e \frac{\partial^2 u_i}{\partial x_j \partial x_j} + \frac{C_B\,|V|}{2H} u_i = 0 \quad : \quad i = \{1, 2\} \tag{4.1}$$

$$\frac{\partial \eta}{\partial t} + \frac{\partial}{\partial x_j} H u_j = 0. \tag{4.2}$$

where a modified Einstein summation convention is used for summation over $j = \{1, 2\}$ for repeated subscripts, u_i are the depth-averaged horizontal velocities in the x_i directions, $V = (u_1^2 + u_2^2)^{1/2}$ is the magnitude of the horizontal speed, g is

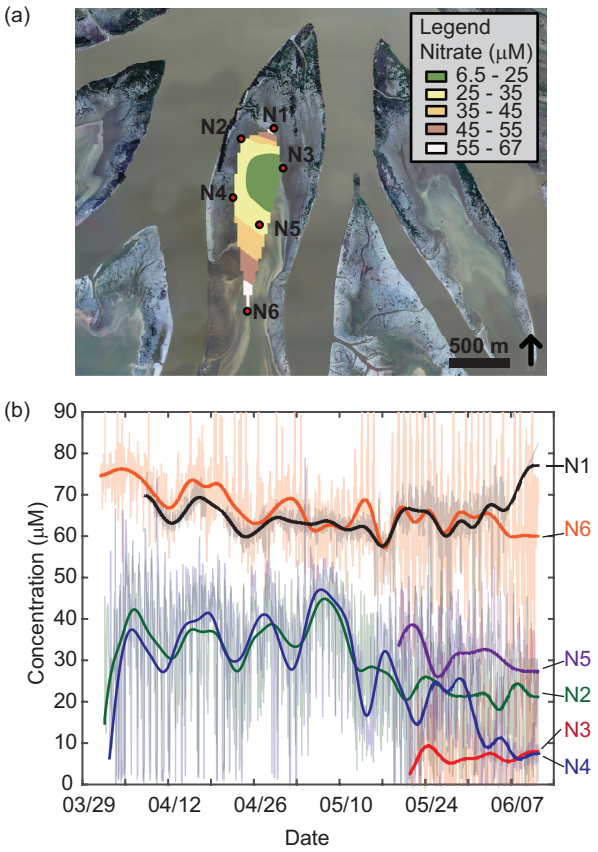

Figure 4.3: Summary of the nitrate concentration measurements from Mike Island in spring 2015. (a) Locations of the SUNA stations measuring nitrate concentration on Mike Island with a spatially interpolated grid of average concentrations for the study period. (b) Raw and filtered time series of the nitrate measurements (see Section 4.2). The bold lines are the filtered signals while the background represents the unfiltered signal.

the gravitational acceleration, ν_e is a horizontal eddy viscosity, C_B is the bottom drag coefficient, H is the local depth, η is the free surface elevation, and t is time. Turbulence in 2D hydrodynamics is typically comprised of a turbulence model (e.g. $k-\epsilon$) for the horizontal ν_e and an a priori assigned C_B. For the purposes of this study, we assume that (1) local turbulence production is equal to local dissipation, and (2) bottom drag dominates turbulent dissipation due to horizontal shear, i.e. $|2\nu_e H\partial^2 u/\partial x^2| \ll C_D u^2$, which makes unnecessary the spatial complexities of a $k-\epsilon$ turbulence model so that a small uniform value of ν_e can be applied. These are reasonable approximations for a model of grid resolution Δx where $\Delta x \gg H$ and Froude number Fr $\ll 1$. For the present purposes ν_e was set to 0.01 m^2 s^{-1} for the cases presented. The coefficient of drag, C_B, is related to the Chezy coefficient, C_Z, as $C_B = gC_Z{}^{-2}$.

A diffusive tracer is used to quantify the RTD within the channel-island complex. Tracer transport within Frehd is based on the conservative advection/diffusion equation for the concentration (c)

$$\frac{\partial c}{\partial t} + u_j \frac{\partial c}{\partial x_j} + \kappa_e \frac{\partial^2 c}{\partial x_j \partial x_j} = 0 \tag{4.3}$$

where κ is the eddy diffusion coefficient. The numerical discretization method within Frehd uses upwind conservative advection schemes [*Hodges*, 2014] that enforce the consistency with the continuity condition of *Gross et al.* [2002] to ensure that the discrete motion of the free surface is exactly accounted for in the discrete scalar transport solution.

4.4 Numerical Modeling Approach

4.4.1 Model domain and setup

The computational domain is based on typical channel-island topography and geometry at WLD (Figure 4.2). We define the channel-island complex based on the conceptualization for hydrological connectivity between primary distributary channels and delatic island from *Hiatt and Passalacqua* [2015] (Figure 4.2b). The test domain is a 7.5-km by 2-km idealized channel-island complex (Figure 4.2c). The length of the domain is similar to the subaerial longitudinal extent of Mike Island (Figure 4.1a) and the width corresponds to a typical distributary channel width flanked by two WLD islands. A 500-m wide central channel extends 15 km through the channel-island complex with an adverse bed slope of 1.33×10^{-4}, rising to the bay elevation of z = -1.5 m (geometry and slope of Gadwall Pass in Figure 4.1a). Flanking the channel are idealized islands with linearly sloping beds and levees. In the baseline model setup, the levee slopes from z = 0.5 m at 107.5 km to z = -0.5 m at 115 km, while the adjacent island bed slopes from z = 0.5 m to z = -1.5 m (Figure 4.2c). These slopes and elevations represent typical values for Mike Island.

The test domain is nested within a buffer domain comprising 3.75×10^{5} cells (Figure 4.2d) to ensure that artificial upstream and bay boundaries do not influence the dynamics within the test domain. A 7.5x7-km bay with open boundaries is at the downstream end of the domain. Upstream of test domain is a 500-m wide, 100-km long channel with a bed slope of $7\text{x}10^{-5}$ (the slope of the Atchafalaya River [*Edmonds*, 2012]) to ensure that upstream tidal propagation is damped prior to the upstream boundary to prevent spurious reflections.

The model grid uses uniform rectangular cells of 50 m $\times$ 50 m, which was chosen to balance computational efficiency with the resolution required to capture kilometer-scale fluid dynamics. Model runs at grid sizes of 25 m $\times$ 25 m and 100 m $\times$ 100 m yielded similar results to those presented herein. An alternative model grid in which flow was topographically blocked from entering the islands (i.e., the channel simply debouching into the bay through a confined channel) was also created and is herein referred to as the "confined" channel case.

4.4.2 Model runs and analyses

We test the effects of hydraulic roughness (C_B), river discharge (Q_R), and tidal amplitude (A) on channel-island exchange and RTD (Table 4.1) for nominal water surface elevations of $\eta = 0$ (i.e., the mean of the tidal range). Q_R ranges from 300 to 1100 m^3 s^{-1} and is held constant for the duration of each run. The range of Q_R is representative of the range of discharges observed in two primary distributary channels at WLD during non-flood conditions [*Hiatt and Passalacqua*, 2015]. The downstream water level is maintained at a constant $\eta = 0$ m in the baseline ($A(t) = 0$ m) case. Our analyses use model results for the discharge and water surface elevation (η) profiles along transects $a - a'$ and $b - b'$ (Figure 4.2c). For the tidal cases, a 12-hour harmonic water level fluctuation with $A = 0.25$ m about $\eta = 0$ m is imposed at the basin boundary.

To examine the relative influence of hydraulic roughness, C_B is maintained at 0.005 ($C_z = 44$ $m^{1/2}$ s^{-1}), a typical value for deltaic environments [e.g., *Nardin et al.*, 2016], for the channel and bay, whereas the wetlands use a range of different (uniform) values across the wetlands to simulate the effects of shallow wetland vegetation and test the sensitivity of the flux at the reach scale to different C_B.

Table 4.1: Model parameters for idealized channel-island complex

Symbol	Variable	Value
Δx	along-channel grid size	50 meters
Δy	cross-channel grid size	50 meters
Δt	time step	25 seconds
$C_{B,channel}$	drag coefficient in channel	0.005
$C_{B,island}$	drag coefficient in island	0.001–0.5
A	tidal amplitude	0–0.25 meters
Q_R	river discharge	300–1100 m^3 s^{-1}
α	nitrate removal rate	0.01–10 d^{-1}

We introduce the parameter θ to express the relative C_B scale for different test cases:

$$\theta = \frac{C_{B,wetland}}{C_{B,channel}}. \tag{4.4}$$

The tested conditions are $\theta \in= \{0.2...100\}$ corresponding to $C_{B,wetland} \in \{0.001...0.5\}$. This set covers the range of bed roughness values used to model flow asymmetry in coastal bifurcations [e.g., *Buschman et al.*, 2010]. A modified Chézy coefficient (C_r) for flow through emergent vegetation can be modeled as:

$$C_r = \sqrt{\frac{1}{1/{C_z}^2} + C_D a H (2g)^{-1}} \tag{4.5}$$

where C_D is the coefficient of drag for a vertical cylinder and a is the vegetation density [*Baptist et al.*, 2007]. Using $C_B = g{C_r}^{-2}$ to convert to an equivalent bottom drag coefficient indicates that our values for $C_{B,wetland}$ correspond reasonable values of θ for $C_z = 44$ $m^{1/2}$ s^{-1} and $C_D a h \leq 1$ [*Luhar et al.*, 2008], with $C_D a H \leq 1$ considered a representative dimensionless drag coefficient for sparse vegetation [*Nepf*, 2012].

4.4.2.1 Water residence time distributions

After the hydrodynamic runs reach a dynamic steady state, the RTD is obtained by tracking the propagation of a diffuse tracer within the test domain. The tracer is released as a pulse over one time step with a uniform concentration $c_t = 1$ in each cell within the channel at the upstream boundary of the channel-island complex transect c–c' (Figure 4.2c). The propagation of the tracer is monitored until $< 1\%$ of the scalar mass remains in the test domain. For the tidal ($A = 0.25$ m) cases, the tracer is released during high, falling, low, and rising tide to investigate the role of tidal regime on the RTD. The RTD is calculated at the interface between the delta channel-island complex and the bay (i.e., $x_1 = 115$ km in Figure 4.2c). The RTD is quantified by calculating the probability density function (PDF) and the cumulative distribution function (CDF). The PDF for a pulse input of tracer is defined as:

$$PDF(\tau) = \frac{Q}{M_{in}} c_t(\tau) \tag{4.6}$$

where M_{in} is the initial mass of the scalar, Q is the local discharge, and $c_t(\tau)$ is the local tracer concentration at a given water residence time τ. The PDF is then decomposed into the contributions from the channel and the island as

$$PDF = PDF_{island} + PDF_{channel} \tag{4.7}$$

where PDF_{island} and $\mathrm{PDF}_{channel}$ are marginal probability density functions describing the fractional allocation of tracer to the island and channel environments, respectively. The PDF are integrated to obtain cumulative distribution functions

(CDF) as

$$CDF(\tau) = \int_{\tau=0}^{\tau} PDF(\tau)\, d\tau \tag{4.8}$$

Note that the CDF may exceed 1 for situations in which the tracer exits and reenters the domain due to tidal motion.

4.4.2.2 Nitrate removal model

The hydrodynamic model output is coupled with a simple model for estimating nitrate removal as a function of the RTD within the deltaic islands. We use the RTD generated with the Frehd model as input to the nitrate model. The fractional nitrate removal (F_R) is quantified with the model of *Dettmann* [2001]:

$$F_R = \frac{\alpha\tau}{1 + \alpha\tau} \tag{4.9}$$

where α is a first-order decay rate [d^{-1}]. F_R represents the mass fraction of nitrate from upstream that is removed. In our case, the decay rate α is used to represent all mechanisms of nitrate removal in the deltaic islands such as mineralization-nitrification-denitrification, immobilization, burial, and plant uptake. While this model was originally developed by *Dettmann* [2001] to quantify nitrate removal on an annual scale using representative values of τ for estuaries, we use the model to quantify the fractional removal for the range of possible τ for the idealized delta channel-island complex. Eq. 4.9 is asymptotic towards 1 as $\tau \to \infty$ and can be interpreted as a theoretical cumulative distribution function for nitrate removal. Since nitrate removal is hypothesized to occur within the deltaic islands [*Henry and Twilley*, 2014] and not in the channels due to relatively low RTD [*Hiatt and*

Passalacqua, 2015], F_R is weighted by PDF_{island} to quantify the fractional nitrate removal associated with the deltaic islands. The flux-weighted nitrate removal ($F_{R,weighted}$) is the integral of the Hadamard (element-wise) product of PDF_{island} and F_R as follows:

$$F_{R,weighted} = \int_{\tau=0}^{\tau} (PDF_{island} \circ F_R)\, d\tau \tag{4.10}$$

Eq. 4.10 can be interpreted as the cumulative distribution function for fractional nitrate removal normalized by the total amount of nitrate entering the channel-island complex. The total fractional nitrate removal is denoted as $F_{R,total}$.

4.5 Results

4.5.1 Channel-island hydrological connectivity

The model runs test the parameter space for Q_R and tidal amplitude A and quantify discharge, Q, and the water surface elevation, η, within the channel and the deltaic islands. The discharge results are normalized by Q_R and are referred to as $\hat{Q}_{channel,L}$ and $\hat{Q}_{island,L}$, the normalized flow in the channel at location L and the normalized flow in the island at location L, respectively. We define L as the distance along transects $a - a'$ and $b - b'$ in the positive x-direction (Figure 4.2b). The flow of water between the channel and the islands is called $\hat{Q}_{exchanged}$ and is defined as positive flowing from the channel to the islands (i.e., $\hat{Q}_{exchanged}$ = 1 - $\hat{Q}_{channel,7500m} = \hat{Q}_{island,7500m}$). Discharges are averaged over three tidal cycles and denoted as $\langle \hat{Q} \rangle$ for runs including tides. Subscripts on $\langle \hat{Q} \rangle$ denote either the channel or the island and the distance L. In all cases, flow is symmetric about $a - a'$ and $\hat{Q}_{island,L}$ and $\hat{Q}_{exchanged}$ include the contributions from both islands in the domain.

4.5.1.1 Influence of discharge

We examine the influence of Q_R on $\hat{Q}_{channel}$ for $Q_R \in \{300...1100\}$ m^3 s^{-1}. $\hat{Q}_{channel}$ decreases with distance downstream through the channel-island complex for all cases, indicating that water flows into the island portion of the domain. However, Q_R has a limited influence on the shape of the $\hat{Q}_{channel}$ profile (Figure 4.4), particularly in the more downstream portion of the domain (two values of θ and three Q_R scenarios are shown in the figure, but similar values were obtained over the full range of Q_R). For low values of L, the deviations among the $\hat{Q}_{channel}$ profiles for both θ cases are relatively large, but the downstream value of $\hat{Q}_{channel}$ is relatively unaffected by the change in Q_R. For example, with $\theta = 1$, the values of $\hat{Q}_{channel,7500m}$ are 0.28, 0.29, and 0.28 for Q_R = 300, 700, and 1100 m^3 s^{-1}, respectively. At $\theta = 10$, $\hat{Q}_{channel,7500m}$ values are 0.53, 0.53, and 0.51 for Q_R = 300, 700, and 1100 m^3 s^{-1}, respectively. For Q_R = 1100 m^3 s^{-1}, $\hat{Q}_{channel,L}$ is generally smaller than the other cases, but its profile approaches that of the other Q_R scenarios with increasing distance downstream (Figure 4.4). In general, $\hat{Q}_{exchanged}$ is insensitive to changes in Q_R. The $\hat{Q}_{channel,L}$ profiles from the idealized channel-island model results are a qualitative match to the discharge values from acoustic Doppler current profiler measurements in two primary channels at WLD by *Hiatt and Passalacqua* [2015] (see Figure 4.4 caption for details). These data are included to how the numerical model of the idealized delta provides similar scales to the observed physics in the more complex real delta. The observed data generally fall within the envelope of the $\hat{Q}_{channel}$ profiles for the range of Q_R and θ tested, except for the measurements taken during the rising tide, which is to be expected since tidal motion is not included in the $A = 0$ m model.

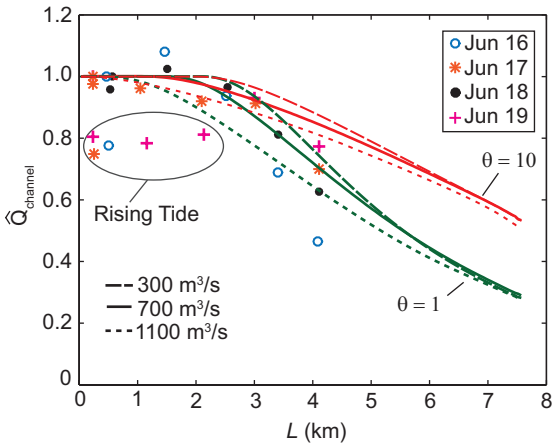

Figure 4.4: Influence of upstream discharge on the fractional discharge profile within the channel compared to the field data from *Hiatt and Passalacqua* [2015]. The green lines indicate $\theta = 1$ and the red lines denote $\theta = 10$. The field data were collected in several transects along two major distributary channels over the course of 4 days in June 2014. The measured discharges of *Hiatt and Passalacqua* [2015] were normalized by the most upstream discharge value for each set of transects (values correspond to falling tide conditions unless noted). The data represent a range of discharge values ($250 \leq Q_R \leq 800$ m^3 s^{-1}) for two adjacent primary channels at WLD. The field data were collected for a limited portion of the channel-island complex, while the modeled results include the more subaqueous portions of the system. See *Hiatt and Passalacqua* [2015] for more information.

4.5.1.2 Influence of hydraulic roughness

The channel water surface profiles and $\hat{Q}_{channel,L}$ along transect $a - a'$ depend on the relative roughness between the channel and islands (Figure 4.5). Overall, we observe lower and flatter water surface profiles along the channel centerline for low values of θ, as compared to the more highly-sloped profiles from the higher values of θ. At $L = 0$ m, the water surface elevation varies about 0.1 m across the set of θ values. All of the profiles approach water surface elevation of $\eta = 0$ m at the downstream end. Accordingly, a steeper water surface slope exists for the higher roughness runs as compared to the lower θ value. For example, the overall water surface slope ranges from 4.2×10^{-5} for $\theta = 10$ to 2.7×10^{-5} for $\theta = 0.2$. Compared to the confined case, the water surface profiles down the length of the channel are generally at least 0.2 m lower throughout the domain. The shape of the water surface profile is also dependent on θ. The profiles tend to be concave up for the relatively low values of θ and concave down as θ increases. The transition in concavity occurs between $\theta = 2$ and $\theta = 5$. The "confined" water surface profile follows an A2 profile (Figure 4.5a) as predicted by gradually-varied open channel flow theory [e.g., *Henderson*, 1966] for an adversely-sloped channel (Figure 4.2c). The water surface profile for $\theta = 100$ is the closest to the confined case due to its high value of hydraulic roughness for the island portion of the domain. As θ increases, it is logical to expect that the water surface profiles will approach that of the confined channel case since the roughness decreases the fraction of water diverted to the deltaic islands.

There is an increase in the flux of water through the channel mouth for an increase in θ (Figure 4.5b; $\hat{Q}_{channel,7500m} = 0.16,\ 0.29,\ 0.53$ for $\theta = 0.2,\ \theta = 1,$

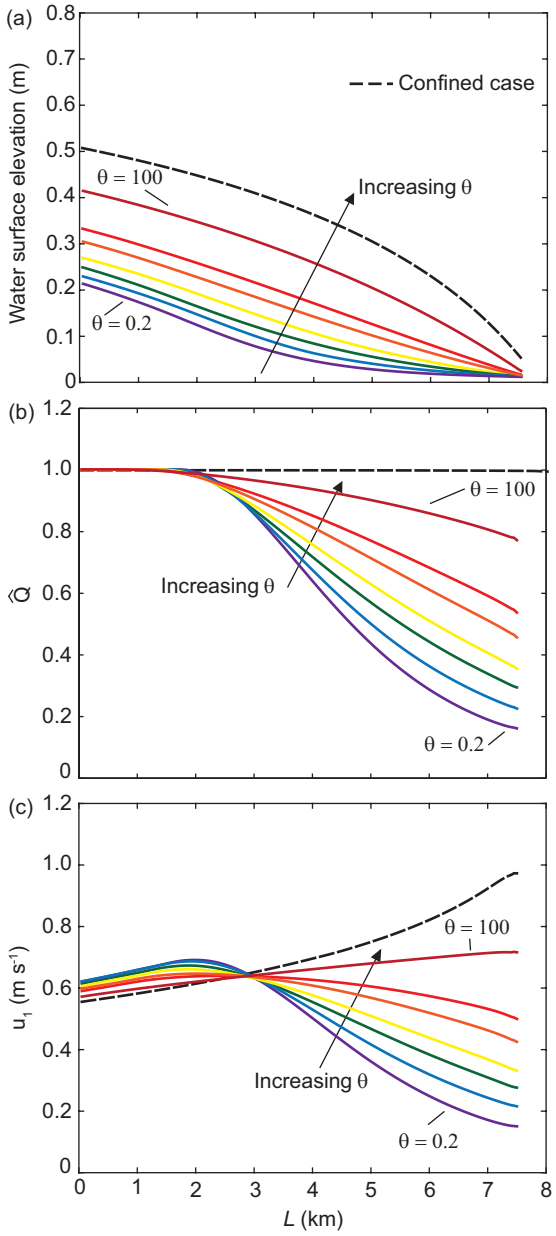

Figure 4.5: Summary of the channel hydraulics for the $Q_r = 700$ m^3 s^{-1} and $A = 0$ m case. Various values of θ are shown: $\theta = 100$ (dark red); $\theta = 10$ (red); $\theta = 5$ (orange); $\theta = 2$ (yellow); $\theta = 1$ (green); $\theta = 0.5$ (blue); $\theta = 0.2$ (purple). (a) Water surface profiles along transect $a - a'$ for various values of θ and a confined channel case (see text). As θ increases, water surface profile approach that of a confined channel. (b) Normalized discharge profiles through the channel portion of the channel-island complex for the set of θ values. Increasing θ leads to an increase in the amount of water retained within the channel. In other words, increasing θ decreases the hydrological connectivity with the deltaic islands.

Figure 4.5 (cont.): (c) Streamwise velocity (u_1) profiles along transect $a - a'$. Increasing θ leads to an increased streamwise velocity along the channel centerline.

and $\theta = 10$, respectively). As such, more water is allocated to the islands for low values of θ, since the flow resistance is lower. Similar to the water surface profiles, the $\hat{Q}_{channel}$ profile is concave up for relatively low θ values and transitions to a concave down profile for the higher θ values. $\hat{Q}_{exchange}$ decreases as θ increases. For example, $\hat{Q}_{exchange}$ for $\theta = 0.2$ is 365% greater than $\hat{Q}_{exchange}$ for $\theta = 100$ (Table 4.2).

The relative hydraulic resistance influences the channel centerline velocity; higher θ values tend to produce higher centerline velocities in the downstream portion of the channel (Figure 4.5c). At the downstream boundary of the channel-island complex ($L = 7.5$ km), the water surface elevations of the model runs for θ are nearly the same (Figure 4.5a), but the discharge at the same location is significantly different (Figure 4.5b), which leads to the differences in velocity (Figure 4.5c). When $\theta > 10$, the channel centerline velocity increases with distance downstream. However, for the majority of θ values tested, streamwise centerline velocity initially increases in the upstream portion of the channel up until $L \approx$ 3 km, where u_1 begins to decrease in the downstream direction (Figure 4.5c). The transition from increasing to decreasing velocity roughly coincides with the distance downstream at which flow begins to enter the deltaic islands (Figure 4.5b).

4.5.1.3 Influence of tides

Discharges are averaged over three tidal cycles and denoted as $\langle \hat{Q} \rangle$ for runs including tides. We measure tidally-averaged discharge exchange ($\langle \hat{Q} \rangle_{exchanged}$) and

compare it to the discharge exchanged for the non-tidal case ($\hat{Q}_{exchange}$). For the model runs with $A = 0.25$ m and $Q_R = 700$ m^3 s^{-1}, $\langle\hat{Q}\rangle_{exchanged}$ is very similar to $\hat{Q}_{exchange}$ for the range of θ values tested (Table 4.2), deviating only slightly at the very high values of θ. A similar trend is observed for the range of Q_R, indicating that tides have a limited effect on the average percentage of water fluxed into the island environment from the channel, especially when the relative roughness is low.

Table 4.2: Summary of $\hat{Q}_{exchanged}$ for $Q_R = 700$ m^3 s^{-1} for non-tidal ($A = 0$ m) and tidal ($A = 0.25$ m) cases. For the tidal case, the normalized discharge is average over three tidal cycles ($\langle\hat{Q}\rangle_{exchanged}$).

	$A = 0$ m	$A = 0.25$ m
θ	$\hat{Q}_{exchanged}$	$\langle\hat{Q}\rangle_{exchanged}$
0.2	0.84	0.84
0.5	0.78	0.78
1	0.71	0.71
2	0.65	0.65
5	0.55	0.56
10	0.47	0.48
100	0.23	0.26

The ranges of $\hat{Q}_{channel,L}$ and $\hat{Q}_{island,L}$ for $A = 0.25$ m show that both θ and Q_R exert control on the discharge fluctuations in the channel-island complex (Figure 4.6). For both the island and the channel, $\langle\hat{Q}\rangle$ is calculated along with the maximum discharge value at a given distance L ($\hat{Q}_{max,L}$) and the associated minimum value ($\hat{Q}_{min,L}$). Therefore, the range of discharge values is defined as $\hat{Q}_{range,L} = \hat{Q}_{max,L} - \hat{Q}_{min,L}$. It is worth noting that $\hat{Q}_{max,L}$ and $\hat{Q}_{min,L}$ are not average values, but simply the maximum normalized discharge observed at a given location during the model run. Note that the range for $\hat{Q}_{island}$ collapses for $L < 1$ km because the furthest upstream area of the island domain remains dry in all simulated cases.

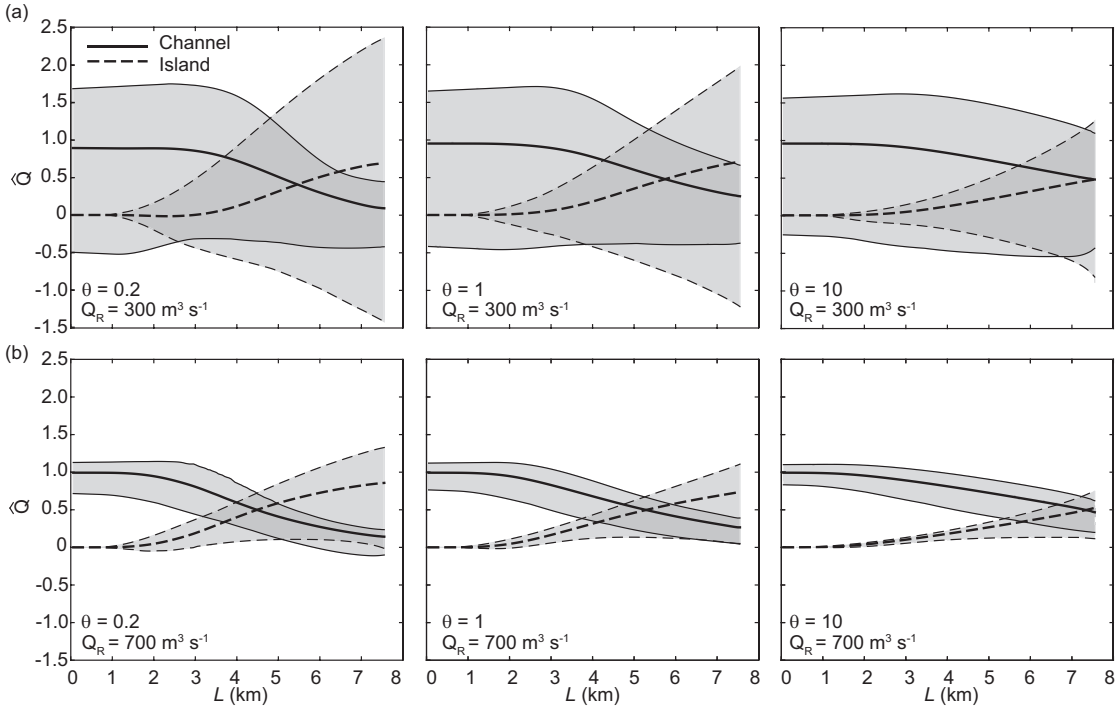

Figure 4.6: Ranges of discharge profiles for $\theta = 0.2$, $\theta = 1$, and $\theta = 10$ for the (a) $Q_R = 300$ m^3 s^{-1} and (b) $Q_R = 700$ m^3 s^{-1} cases. Solid lines indicate channel profiles (transect $a - a'$ in Figure 4.2c) and dashed lines are island transects ($b - b'$ in Figure 4.2c). The bold lines delineate the tidally-averaged discharge profiles for each case and the upper and lower bounds indicate the extreme values for discharge at each distance L (i.e., the upper line delineates the profile of maximum normalized discharges, $\hat{Q}_{max,L}$, and the lower line delineates the minimum, $\hat{Q}_{min,L}$).

These results point to the role of relative roughness in coupled channel-island hydraulics. In all cases, $\hat{Q}_{range,7500m}$ within the channel is smaller than that of the island, but $\hat{Q}_{range,7500m}$ for the island becomes increasingly similar to $\hat{Q}_{range,7500m}$ for the channel as θ increases (Figure 4.6). This is because larger θ values cause larger $\hat{Q}_{range,7500m}$ values in the channel and a decrease in $\hat{Q}_{range,7500m}$ in the island. For example, when $Q_R = 300$ m^3 s^{-1}, $\hat{Q}_{range,7500m}$ in the channel is 0.87 and 1.53 for $\theta = 0.2$ and 10, respectively as compared to $\hat{Q}_{range,7500m}$ in the island, which is 3.79 for $\theta = 0.2$ and 2.08 for $\theta = 10$. In the channel, $\hat{Q}_{range,0m}$ slightly decreases with increasing relative roughness for all Q_R tested. Patterns in $\hat{Q}_{range,L}$ values due to θ as described above hold true for each value of Q_R tested.

For $Q_R = 300$ m^3 s^{-1}, $\hat{Q}_{range,L}$ is significantly larger in both the channel and the island than for $Q_R = 700$ m^3 s^{-1} (Figure 4.6). For $\theta = 1$ and $Q_R = 300$ m^3 s^{-1}, channel $\hat{Q}_{range,7500m}$ and island $\hat{Q}_{range,7500m}$ are 0.49 and 1.33, respectively. For the same scenario, but with $Q_R = 700$ m^3 s^{-1}, channel $\hat{Q}_{range,7500m}$ and island $\hat{Q}_{range,7500m}$ are 0.39 and 1.01, respectively. Q_R tends to dampen the effect of tides, causing a 20-24% decrease in $\hat{Q}_{range,L}$.

To further investigate the influence of tides on the hydraulics within the channel and the islands, we calculate the relative influence of river to tidal inflow as

$$R = \frac{V_R}{P} \tag{4.11}$$

where P is the tidal prism and the volume of water fluxed by the river during a tidal period, V_R, is the product of Q_R and the tidal period T [*Luketina*, 1998]. The tidal prism is calculated as the volume of water contained within the system between low and high tide. We use Eq. 4.11 to determine threshold behavior for

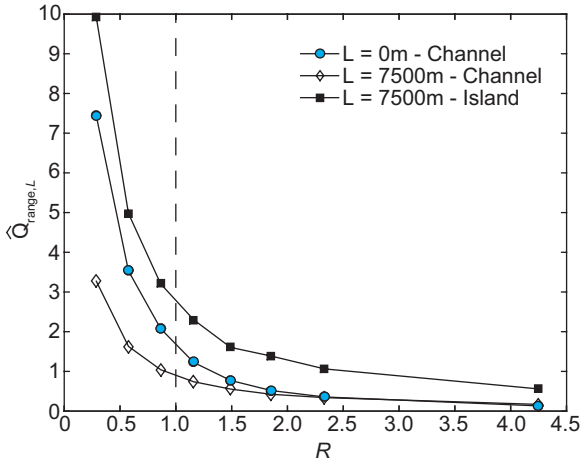

Figure 4.7: The influence of R on the Q ranges within the channel and the island for $\theta = 1$. Each curve decays as a power law with exponents ranging from -1.1 to -1.5.

the channel-island hydraulics and RTD. R ranges from 0.29 for $Q_R = 100$ m^3 s^{-1} to 4.24 for $Q_R = 1100$ m^3 s^{-1}. $\hat{Q}_{range,L}$ decreases exponentially as R increases (Figure 4.7). Within the island, $\hat{Q}_{range,7500m}$ values are consistently larger than those within the channel. At $R >\sim 2$, the $\hat{Q}_{range,L}$ is similar at both $L = 0$ m and 7500 m within the channel, indicating that tides have a limited effect when Q_R is relatively large. Tides have a greater effect within the channel in the upstream region when compared to the downstream, which may be due to the greater depth at $L = 0$ m and tidal amplification due to the confinement of the channel in this region.

4.5.2 Residence time distributions and nitrate removal

The RTD and nitrate removal are quantified based on the hydrodynamic modeling results coupled with the numerical tracer propagation within the test domain. We present the calculated RTD and nitrate removal for $Q_R = 300$ and 700 m^3 s^{-1} for

both the non-tidal ($A = 0$ m) and tidal cases ($A = 0.25$ m) only. The patterns described in the following sections hold true for the range of parameters tested.

4.5.2.1 Influence of discharge

The CDF for the $Q_R = 300$ m^3 s^{-1} show longer tails and increased residence times compared to the 700 m^3 s^{-1} case (Figure 4.8a). A decrease in Q_R leads to an increase in the median residence time (Table 4.3), as expected, and increases the interquartile range (IQR). The interquartile ratio, defined as the IQR divided by the median, is consistent across Q_R values (Table 4.3), indicating that Q_R does not affect the relative dispersion of the calculated RTD. The lack of influence of Q_R on the relative dispersion of the RTD is also manifested in the unchanging shape of the CDF between the two Q_R scenarios (Figure 4.8a). The shape of the CDF is unchanged with the change in Q_R aside from the shift in median value. In summary, Q_R only affects the nominal values of the RTD but does not influence the shape of the distribution nor the tail behavior. Accordingly, $F_{R,weighted}$ increased as Q_R decreased (see below)

4.5.2.2 Influence of hydraulic roughness

Q_R exerts a control on the median and IQR of the RTD, but not on the shape of the RTD. However, θ influences the shape of the distribution and can significantly increase the extreme values of the distribution (Figure 4.8b). For the $Q_R = 700$ m^3 s^{-1} case, the median residence times range from 3.28 to 5.04 hrs for the range of θ tested (Table 4.3). Increases in θ act to decrease the median residence time, since more water and tracer are retained in the faster-moving channel. The IQR tends

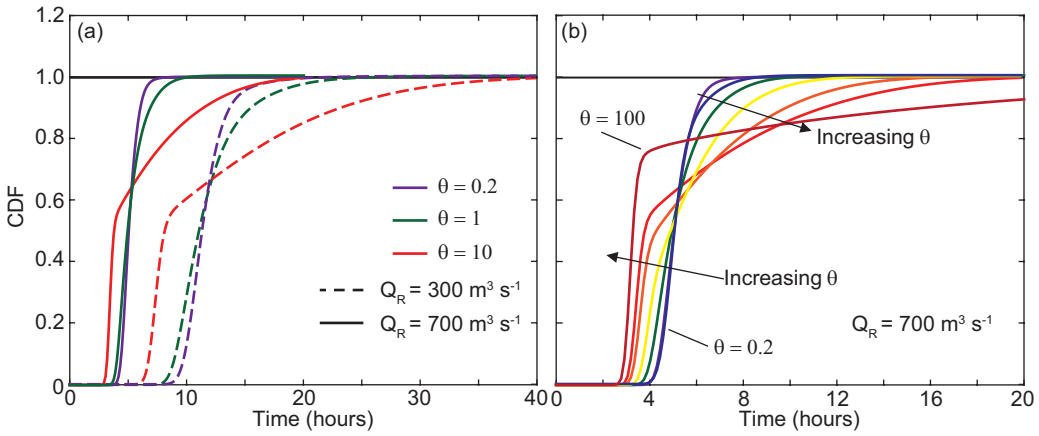

Figure 4.8: Representation of the RTD in the form of cumulative distribution functions. Various values of θ are shown: $\theta = 100$ (dark red); $\theta = 10$ (red); $\theta = 5$ (orange); $\theta = 2$ (yellow); $\theta = 1$ (green); $\theta = 0.5$ (blue); $\theta = 0.2$ (purple) (a) The CDFs for two different values of Q_R. In this case, only $\theta = 0.2$, 1, and 10 are shown for clarity, but the trends follow (a) for the θ values not shown. (b) The CDF for the $Q_R = 700$ m^3 s^{-1} case for the set of tested θ values. The $\theta = 100$ model run is not completely shown for visualization purposes and comparison with the other runs. The CDF for $\theta = 100$ reaches unity at about 40 hours.

Table 4.3: Summary of tracer statistics for $Q_R = 300$ and 700 $m^3\ s^{-1}$ when $A = 0$ m

$Q_R = 300\ m^3\ s^{-1}$			
θ	Median (hr)	IQR (hr)	$\frac{IQR}{Median}$
0.2	11.34	1.94	0.17
1	11.06	3.10	0.28
10	8.14	8.02	0.98

$Q_R = 700\ m^3\ s^{-1}$			
θ	Median (hr)	IQR (hr)	$\frac{IQR}{Median}$
0.2	5.04	0.85	0.17
0.5	5.06	0.78	0.15
1	4.94	1.38	0.28
2	4.89	2.37	0.48
5	4.28	3.43	0.80
10	3.79	3.86	1.02
100	3.28	0.76	0.23

to increase with increasing θ along with the interquartile range, before decreasing sharply when $\theta = 100$.

The shape of the marginal island and channel PDF provide insight into the timing, duration, and magnitude of water flux to the island. In general, as discussed in the above sections, $\hat{Q}_{exchange}$, which is also represented by the area under the PDF_{island} curve, decreases with increasing θ (Figure 4.9a). The PDF_{island} has a less pronounced peak as θ increases, while the $\text{PDF}_{channel}$ peak becomes increasingly pronounced and accounts for a larger mass within the total PDF (Figure 4.9a), since more water flux is contained within the channel. The timing of the peak of the PDF decreases as θ increases, owing to the increased velocities through most of the channel associated with larger θ values. The tail of the distribution lengthens as θ increases, which indicates that the extreme values of the RTD increase (Figure 4.9a). In general, the peak of the $\text{PDF}_{channel}$ precedes

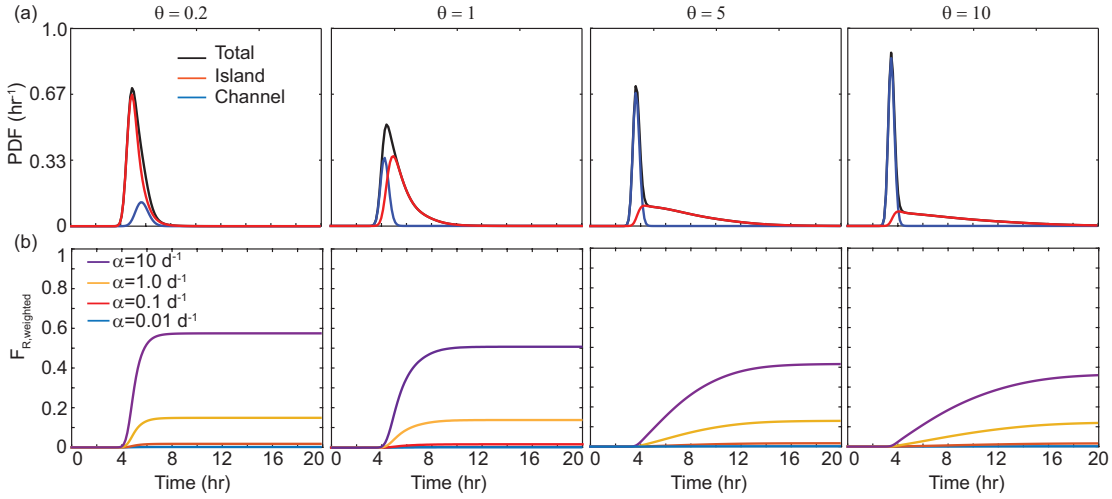

Figure 4.9: Summary of RTD and nitrate removal for Q_R = 700 m^3 s^{-1} and A = 0 m. The RTDs are quantified with probability density functions (PDF). (a) PDFs for various values of θ. The total PDF distribution is decomposed into the marginal contributions from the channel and island portions of the domain (Eq. 4.7). Increases in θ cause decreases in the volume of water entering the island (represented here by the area under the island PDF). (b) Cumulative fractional nitrate removal for various values of α calculated with Eq. 4.10. A decrease in the nitrate removal occurs when θ increases, due to the overall decrease in the flux to the islands.

the peak of the PDF$_{island}$ because the channel velocities are generally higher than island velocities. For θ = 0.2, the peak of the PDF$_{island}$ precedes that of the channel (Figure 4.9b), due to the increased island velocities associated with the decrease in hydraulic roughness and relatively low channel velocities (Figure 4.5c).

While increased island roughness causes an increase in the extreme values of the RTD, it also causes a general decrease in the fraction of nitrate removed from the system (Figure 4.9b). The shape of the $F_{R,weighted}$ curve becomes more dispersive as θ increases, due to the longer tail in the island RTD. Lower values of α result in lower values for $F_{R,weighted}$ in all cases. The α = 0.01 d^{-1} scenario results in nearly zero nitrate removal for all the scenarios presented. The value

of $F_{R,weighted}$ at the end of the model run represents the total fraction of nitrate removed ($F_{R,total}$) from the system. $F_{R,total}$ ranged from ~0 to 0.56 for the tested ranges of α and θ. For the $\alpha = 10$ d^{-1} scenario, $F_{R,total}$ decreased from 0.56 to 0.36 for $\theta = 0.2$ and $\theta = 10$, respectively. For each value of α, the $F_{R,total}$ decreased as the relative roughness increased. The maximum change in $F_{R,total}$ of 0.20 exemplifies the control of θ and the amount of water flux delivered to the island on nitrate removal.

4.5.2.3 Influence of tides

Tides have a limited effect on the RTD and $F_{R,weighted}$ for $R > 1$ (example for $Q_R =$ 700 m^3 s^{-1} in Figure 4.10). For the $Q_R = 700$ m^3 and $A = 0.25$ m with $\theta = 1$ case, the shape of the PDF is similar for all tracer release scenarios (high, falling, low, and rising) and the area under PDF$_{island}$ is relatively unchanged (Figure4.10a). Minor deviations in the shape of the distributions are observed, namely the bump in the falling tide release occurring about nine hours after the tracer was released, which indicates a flow stagnation or slight flow direction reversal. Accordingly, the estimates of $F_{R,weighted}$ do not seem to be significantly affected by the timing of the tracer release (Figure 4.10b). For example, over the four different release times $F_{R,total} = 0.12 - 0.16$ and $0.47 - 0.54$ for $\alpha = 1$ and 10, respectively. For comparison, when $A = 0$ m , $F_{R,total} = 0.15$ and 0.54 for $\alpha = 1$ and 10, respectively.

In contrast, for $R < 1$, tidal effects significantly influence the tracer transport, which alters the shape of the RTD, generally increases residence times, and increases nitrate removal estimates (Figure 4.11). The model run with $Q_R = 300$ m^3 s^{-1}, $\theta = 1$, and $A = 0.25$ m is used to illustrate these effects. In all of the tracer release scenarios, return peaks are observed after the initial propagation of

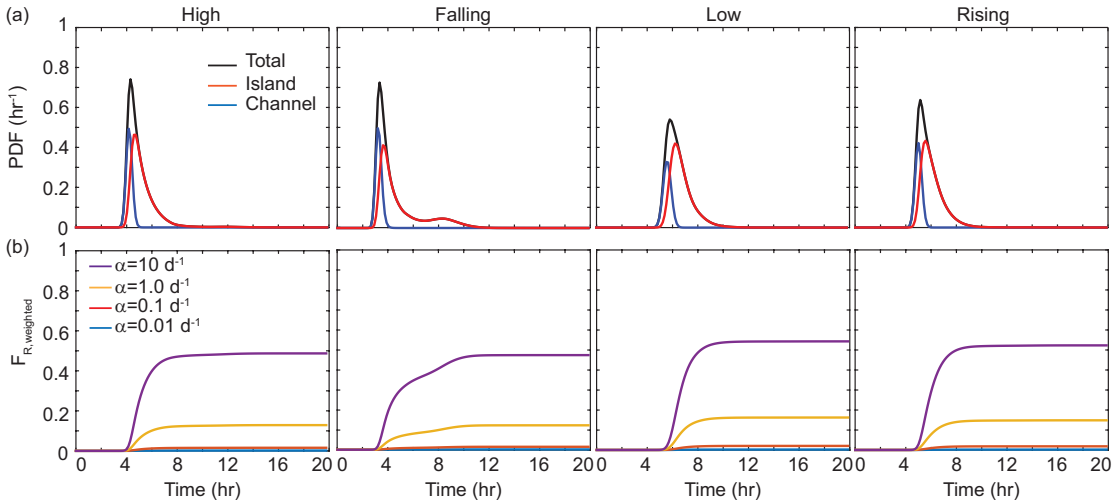

Figure 4.10: The influence of tides during high discharge on RTD and nitrate removal ($Q_R = 700$ m^3 s^{-1}, $\theta = 1$, $A = 0.25$ m) (a) PDFs for tracer releases at high, falling, low, and rising tides. (b) Cumulative fractional nitrate removal for each scenario.

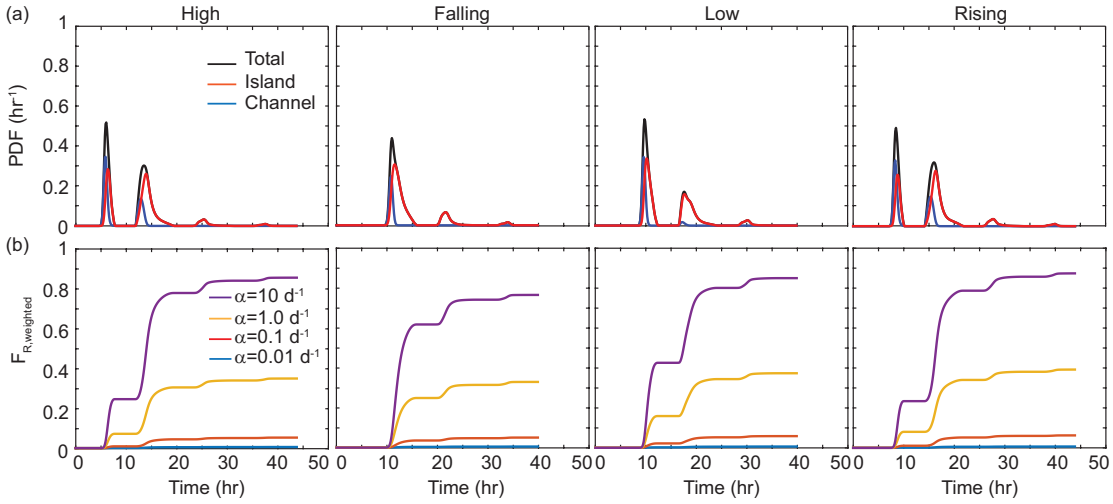

Figure 4.11: The influence of tides on RTD and nitrate removal during low discharge ($Q_R = 300$ m^3 s^{-1}, $\theta = 1$, $A = 0.25$ m) (a) PDFs for tracer releases at high, falling, low, and rising tides. The return peaks indicate the tracer was fluxed through the seaward boundary of the channel-island complex then reentered, before again being flushed out. (b) Cumulative fractional nitrate removal for each scenario. The return peaks cause a step-like curve for each value of α.

the tracer through the channel-island complex, leading to increased residence times (Figure 4.11a). Within the return peaks, the majority of the tracer flux is allocated to the islands. In some cases, the tracer flux reentering the islands is greater than the initial tracer flux within the islands, which is due to the spreading of the flow at the channel mouth. Accordingly, the increased residence time and flux allocation to the island leads to increased values of $F_{R,weighted}$ (Figure 4.11b). A step-like curve describes the cumulative fraction of nitrate removed in accordance with the multi-peak PDF_{island}. Since the first return peak fluxes a relatively large amount of the tracer to island, the increase in $F_{R,weighted}$ associated with the return peak is often larger than the initial increase, which is evident in the high and rising tide tracer release conditions (Figure 4.11b).

The increased RTD and water flow to the island environment leads to significant increases in $F_{R,total}$ compared to the case without tides. We illustrate this behavior by comparing the above results to those of the $Q_R = 300$ m^3 s^{-1}, $\theta = 1$, and $A = 0$ m case (Figure 4.12). For the non-tidal condition, $F_{R,total}$ is 0.04, 0.25, and 0.61 for $\alpha = 0.1$, 1, and 10 d^{-1}, respectively. When tides are introduced, $F_{R,total}$ increases to 0.05–0.06, 0.34–0.39, and 0.77–0.87 for $\alpha = 0.1$, 1, and 10 d^{-1}, respectively. Ranges in $F_{R,total}$ are given to show the variation among the tidal conditions during each tracer release (high, falling, low, rising). Accordingly, there is an effect of the timing of the tracer release on the $F_{R,total}$ estimates for $R < 1$. The $F_{R,total}$ for $\alpha = 1$ d^{-1} is less than 0.01 in all cases.

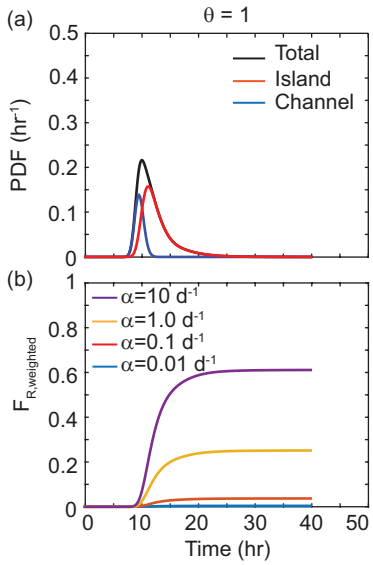

Figure 4.12: Summary of RTD and nitrate removal for Q_R = 300 m^3 s^{-1} and A = 0 m.(a) PDFs for various values of θ. (b) Cumulative fractional nitrate removal for various values of α.

4.6 Discussion

4.6.1 Controls on hydrological connectivity in a channel-island complex

Hydrological connectivity is a key factor in understanding the ecological and morphological implications of water, sediment, and nutrient transport in landscapes and aquatic systems [*Pringle*, 2003; *Fryirs*, 2013; *Bracken et al.*, 2013]. Our study suggests that deltaic islands receive significant flow from the distributary channels ($\hat{Q}_{exchange}$ = 0.23–0.84), and the percentage of flow received depends most importantly on hydraulic roughness, followed by river discharge and tides. This percentage allocation of flow is similar to the 23–54% measured by *Hiatt and Passalacqua* [2015], but their discharge measurements did not extend to the sub-

aqueous distributary channel tips like our idealized channel-island domain does. Additionally, a mass-balance approach based on delta topography at the delta front predicts that 59% of the water at WLD departs the channel and flows into the interdistributary islands [*Shaw et al.*, 2016].

Since river discharge (Q_R) generally has a limited effect on water surface elevation in backwater zones [*Chatanantavet et al.*, 2012], the channel-island hydrological connectivity is not greatly altered by changes in Q_R in our model (Figure 4.4). This notion appears to be true at WLD, since the field discharge measurements of *Hiatt and Passalacqua* [2015] in two distributary channels qualitatively match our $\hat{Q}_{channel}$ profiles (Figure 4.4). The presence of tides have a limited effect on the average percentage of water allocated to the deltaic island in our model results (Table 4.2). However, tides modulate the magnitude and direction of flows within the island interiors and, to a lesser extent, within the channel (Figure 4.6). When the relative influence of river discharge is low compared to tides ($R < 1$), the dynamics within both the channel and the islands are modulated by tides, but the average flux between the two is unchanged regardless of R (bold lines in Figure 4.6). However, our study accounts only for hydrological connectivity in the form of over-bank flow and does not include secondary channels, which have been shown to reverse direction due to tides [*Hiatt and Passalacqua*, 2015]. A full field investigation of the response of distributary channels and the connection to the deltaic islands over the hydrograph and tidal range is warranted to fully characterize this phenomenon.

At the reach scale, marsh vegetation can enhance erosion within tidal channels [*Temmerman et al.*, 2007], due to the non-local hydrodynamic effects of vegetation patches [*Vandenbruwaene et al.*, 2011]. Therefore, in highly hydrologically-

connected channel-island systems, off-channel parameters are of paramount importance for understanding channel dynamics. We find that relative roughness, θ, (i.e., the ratio of drag coefficients in the islands and the channel) exerts a significant control on the flow within the channel by altering water surface profile and lateral exchange (Figure 4.5), which in turn influence the RTD (e.g., Figure 4.9a). Relatively high θ values limit the hydrological connectivity between delta channels and islands (Figure 4.5b), leading to a more confined channel flow, which causes an increase in the flow velocity within the channel (Figure 4.5c). Conversely, when θ is low, the enhanced partitioning of water through the island decreases the flow velocities within the channel (Figure 4.5c). These behaviors have significant implications for sediment transport within distributary channels and indicate that the channel-island hydrological connectivity may control the tendency towards sediment deposition or erosion in distributary channels. Indeed, deltaic distributary channels can be erosional [*Edmonds et al.*, 2011b; *Shaw et al.*, 2013; *Shaw and Mohrig*, 2014], but the reduction in flow momentum within distributary channels due to the hydrological connectivity may facilitate sediment deposition.

The presence of vegetation increases the drag in wetland environments [*Kadlec*, 1990; *Nepf*, 1999; *Nepf and Vivoni*, 2000; *Leonard and Croft*, 2006], but spatial heterogeneity in vegetation communities due to changes in elevation [*Carle et al.*, 2013], patchiness [*Vandenbruwaene et al.*, 2011], seasonality, and scale introduce complexities beyond the scope of this work. While our study uses a simplified, uniform bed roughness within the islands to understand the first-order effects of flow resistance on hydrological connectivity in deltaic systems, more explicit treatment of the drag for flow in a vegetated deltaic island wetland [e.g., *Nardin et al.*, 2016] and accounting for the spatial distribution of vegetation patches [*Marani*

et al., 2013] would provide further insights into the control of vegetation.

Our study does not address the effects of groundwater in channel-island hydrological connectivity. Surface water-groundwater exchange is an important component in hydrological connectivity [*Bracken et al.*, 2013, and reference therein] and biogeochemical transformations [*Gomez et al.*, 2012]. The groundwater dynamics are spatially heterogeneous within Pintail Island at WLD (northeastern island in Figure 4.1a), depending on elevation and levee composition, and recharge is significantly influenced by storms [*O'Connor and Moffett*, 2015]. In general, groundwater flow is directed out of the island near the Pintail Island apex, but tides and storms can cause flow reversals that prolong groundwater residence times [*O'Connor and Moffett*, 2015]. A recent numerical modeling study indicated that exchange rates between surface and groundwater were highest in coarse-grained deltas, owing to the permeability and resulting morphology. Global-scale estimates of groundwater discharge account for only 6% of the inputs to the sea [*Zektser and Loaiciga*, 1993], but much of the water entering a delta system is subject to surface-groundwater exchange [*Sawyer et al.*, 2015], which has implications for nutrient cycling processes. To improve estimates of nutrient removal in deltaic systems, future work should look to determine the relative contributions of surface and groundwater to the RTD.

4.6.2 Residence time distributions and nitrate removal in river deltas

Water residence times are a key factor for the estimation of nutrient removal in coastal systems [*Yu et al.*, 2006; *Rivera-Monroy et al.*, 2010], but estimates of residence times in coastal systems are lacking [*Rivera-Monroy et al.*, 2010]. This study takes the first step in characterizing the processes that control RTD in coastal river

deltas and provides quantitative estimates of RTD in a deltaic channel-island complex. Hydrological connectivity between the channel and deltaic islands is a critical factor in estimating the RTD. Increased flow resistance within deltaic islands due to vegetation slows the flow locally [*Nepf and Vivoni*, 2000], but limits the hydrological connectivity between the channel and the islands (Figure 4.5b), which leads to a larger percentage of the total water flux exiting the system via the faster-moving channel. Therefore, perhaps counter-intuitively, increased flow resistance actually decreases RTD in a channel-island complex, due to the localization of flow within the channel.

Our model results indicate that water residence times in the channel-island complex range from as little as a few hours to nearly two days depending on tides, river discharge, and the relative hydraulic roughness (Figures 4.10a & 4.11a). The results are on the same order as those of *Hiatt and Passalacqua* [2015], who observed tracer travel times on Mike Island of at least 3.8 days. Patches of vegetation, wind, and tides acted to increase residence times [*Hiatt and Passalacqua*, 2015].

While tides have a limited effect on the percentage of water flux allocated to the island (Table 4.2), we find that total nitrate removal ($F_{R,total}$) depends significantly on the relative influence of river discharge and tides (R) and the relative hydraulic roughness (θ). In the absence of tides, Q_R has a relatively minor effect on $F_{R,total}$ (Figure 4.10b). Without tides, nitrate removal efficiencies ($F_{R,total} \times 100\%$) range from $\sim$0 to 58% for $Q_R = 700$ m^3 s^{-1} and from $\sim$0 to 61% for $Q_R = 300$ m^3 s^{-1}; only an increase of 3% efficiency for a large reduction in discharge. However, tides significantly increase the maximum removal efficiency from 61 to 87% for $Q_R = 300$ m^3 s^{-1} (Figure 4.11b). For $R > 1$, $F_{R,total}$ is relatively unaffected by tides (e.g., $\theta = 1$ in Figures 4.9b & 4.10b). Tidal motion

also enhances the potential for nitrate removal by reintroducing water fluxed out of the system back into the island environment when $R < 1$, but does not affect $F_{R,total}$ when $R > 1$. We find that the return peak carries more tracer to the island than the initial peak (Figure 4.11), indicating that tides route flow exiting via the channel back into the island via flow reversal. This increase in tracer mass within the return flow is facilitated by the lateral spreading of the flow at the channel mouth. Our model does not take into account the roles of offshore currents. The return flows associated with tides are likely significantly influenced by offshore currents and should be addressed in future studies.

We use a simple model to describe the fractional removal of surface water nitrate from a coastal deltaic system based on the RTD and a first-order nitrate decay rate (α) [*Dettmann*, 2001]. Applying this model (Eq. 4.9) to the nitrate removal via denitrification data of *Yu et al.* [2006] for the Davis Freshwater Pond Diversion, α is found to range from 0.72 to 3.80 d^{-1}, indicating that the values of α used in our study (0.01 to 10 d^{-1}) are representative of measured values in the region. The removal efficiencies generated by our model compare well to observed trends in nitrate concentrations measured at WLD during the spring/summer of 2015. We observe a 47–91% reduction in nitrate concentration within the island surface water at Mike Island (Figure 4.3a) using the average concentrations measured at each station. These results are comparable to those observed at fixed monthly (March to August 2013 and 2014) water quality monitoring stations established in Mike (30 stations) and Pintail (34 stations) islands using a grid (150×250 m) sampling approach to capture surface water nitrate concentration variability during peak spring-summer Mississippi River flood-pulse season (Castañeda-Moya et al. in preparation). Results from this study indicate that nitrate concentrations

in distributary channels feeding water to island interiors varied from $60-180$ μM, with higher values during the summer. In contrast, surface nitrate decreased to $< 20\mu$M in hotspots along the island edges, but remained around 100 μM (May-June) in the central and distal part of islands, characterized with the lowest elevation. Overall, low surface nitrate values were associated with shallow vegetated areas and higher water residence time and water temperature (Castañeda-Moya et al. in preparation). Our modeled and measured nitrate removal efficiencies also compare well to those observed in Louisiana coastal islands receiving Mississippi River water [*Lane et al.*, 2003, and references therein]. For example, using direct measurements of denitrification and a denitrification model, *Yu et al.* [2006] show that the retention time of ponded surface water is the major control on nitrate removal efficiency in the Davis Pond Freshwater Diversion Project ponding area, with removal efficiencies ranging from 42±2.5% to 95±0.5% depending on water residence time ranging from 1 to 5 days.

While our nitrate removal model is useful for system-scale estimates [*Dettmann*, 2001], numerous factors influence nutrient processes in coastal wetland environments. Nitrogen transformation in wetland environments generally occurs via fixation [*Howarth et al.*, 1988], mineralization [*Zak and Grigal*, 1991], nitrification [*Mitsch and Gosselink*, 1993], annamox [*Erler et al.*, 2008], and denitrification [*Bowden*, 1987; *Yu et al.*, 2006; *Rivera-Monroy et al.*, 2010]. Plant uptake and nitrogen immobilization by microbial communities and vegetation also occur [*Yu et al.*, 2006]. Significant deposition of inorganic sediments can also lead to burial of inorganic nitrogen [*Smith et al.*, 1985]. Long surface water residence times can promote diffusion of nitrate into the anaerobic wetland sediments when denitrification can occur [*Rivera-Monroy et al.*, 2010]. Nitrate concentrations in coastal

wetlands are variable due to changes in temperature, loading [*Lane et al.*, 2004], and the amount of overbank flow [*Hyfield et al.*, 2008]. Soil organic matter content [*Henry and Twilley*, 2014] also influence nitrate removal rates via denitrification. Our study is limited by the assumption of a constant first-order decay rate, when the removal rate of nitrate is likely spatially and temporally dynamic within deltaic wetlands due to the combination of the above factors. Additionally, while the increased drag associated with vegetation limits hydrological connectivity and thus causes a reduction in nitrate removal (Figure 4.9), ecological feedbacks exist among vegetation, nutrient uptake, and sedimentation [*Ortiz et al.*, 2013] that are not accounted for in our model.

4.6.3 Implications for coastal river diversions

Our results indicate that channel-island hydrological connectivity should be considered when designing and evaluating coastal restoration projects. We find that enhancing the connectivity between the channel and island environments promotes increased nutrient removal due to the increased residence times. Longer water residence times associated with increased hydrological connectivity can exacerbate the risk of harmful algal blooms [*Twilley and Rivera-Monroy*, 2009; *Rivera-Monroy et al.*, 2010]. However, the nitrate removal we and other studies [e.g., *Lane et al.*, 2003] observed within islands limits the potential for toxic blooms which are dependent on nitrogen input [*Rivera-Monroy et al.*, 2010].

For the case of land-building diversions in the Mississippi River Delta, *Allison and Meselhe* [2010] indicate that large, deep sediment diversions that convey large volumes of water would best facilitate sand transport [*Meselhe et al.*, 2012] and rapid land-building and wetland creation/preservation. On the other hand,

our results indicate that deltaic channel-island complexes are most efficient at removing nitrate when the hydraulic influence of tides is greater than that of the river (i.e, $R > 1$; see Figure 4.11b). Therefore, river diversion conveying relatively low flow may be subject to flow direction reversals due to tides that increase RTD and nutrient removal. In practice, this means that many, relatively small discharge river diversions may be more adept at removing nitrate than sparse, large-scale diversions and may be more economically beneficial [*Turner and Boyer*, 1997]. However, taking into account the morphology and evolution of the prograding WLD, an analog for a successful land-building diversion [*Allison and Meselhe*, 2010], it may be expected that large-scale water/sediment diversions could produce delta networks comprising channel and islands, which act to distribute flow throughout the deltaic floodplain, leading to lower R values in systems subject to tides. Therefore, the relative forcing from the riverine input compared to tides should be considered when designing and locating river diversion sites.

4.7 Conclusions

We investigated the processes controlling hydrological connectivity, water residence time distributions, and nitrate removal in a river delta channel-island complex. We used two-dimensional hydrodynamic and scalar modeling to quantify the channel-island hydrological connectivity and water residence time distributions in an idealized delta channel-island complex subject to variations in river discharge, tidal amplitude, and hydraulic roughness. We then applied a simple model to estimate nitrate removal based on the marginal water residence time distribution associated with the island interior and compared those results to field measurements of surface water nitrate concentrations within a island at the Wax Lake Delta in

coastal Louisiana. The results improve our understanding of the processes controlling hydrological connectivity in river deltas and provide estimates of RTD for a channel-island complex for a range of environmental conditions. This work also has implications for restoration of ecological processes in coastal wetlands and the broader understanding of the influence of hydrological connectivity on water quality.

From these analyses, we found that a significant portion of the water entering the deltaic channel-island complex is allocated to the deltaic islands and that water residence time distributions and nitrate removal are strongly linked to channel-island hydrological connectivity. The relative hydraulic roughness between the deltaic islands and the distributary channel exerts a strong control on the amount of water fluxed from the channel to the island environment. Increased hydraulic roughness within the inundated islands causes an increase in the streamwise velocities in the distributary channel and reduces velocities within the island. The water residence time distribution is controlled by the amount of water entering the deltaic islands and by the relative influences of river discharge and tides. The fractional nitrate removal decreases with increasing island hydraulic roughness, since the increased roughness limits channel-island hydrological connectivity. Tides can increase residence times within the channel-island complex when the tidal influence is greater than that of the river discharge, which leads to larger fractions of nitrate removal. This study demonstrates the importance of hydrological connectivity in deltaic processes and extends our understanding of the interactions between hydraulics and nutrient dynamics in coastal deltaic wetlands.

Notation

Symbol	Description
WLD	Wax Lake Delta
WLO	Wax Lake Outlet
RTD	water residence time distribution
x_i	horizontal directions
u_i	depth-average horizontal velocity [m s^{-1}]
V	magnitude of horizontal speed [m s^{-1}]
g	gravitational acceleration [m s^{-2}]
ν_e	horizontal eddy viscosity [m^2 s^{-1}]
C_B	bottom drag coefficient [-]
H	local depth [m]
η	free surface elevation [m]
t	time [hr]
Fr	Froude number [-]
C_z	Chézy coefficient [m^2 s^{-1}]
n_b	Manning's coefficient [s $m^{-\frac{1}{3}}$]
κ	eddy diffusivity coefficient [m^2 s^{-1}]
z	bed elevation [m]
Q_R	river discharge [m^3 s^{-1}]
θ	ratio of the island C_B to the channel C_B
n_M	modified Manning's coefficient [s $m^{-\frac{1}{3}}$]
B^{SA}	fraction of transect surface area blocked by vegetation [-]

Continued on next page

Notation – *from previous page*

Symbol	**Description**
c_t	tracer concentration [mass m^{-3}]
PDF	probability density function [hr^{-1}]
Q	local discharge [m^3 s^{-1}]
τ	water residence time [hr]
CDF	cumulative distribution function [-]
F_R	un-weighted fractional nitrate removal [-]
α	first-order decray rate [d^{-1}]
$F_{R,weighted}$	weighted fractional nitrate removal [-]
$F_{R,total}$	total fraction of nitrate removed [-]
$\hat{Q}_{channel}$	normalized discharge in channel
$\hat{Q}_{channel,L}$	normalized discharge in the channel at distance L along transect $a - a'$ [-]
$\hat{Q}_{island,L}$	normalized discharge in the islands at distance L along transect $b - b'$ [-]
L	distance along transect $a - a'$ or $b - b'$ [m]
$\hat{Q}_{exchanged}$	normalized discharge between the channel and the island [-]
$\langle \hat{Q} \rangle$	normalized discharge averaged over three tidal cycles [-]
$\langle \hat{Q} \rangle_{exchanged}$	normalized discharge between the channel and the island averaged over three tidal cycles [-]

Continued on next page

Notation – *from previous page*

Symbol	**Description**
$\hat{Q}_{max,L}$	maximum normalized discharge within the islands at distance L [-]
$\hat{Q}_{min,L}$	minimum normalized discharge within the islands at distance L [-]
$\hat{Q}_{range,L}$	difference between $\hat{Q}_{max,L}$ and $\hat{Q}_{min,L}$ at distance L [-]
R	relative influence of river to tidal inflows [-]
P	tidal prism [m^3]
T	tidal period [hr]
V_R	volume of water fluxed by the river over one tidal period [m^3]
IQR	inter-quartile range

Chapter 5: Quantifying the network-scale flow partitioning, channel-island hydrological connectivity, and water residence time distribution at Wax Lake Delta

5.1 Introduction

Many of the world's rivers pass through a delta network comprising distributary channels and interdistributary islands before debouching into the receiving basins. Water, sediment, and nutrients are partitioned through this delta network, and the allocation of these constituents has important environmental effects. Water-mediated sediment delivery controls the development of the delta platform [*Edmonds et al.*, 2011a] and the flow division at bifurcations influences patterns of delta growth [*Wolinsky et al.*, 2010]. Flow division at single river bifurcations has been extensively studied [*Bolla Pittaluga et al.*, 2003; *Bertoldi and Tubino*, 2007; *Hardy et al.*, 2011], but the influences of network structure and hydrological connectivity with off-channel areas on network-scale flow partitioning has received less attention. The partitioning of water through a delta network has a control on the water residence time distribution (RTD), and the allocation of water to deltaic islands can significantly increase water travel times [*Hiatt and Passalacqua*, 2015]. The partitioning of water to deltaic islands is important for the nutrient removal capacity of delta networks (Chapter 4), since wetlands in deltaic islands can act as nutrient sinks [*Luu et al.*, 2012; *Henry and Twilley*, 2014]. The RTD is an important parameter for estimating nutrient removal [*Nixon et al.*, 1996; *Dettmann*, 2001; *Yu et al.*, 2006], but estimates of the network-scale RTD in coastal systems

are lacking [*Rivera-Monroy et al.*, 2010]. This chapter analyzes the network-scale flow partitioning and the RTD at Wax Lake Delta (WLD) in coastal Louisiana and addresses the role of tides in flow partitioning within a river-dominated delta.

Tides influence the partitioning of water and sediment at tidal junctions [*Buschman et al.*, 2010, 2013; *Sassi et al.*, 2013] and mouth bar formation in distributary channels [*Leonardi et al.*, 2013]. The effects of tides and channel geometries at an idealized channel junction were investigated by *Buschman et al.* [2010] using numerical modeling. They found that tides enhance the unequal flow division relative to a river-only model run, except for situations in which the hydraulic roughness between the channels differs. *Buschman et al.* [2010] found that neap tide discharges were higher than those near spring tide, indicating that water was stored within their idealized junction during the spring tide. We test the effect of the spring-neap tidal cycle in this chapter using field measurements and hydrodynamic modeling at WLD.

5.2 Field Measurements

Two field trips aimed at quantifying the partitioning of flow through the WLD distributary network with acoustic Doppler current profiler (ADCP) measurements. These field trips were designed to capture the flow partitioning at the network scale and to test the influence of tides (flood and ebb tides, spring and neap tides). During each trip, we measured flow within the major distributary channels at WLD (Figure 5.1).

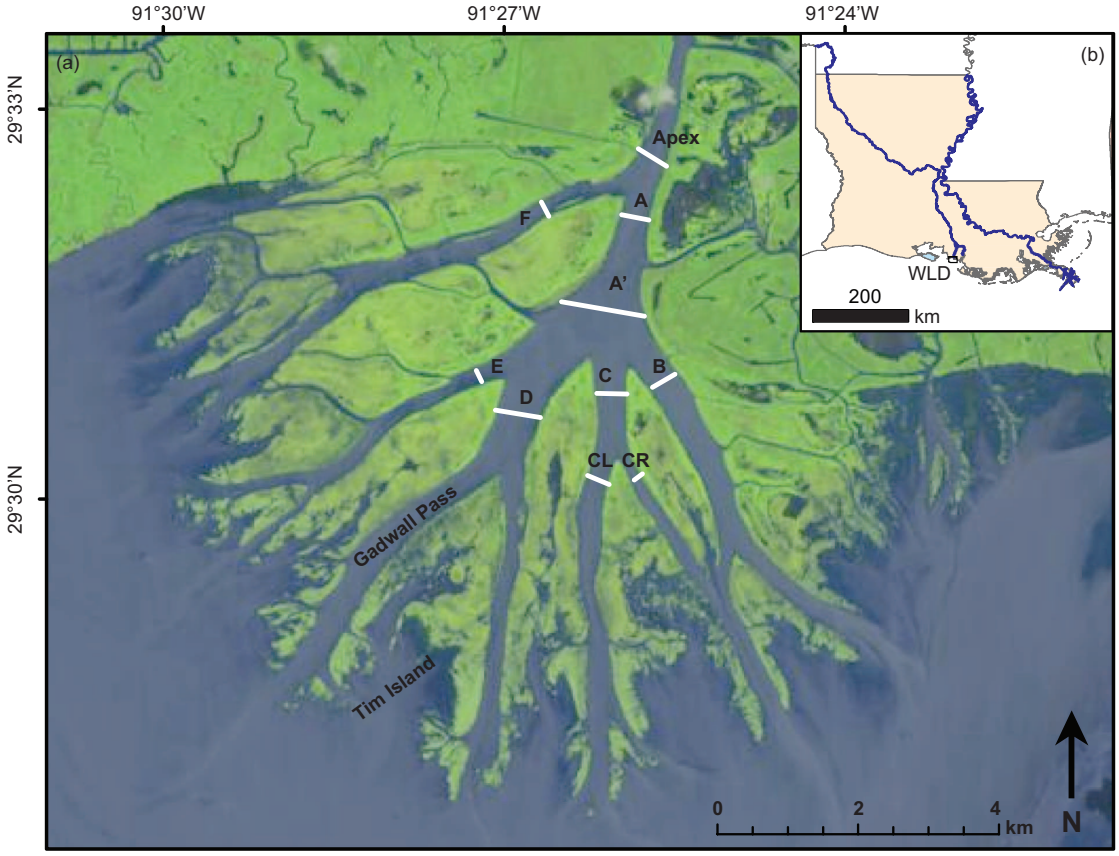

Figure 5.1: Map of the locations of ADCP transects for the February 2013 and June 2014 field trips. Image specifications: LANDSAT 8 image from 19 June 2014 at 30-m resolution. (b) Map of Louisiana and the major rivers flowing into the Atchafalaya Bay. The WLO debouches into the Atchafalaya Bay at WLD and receives its flow from the Atchafalaya River.

5.2.1 Acoustic Doppler current profiler measurements

Discharge was measured by traversing transects in the major WLD distributary channels (Figure 5.1 - Locations Apex, A, B, C, D, E, CL, and CR) with a 600 kHz Teledyne RD Instruments Workhorse Rio Grande Acoustic Doppler Current Profiler (ADCP) in conjunction with differential GPS. The ADCP was mounted to the *R/V Itasca* and sat 0.4 m below the water surface.The bin size was set to 0.50 m, the blanking distance was 0.44 m, and the boat speed was maintained at less than 1.0 m s^{-1}. The velocity transects were measured on 15 February 2013 from 08:00 to 12:00 and from 12:00 to 16:00 CDT in an attempt to capture the falling and rising tides, respectively. The measurements coincided with a steady seasonal hydrograph at the USGS gage at Calumet, LA on the WLO. Flows had been near 1000 m^3 s^{-1} for much of the winter before rising and topping 4200 m^3 s^{-1} by February 1. On February 15, the station recorded a maximum flowrate of 4530 m^3 s^{-1} and a minimum of 3850 m^3 s^{-1}. For each cross section, two consecutive passes (right bank to left bank, then left bank to right bank) at each transect location were conducted during the predicted falling and rising tides. The field trip was conducted during a neap tide with relatively high river discharge.

In June 2014, discharge was again measured in the major distributary channels at WLD (Figure 5.1a - Locations A', B, C, D, E, and F). Coinciding with predictions for the spring and neap tides, velocity transects were sailed on 15 June 2014 and 20 June 2014, respectively (Figure 5.2a). The ADCP measurement set up coincides with the methods of *Hiatt and Passalacqua* [2015]. We measured velocity profiles along the transects with the 2 MHz RDI StreamPro with the long-range upgrade measuring in water mode 12sp. Due to depth limitations associated with

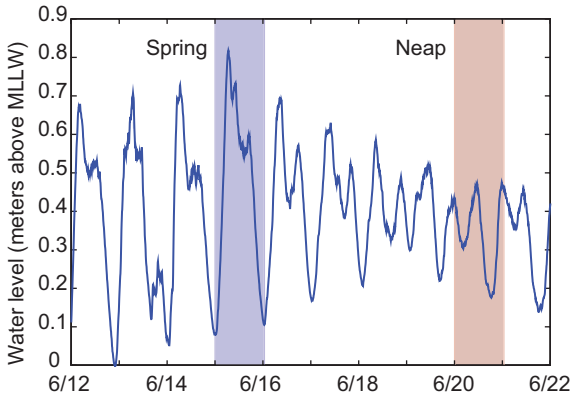

Figure 5.2: Water levels from the NOAA Lawma-Amerada Pass Station [*NOAA*, 2016] during the June 2014 field trip. The spring tide ADCP measurements took place on 15 June and the neap tide measurements took place on 20 June.

the ADCP, transects Apex and A could not be measured since they were greater than seven meters in depth. The ADCP was floated alongside the bow of the *R/V Bluerunner* and the transect was traversed four times at an average boat speed of about 1.0 m s^{-1}. The data output rate was maintained at 1 Hz and each collected velocity ping was averaged from eight subpings. The ADCP transducer was 0.15–0.20 m below the water surface, depending on channel depth and surface roughness conditions. The blanking distance was 0.27 m. Depth profiles were linearly extrapolated to the channel banks at a distance estimated from satellite imagery. ADCP transects were collected during both rising and falling tides. The flow entering the WLD at transect A was 2880 m^3 s^{-1} during falling tide on 06/20 and the average from the Calumet gage was about 3450 m^3 s^{-1} [*USGS*, 2016]. To calculate discharge for both field trips, the measured velocities were projected onto the average flow direction for each transect. Teledyne RDI's WinRiver II software was used to process the GPS and ADCP data and output water discharge within each cross section.

5.3 Numerical Modeling Approach

5.3.1 Model domain and setup

The Fine Resolution Environmental Hydrodynamics model (Frehd) was used to quantify the flow partitioning through WLD network under river and tidal forcing. For the present purposes, Frehd solves the depth-averaged hydrostatic Navier-Stokes equations with the Boussinesq approximation (i.e. the shallow water equations). The transport of a diffusive tracer is modeled using Frehd to quantify the network-scale RTD. The governing equations used in this study are presented in Section 4.3. The bottom drag coefficient, C_B, was set to a uniform value of 0.005 throughout the computational domain, which corresponds to a typical value of bed roughness for similar applications [e.g., *Buschman et al.*, 2010]. The horizontal eddy viscosity was set to a constant 0.01 $m^2\ s^{-1}$.

The computational domain is derived from bathymetric and topographic data collected at WLD [*Shaw et al.*, Airborne Radar Imaging of Subaqueous Channel Evolution in Wax Lake Delta, Louisiana, USA, *in review Geophysical Research Letters*, 2016]. The test domain is 15×22.5-km Cartesian grid comprising 2×10^5 cells with 50 m spacing in both the x_1 and x_2 directions (Figure 5.3). The test domain is nested within a larger computational domain to buffer the effects of artificial boundary conditions. Comprising the buffer domain is a 10-km extended bay downstream of the test domain and a 500-m wide, 100-km long channel extending upstream that ensures the proper attenuation of tides. The lateral buffer of 5 km on either x_2 side of the delta bathymetry ensured a smooth transition to zero velocity in the x_2-direction for all runs. The bay is set to an elevation of $z = -2$ m and the transition from the collected bathymetry and the artificial bay

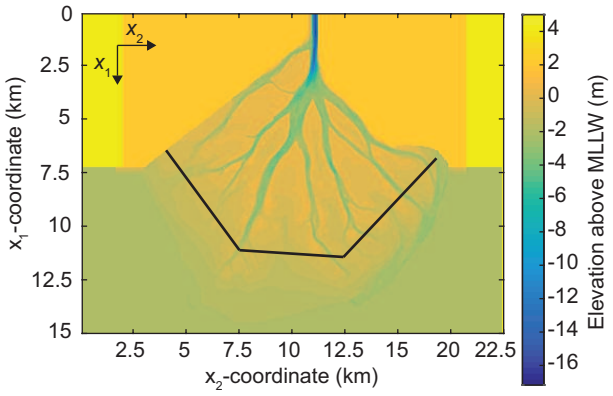

Figure 5.3: The test domain for the numerical model. The grid size is 50 m and the bathymetry was rotated 16.5° to orient the feeder channel perpendicular to the -x_1 boundary. The cell elevation is depicted by the color map. Lines are drawn to delineate the transect at which the network-scale RTD is calculated.

depth was smoothed with a Gaussian filter in Matlab. The time step of 25 s was selected to ensure numerical stability.

5.3.2 Model runs and analyses

We subjected the model to a constant river discharge of $Q_R = 3300$ m^3 s^{-1} at the $-x_1$ boundary and forced the model with a spring-neap tidal cycle at the $+x_1$ boundary. The discharge was chosen as a representative value based on our ADCP measurements for discharge entering WLD on 20 June 2015. The spring-neap tidal cycle was generated as

$$\eta(t) = \sum_{n=1}^{n=N} A_n cos(\sigma_n t - G_n) \tag{5.1}$$

where A_n is the tidal amplitude [m], σ_n is the angular speed [rad hr^{-1}], G_n is the phase lag [rad], t is time [hr], and N is the number of tidal constituents. The S2 (principal solar semidiurnal) and M2 (principal lunar semidiurnal) tidal

constituents from the Lawma-Amerada Pass Station (Figure 3.1b) are used (A_{S2} = 0.10 m and A_{M2} = 0.29 m, respectively), which results in a spring-neap tidal cycle typical of the WLD (Figure 5.4).

Two model runs were performed. The first model run is subject to the contributions from the river only and the tidal boundary condition is turned off. The water level is maintained at a constant η = 0.41 m, which was selected because it was the average water level during the June 2014 ADCP measurements. The second model run included the forcing from both the river and the tides. The river-only simulation was allowed to run for 2.6 days of modeled time before reaching steady-state. The spring-neap simulation ran for 2.6 days of river-only forcing before the spring-neap cycle began. We allowed the model to reach a dynamic steady state (7.86 days of modeled time) subject to the spring-neap boundary condition before beginning analysis on transition from spring to neap tide (Figure 5.4). A summary of the default model parameters is presented in Table 5.1.

Table 5.1: Hydrodynamic model parameters

Symbol	Variable	Value
Δx	along-channel grid size	50 meters
Δy	cross-channel grid size	50 meters
Δt	time step	25 seconds
C_D	bottom drag coefficient	0.005
Q_R	river discharge	3300 m^3 s^{-1}
ν_T	Eddy viscosity	0.01 m^2 s^{-1}
A_{S2}	Amplitude of S_2	0.10 m
A_{M2}	Amplitude of M_2	0.29 m

The discharge (Q) for a given transect was calculated by numerically integrating over the grid cells spanning the transect of interest. The velocity ($V = \sqrt{{u_1}^2 + {u_2}^2}$) was projected perpendicular to the transect and multiplied by the

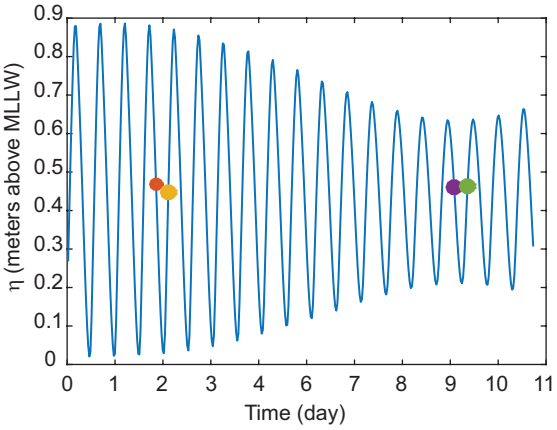

Figure 5.4: The idealized tidal boundary condition imposed at the $+x_1$ boundary in the model (Figure 5.3). The M_2 and S_2 tidal constituents used to generate the tidal predictions at Lawma-Amerada Pass [*NOAA*, 2016] were used to generate the synthetic tidal signal. The circles on the tidal time series denote the timing of measurements associated with the SF (orange), SR (yellow), NF (purple), and NR (green).

distance between cell centers and the local depth to obtain Q. The normalized discharge ($\hat{Q}$) is for a given transect is defined as the local discharge divided by the discharge input at the $-x_1$ boundary (i.e., $\hat{Q} = Q/Q_R$). We calculated Q, $\hat{Q}$, V, and water surface elevation (η) profiles to quantify the flow partitioning at the network scale, which includes the flow through distributary channels and interdistributary islands. The division of flow at a bifurcation is presented as an index of the relative allocation of flow between two channels. The discharge asymmetry index (Ψ) is calculated as:

$$\Psi = \frac{Q_1 - Q_2}{Q_1 + Q_2} \tag{5.2}$$

where Q_1 and Q_2 are the discharges in two channels splitting from the bifurcation [*Buschman et al.*, 2010]. We take the absolute value of Ψ for comparison among the channels at WLD. The dominant flow direction and the magnitude of Ψ were

compared with the field data for rising and falling tides during both the spring and neap tidal regimes.

To quantify the network-scale RTD, we calculated the probability density function (PDF) of a tracer passing through a transect bounding the system at the delta front (Figure 5.3) for the river-only model run. The tracer was released in a uniform concentration ($c_t = 1$ [mass/volume]) along 10 grid cells comprising the perpendicular transect of the feeder channel upstream of the delta apex (i.e., $x_1 = 0km$ in Figure 5.3) and its propagation was monitored. The PDF for this pulse input condition was calculated as:

$$PDF(\tau) = \frac{Q}{M_{in}} c_t(\tau) \tag{5.3}$$

where M_{in} is the initial mass of the scalar and $c_t(\tau)$ is the local tracer concentration at a given residence time τ. The PDF was calculated at the delta front transects until $< 1\%$ of the tracer by mass remained in the test domain. The marginal PDF for any given transect within the test domain can be calculated equivalently to Eq. 5.3 given that M_{in} equals the initial mass of the scalar for the entire test domain. We calculated marginal PDFs throughout the domain to quantify the spatial variability in RTD in the WLD network. The definite integral:

$$F = \int_{\tau=0}^{\tau=\infty} PDF \; d\tau \tag{5.4}$$

gives the area under the PDF, which is equivalent to the fractional mass of the tracer passing through a transect. The parameter F [-] is used to quantify the influence of channel-island hydrological connectivity on the spatial variability of

the marginal PDFs throughout the WLD network.

5.4 Results and Discussion

5.4.1 Network-scale flow partitioning

The results of the ADCP measurements from 15 February 2013, 15 June 2014, and 20 June 2014 are summarized in Table 5.2. Hereinafter, unless otherwise indicated, the average discharge is reported for each transect. In general, the discharge values did not vary significantly among the repeat transects (Table 5.2), so the average discharge is considered an adequate representation of the discharge through the transect.

The 15 February 2013 field trip comprised measurements at locations Apex, A, B, C, D, E, CR, and CL during the falling and rising tides, according to the tidal gage at the nearby Lawma-Amerada Pass Station (see Figure 3.1b for location). For both the rising and falling tides, the flow direction pointed toward the bay (i.e., downstream). In general, good agreement existed between the discharge at Transect A and the sum of discharges at transects B, C, D, and E. The discharge at transect A during falling tide was 3278 m^3 s^{-1}, and the sum of the discharges at transect B, C, D, and E was 3344 m^3 s^{-1}, which computes to a ratio of 1.02 for downstream and upstream discharges. During rising tide, the ratio was also 1.02. A similar behavior existed at transect C and its downstream bifurcates, CR and CL. The ratio of agreement between the downstream discharge sum and the upstream discharge was 1.05 during rising tide and 1.00 during falling tide.

The influence of the daily tidal cycle on the discharge partitioning through the distributary channels was also analyzed. Let the ratio of falling tide discharge

Table 5.2: Average discharge, area, and width measured by the ADCP on 15 February 2013 and 15 and 20 June 2014. Transects averaged over fewer than four repeat measurements are italicized for the June 2014 field trip.

Time and Date	Location	Tide	Q (m^3 s^{-1})	Area (m^2)	Width (m)
08:02 15 Feb	Apex	Fall	3734 (26)	3951 (49)	437 (61)
08:23 15 Feb	A	Fall	3278 (14)	3696 (11)	396 (1)
08:47 15 Feb	E	Fall	588 (4)	935 (5)	289 (3)
09:08 15 Feb	D	Fall	1279 (7)	2209 (11)	682 (4)
09:46 15 Feb	C	Fall	796 (12)	1244 (7)	428 (2)
10:13 15 Feb	B	Fall	681 (5)	1189 (20)	493 (7)
10:39 15 Feb	CR	Fall	221 (25)	397 (30)	160 (15)
10:54 15 Feb	CL	Fall	572 (1)	940 (23)	309 (6)
12:31 15 Feb	CL	Rise	582 (3)	950 (5)	309 (4)
12:49 15 Feb	CR	Rise	228 (14)	420 (31)	176 (17)
13:38 15 Feb	B	Rise	683 (18)	1248 (1)	523 (4)
13:59 15 Feb	C	Rise	775 (5)	1275 (14)	439 (3)
14:26 15 Feb	D	Rise	1250 (5)	2254 (2)	682 (4)
14:53 15 Feb	E	Rise	580 (3)	926 (1)	285 (3)
15:19 15 Feb	A	Rise	3225 (33)	3755 (18)	411 (19)
15:41 15 Feb	Apex	Rise	3671 (38)	3851 (12)	378 (9)
08:45 15 Jun	B	Fall	*430* (5)	*1266* (91)	*490* (16)
09:18 15 Jun	C	Fall	466 (24)	1309 (128)	455 (42)
10:22 15 Jun	F	Fall	247 (26)	868 (26)	301 (14)
10:59 15 Jun	E	Fall	447 (10)	913 (18)	310 (8)
11:38 15 Jun	D	Fall	*914* (5)	*2230* (147)	*668* (36)
13:16 15 Jun	B	Lower-high	468 (8)	1153 (58)	466 (18)
14:02 15 Jun	C	Lower-high	*625* (18)	*1217* (28)	*423* (8)
14:58 15 Jun	D	Lower-high	880 (74)	2095 (32)	653 (17)
16:06 15 Jun	E	Lower-high	418 (18)	888 (33)	309 (8)
16:53 15 Jun	F	Lower-high	317 (22)	804 (14)	293 (3)
08:52 20 Jun	D	Rise	971 (10)	2161 (27)	640 (6)
09:50 20 Jun	E	Rise	448 (7)	870 (29)	314 (28)
10:29 20 Jun	C	Rise	610 (3)	1274 (18)	465 (9)
11:13 20 Jun	B	High	537 (6)	1198 (22)	501 (7)
12:43 20 Jun	F	Fall	364 (4)	802 (17)	306 (3)
13:25 20 Jun	D	Fall	1118 (14)	2208 (33)	699 (20)
14:11 20 Jun	E	Fall	530 (9)	867 (12)	324 (7)
14:40 20 Jun	A'	Fall	*2899* (10)	*4359* (214)	*928* (8)
15:32 20 Jun	C	Fall	716 (10)	1195 (15)	449 (9)
16:32 20 Jun	B	Fall	619 (9)	1122 (20)	502 (6)
17:11 20 Jun	F	Fall	381 (9)	728 (20)	296 (6)

($Q_{falling}$) to rising tide discharge (Q_{rising}) at transect i be defined as:

$$\phi_i = \frac{Q_{falling,i}}{Q_{rising,i}}. \tag{5.5}$$

For the 15 February 2013 measurements, ϕ_i ranged from 0.97 to 1.03, suggesting that the daily tidal fluctuations had little effect on the magnitude of measured discharge for the February 2013 measurements.

Discharges at transects A', B, C, D, E, and F were measured on 15 June and 20 June 2014 to examine the influence of the spring and neap tidal cycle on the network-scale flow partitioning (Figure 5.5). The velocity transects were designed to take place during both the falling and rising tides based on tidal predictions [*NOAA*, 2016], but the 15 June measurements for rising tide actually took place during a lower-high tide. Water levels did not significantly rise as predicted, which may be due to the wind. During the 20 June 2014 measurements, both rising and falling tide were captured at each transect. Comparing the differences in discharges between spring and neap tide reveals that discharges are generally larger during neap tide than during spring tide for both rising and falling tides (Table 5.2 & Figure 5.5). Averaging over the daily tides, the discharges entering the five major bifurcates were 2606 and 3122 $m^3\ s^{-1}$ for spring and neap tide, respectively. However, the discharge at the Calumet station did increase from 3144 to 3454 $m^3\ s^{-1}$ from 15 to 20 June 2014. The daily average river discharge at Calumet increased 310 $m^3\ s^{-1}$ while the discharge within WLD increased 516 $m^3\ s^{-1}$. This may suggest some storage of the tidal prism may be occurring on the WLD during spring tide and then subsequently released during neap tide as was found by *Buschman et al.* [2010] for a macro-tidal system. However, the discharge measurements at

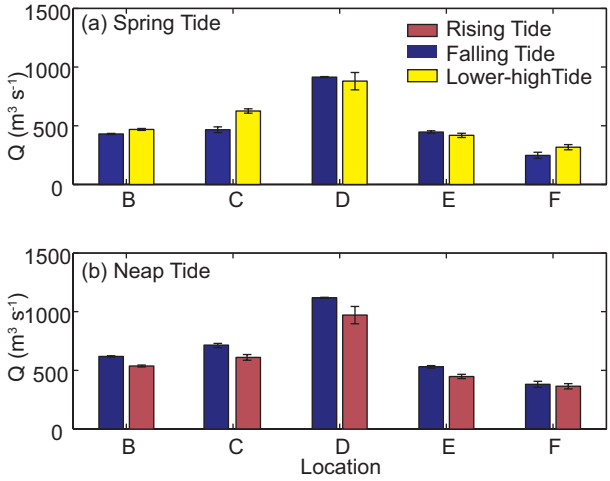

Figure 5.5: Discharge values for the (a) spring and (b) neap tides at WLD during June 2014. Error bars indicate the standard deviation of the measurements. Note that the location B for Spring-Rising tide was measured during a high tide, but is included with the rising tide for simplicity.

Calumet ranged over 700 m^3 s^{-1} on 06/15 so it is difficult to determine whether the spring-neap tidal cycle did indeed have a significant effect on the distributary channel discharge.

Winds were gusting from the south at speeds > 5 m s^{-1} for the duration of the measurements on 15 June 2014, which can cause a significant water level setup [*Geleynse et al.*, 2015] that may have lowered flow velocities within the channels. The high winds on 15 June also generated significant surface waves that proved problematic for floating the ADCP alongside the boat and led to relatively low precision for the average discharge measurements (Table 5.2). These waves likely decreased the accuracy of the measured discharges.

The discharges measured in the field are normalized for comparison with the modeled discharges. The normalized transect discharge ($\hat{Q}$) is obtained by dividing the transect discharge Q by the discharge entering WLD through the

Apex transect. Since, the Apex discharge was not measured during the June 2014 field trip, the sum of discharges passing through B, C, D, E, and F was used for normalization. This assumption is reasonable considering the good agreement obtained among the measurements at A', B, C, D, and E on 20 June (ratio = 1.03). The modeled flow partitioning is compared to the field discharge results in Figure 5.6 for the river-only and tidal cases during spring and neap tide.

In general, $\hat{Q}$ does not significantly vary for each transect across the model results and field observations. The average variability among the measurements at each transect is 5% and the maximum variability occurs at transects A and D (8%). Transect D consistently receives the largest allocation of flow among the major bifurcates downstream of the Apex and transect A. Transect C received about 25% of the total flow through the system followed by B, E, and F. A large flow asymmetry exists at the CR-CL bifurcation, with CL receiving the majority of flow from transect C. The area of the cross sectional area of the channel controls the allocation of flow (Table 5.2), which agrees well with the control of depth on bifurcation flow asymmetry [*Buschman et al.*, 2010; *Kleinhans et al.*, 2013].

The flow asymmetry index (Ψ) gives the relative partitioning of flow through the two channels downstream of a bifurcation. We tested the influence of tides on Ψ for the major bifurcations at WLD and found that neither the spring-neap or semidiurnal tidal cycle has an influence on the flow asymmetry (Figure 5.7). Width and channel cross-sectional area seem to be the major controls on Ψ. The tidal fluctuations due to the semidurnal component do modulate the flow asymmetry at a bifurcation, but never more than 10% for both the modeled and field results. The modeled results compare reasonably well with the results from the field and correctly capture the dominant channel in all cases, but the magnitudes of Ψ differ

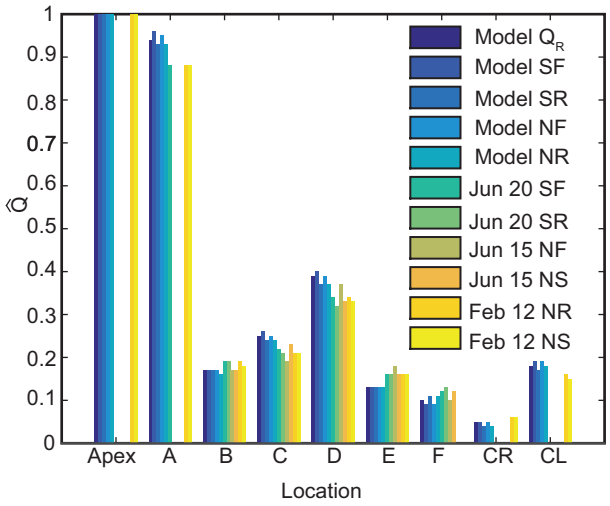

Figure 5.6: Summary of the model and measured flow partitioning in the major distributary channels at WLD. The bar labels are interpreted as follows: 'Model' indicates a model run and the date denotes the date of field measurements; 'Q_R' stands for river-only forcing; 'S' is spring tide; 'N' is neap tide; 'F' is falling tide; 'R' is rising tide. Modeled results for SF, SR, NF, and NR correspond to the times denoted in Figure 5.4. Error bars are omitted from the plot because they are generally on the order of 1%. Gaps in the data are present for locations Apex, A, CR, and CL because they were not measured during the June 2014 field trip. Location F was not measured during the February 2013 field trip.

between the modeling and field results. On average, the flow asymmetry at A'-F is captured very well, with a modeled average of $\Psi = 0.8$ and a field value of $\Psi = 0.77$ for falling tide. The model over-predicts Ψ at C-B and D-E, but under-predicts at L-G. This discrepancy may be due to limitations of the model bathymetry or environmental forces like wind that are not accounted for in the model.

5.4.2 Channel-island hydrological connectivity

The network-scale channel-island hydrological connectivity was quantified with the river-only model run and the dynamics of hydrological connectivity through a

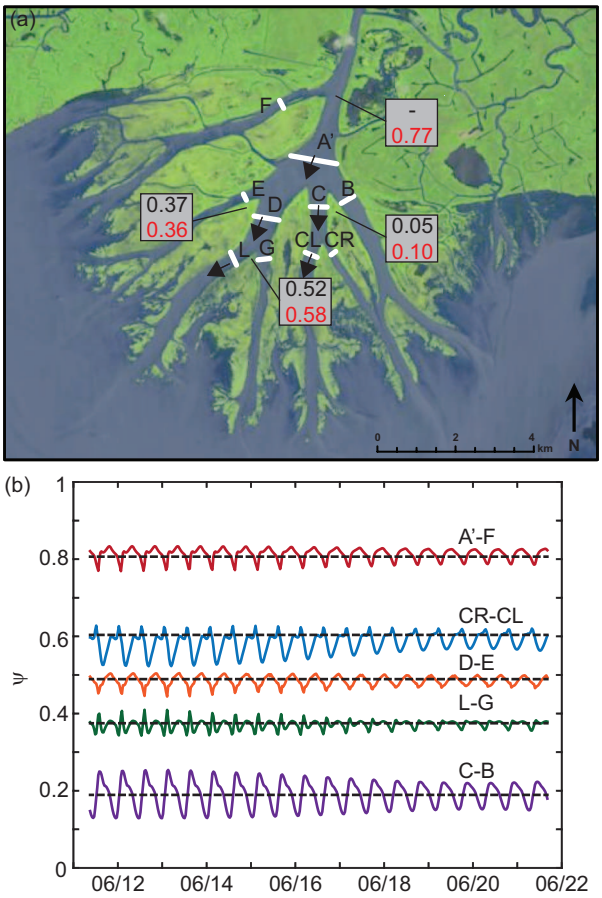

Figure 5.7: Summary of the modeled and measured discharge asymmetry index in the WLD channel network. (a) The discharge asymmetry index (Ψ) for the 20 June 2014 discharge measurements at WLD (the absolute value of Ψ is presented for comparison). The black values represent rising tide and the red values indicate falling tide. The dominant channel is delineated with an arrow. Field values at transect L-G are from the 19 June 2014 measurements conducted by *Hiatt and Passalacqua* [2015] (Chapter 3). (b) The modeled absolute value of Ψ for the bifurcations in (a). The dashed line represents Ψ due to river discharge only and the solid lines represent ψ subject to the tidal forcing in Figure 5.2b.

secondary channel was studied in detail for the tidal run. Nearly 55% of the water flux at the apex departed the channels and entered the islands (Figure 5.8). Nearly the delta front, Tim Island fluxed the most water (12.8%) of any element of the

WLD network. The limited control of tides on flow partitioning and the significant hydrological connectivity suggest that network-scale flow partitioning (including flow into the islands) at the WLD is controlled primarily by the geometry of the system. Indeed, the estimate of 55% of the flow entering the interdistributary islands estimated by this study is in agreement with the 59% flow departure from the WLD distributary channels estimated from topography by *Shaw et al.* [2016].

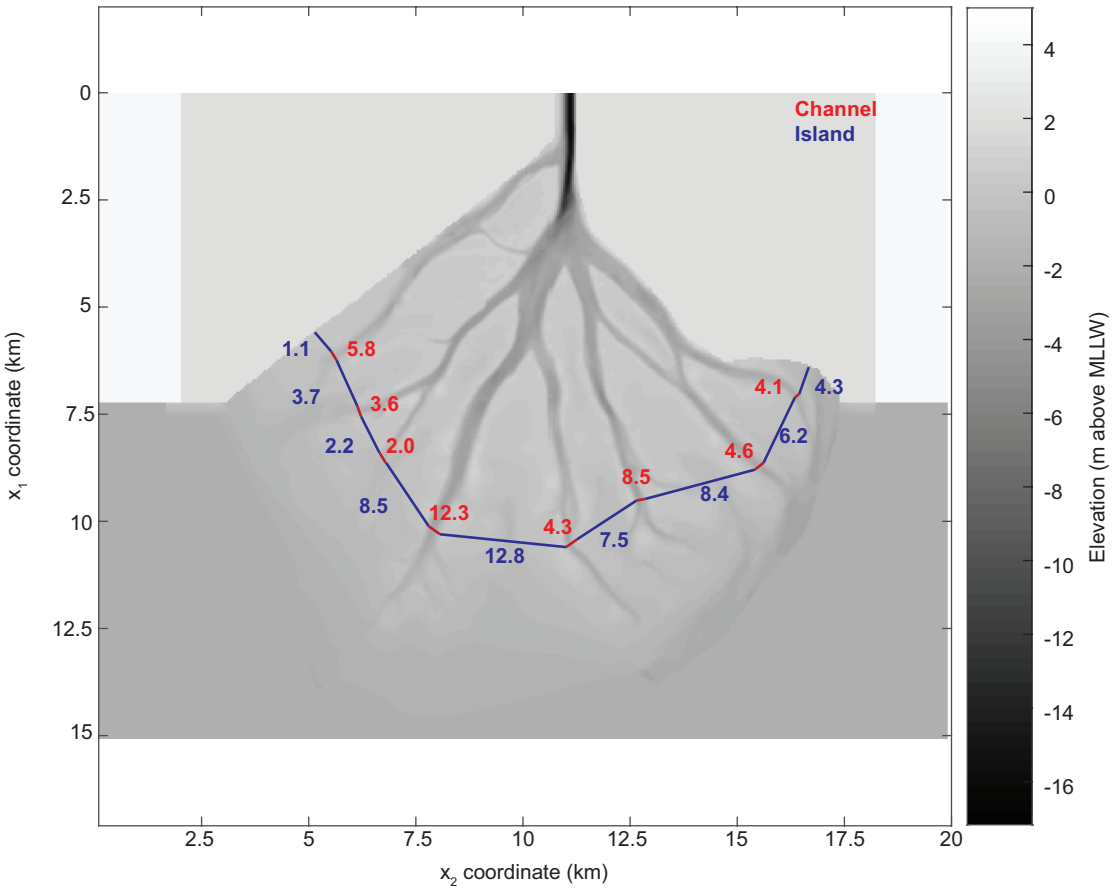

Figure 5.8: Network-scale distribution of $\hat{Q}\times 100\%$ at WLD for the river-only model run.

The influence of tides on the flow into an interdistributary island for a secondary channel on Tim Island (Figure 5.9a) was studied in detail with the

model. The following results are presented for spring tide, but the same behavior existed for neap tide. Water surface profiles along the longitudinal axis of the island revealed that the water surface gradient between the channel and the island was modulated by the tides (Figure 5.9b), which influenced flow velocities through the secondary channel and within the island (Figure 5.9c–f). The difference between the channel η and the island η along the transect was highest during the low tide (0.22 m), which led to a water surface slope of 5×10^{-4}. Falling tide led to a differential water level set up of 0.03 m and a water surface slope of 6×10^{-5}. The water surface slopes during rising and high tide were 1×10^{-5} and 8×10^{-6}, respectively. Although only four instances of time are presented here, water surface slope between the channel and the island steadily increases as water levels lower towards low tide, where the slope reaches a maximum. As the water level increased during rising tide, the water surface slope approached zero and reaches a minimum at high tide.

The water surface slope between the channel and the island acted to modulate the flow velocity through the secondary channel (Figure 5.9c–f). The velocities during falling tide were generally downstream and water departed the distributary channel through the secondary channels and overbank flow (Figure 5.9c). During the low tide, flow was localized within the secondary channel and velocities were relatively high (Figure 5.9d), and overbank flow was limited due to the low water levels. Rising tide tends to alter flow directions and initiates propagation of water entering the island through the secondary channel towards the upstream portion of the island. During high tide, flow velocity magnitudes are relatively uniform throughout the secondary channel, interdistributary island, and distributary channel (Figure 5.9f). For all cases, flow consistently entered the island through

the secondary channel. The localization of flow and increased velocities in the secondary channel during low tide point toward the tidal modulation of erosion within secondary channels. Distributary channels at WLD are erosional [*Shaw et al.*, 2013; *Shaw and Mohrig*, 2014], so it follows that secondary channels may mine island deposits and extend into the island interior. Further work is needed to quantify the tidal modulation of shear stress to determine erosive/depositional thresholds.

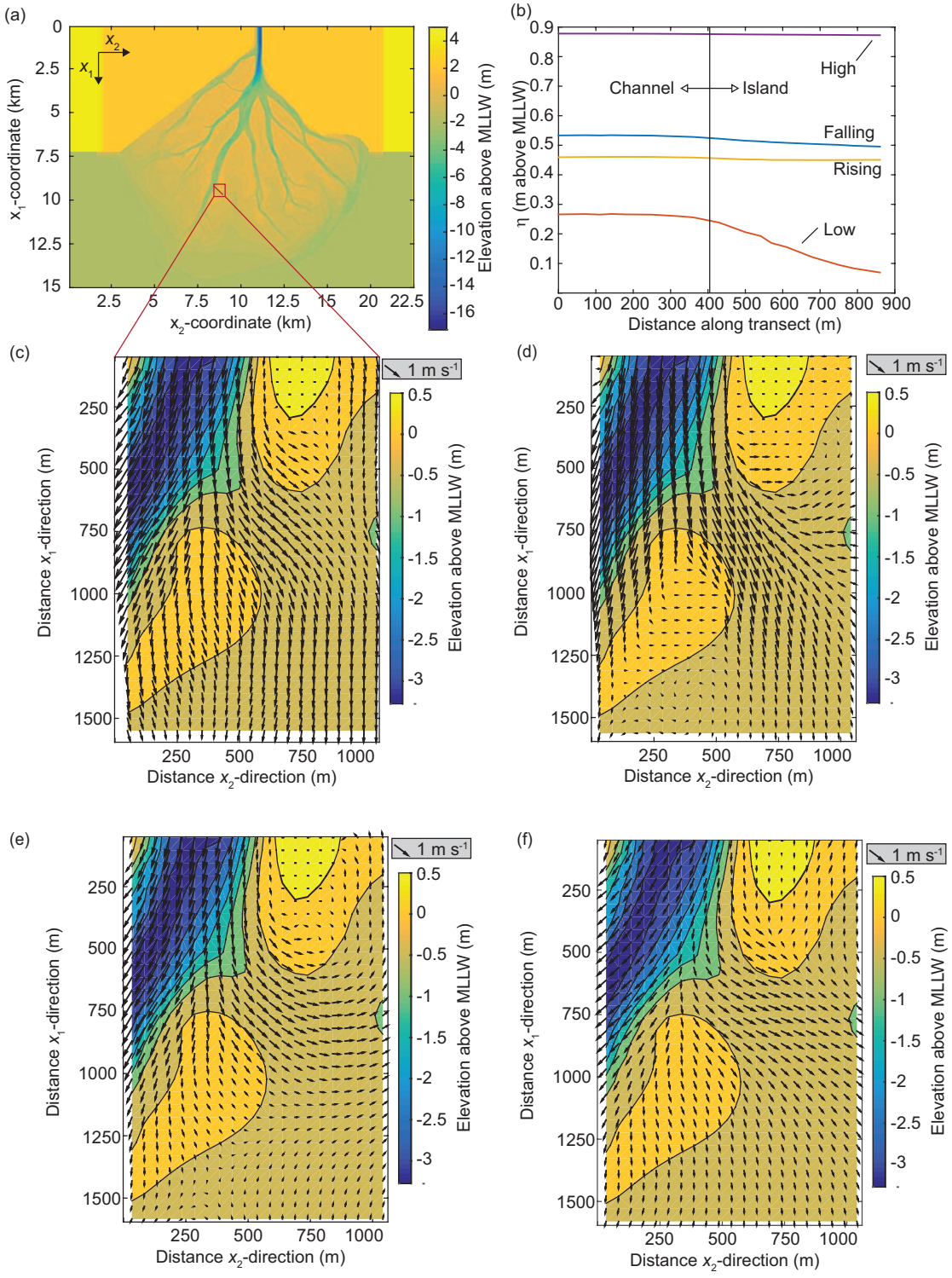

Figure 5.9: Tidal modulation of channel-island water surface gradients and flow velocities. (a) Transect location within Tim Island and the adjacent Gadwall Pass.

Figure 5.9 (cont.): (b) Water surface profiles along the transect in (a). Maps of velocity magnitude ($V = \sqrt{{u_1}^2 + {u_2}^2}$) for (c) falling tide, (d), low tide, (e) rising tide, and (f) high tide. The results for spring tide are shown, but neap tide exhibits a similar behavior.

As water moved down the distributary channels at WLD, the magnitude of velocity (V) generally tended to decrease (Figure 5.10). The pattern and magnitude V was relatively consistent among the distributary channels. For example, η generally decreased with distance downstream along Gadwall Pass (Figure 5.11a), leading to a water surface slope of -2.3×10^{-5} (Figure 5.11b). Additionally, the centerline velocity (V_{center}) generally decreases with distance downstream. However, from about 5 km to 10 km, V_{center} remained relatively constant around 0.6 m s^{-1}, but fluctuations did exist (Figure 5.11c). These fluctuations were likely

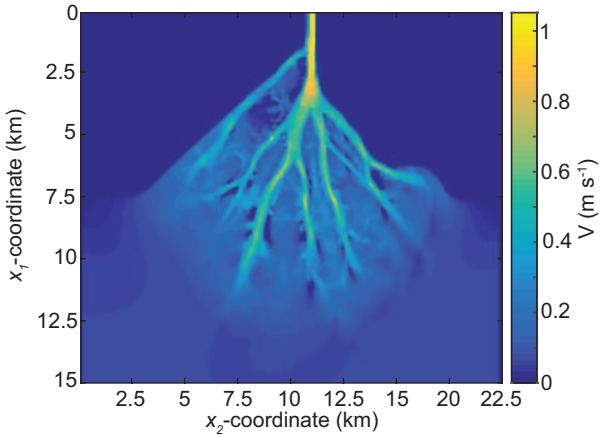

Figure 5.10: The map of velocity magnitude ($V = \sqrt{{u_1}^2 + {u_2}^2}$) for the river-only case.

due to spatial variability in the geometry of the channel. The spatial deceleration in velocity is due to the lateral spreading of flow over the channel margins and through secondary channels [*Hiatt and Passalacqua*, 2015], which can cause depo-

sition of sediment in the interdistributary islands [*Shaw et al.*, 2016]. The lowest values of V tended to be near the island margins and velocities increase toward the center of the islands. The presence of an 'interdistributary trough'—relatively low elevation zone along the longitudinal axis of the island—that acted as a conduit that facilitated a velocity increase within the island interior [*Shaw et al.*, 2016].

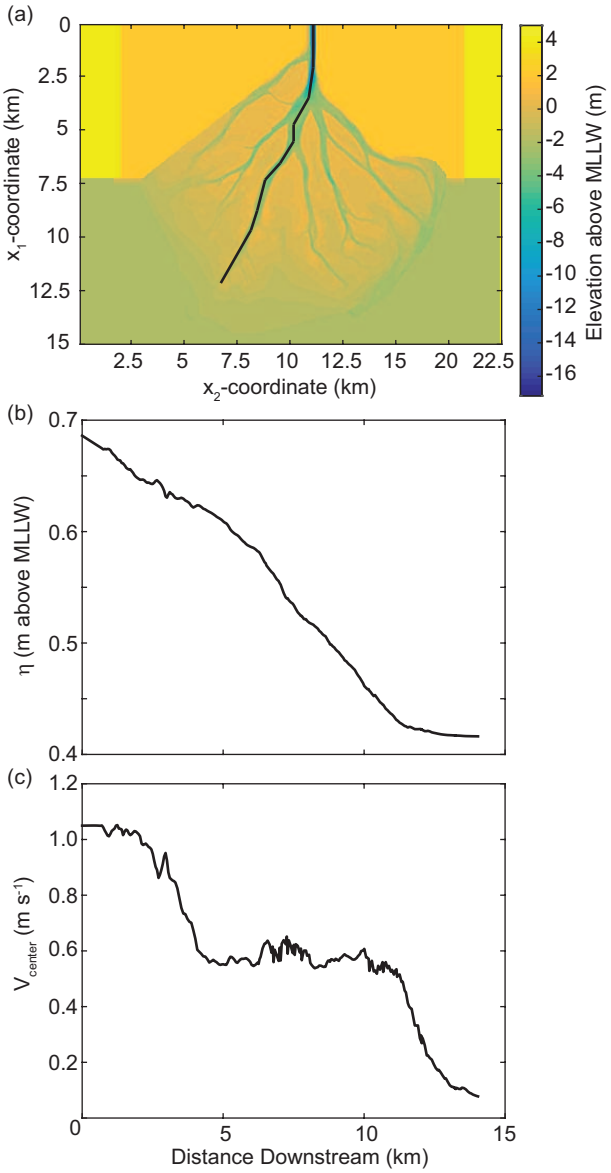

Figure 5.11: The modeled hydraulics within Gadwall Pass for the river-only model run. (a) Map of the transects used along which η and V_{center} are calculated. (b) The water surface elevation within Gadwall Pass. The slope of the water surface is roughly 2.3×10^{-5} up to $\sim$11 km, before approaching the bay water level ($\eta = 0.41$ m above MLLW). The water surface profile is concave down, which is in accordance with the adverse bed slope. (c) The centerline velocity magnitude (V) along Gadwall Pass. The centerline velocity magnitude rapidly decreases after the initial bifurcation at WLD and again as near the delta front.

5.4.3 Network-scale water residence time distribution

To quantify the RTD at the network scale, we tracked the propagation of a diffuse numerical tracer in the Frehd model for the river-only and tidal scenarios and calculated the PDF at a boundary near the delta front (see boundary in Figure 5.3). The PDF was generated for the river-only, spring tide, and neap tide cases (Figure 5.12). The median residence time was 8.9 hours and the RTD IQR was 2.5 hrs for the river-only case. This estimate of the RTD represents a benchmark for estimating the RTD at WLD under a suite of environmental forces.

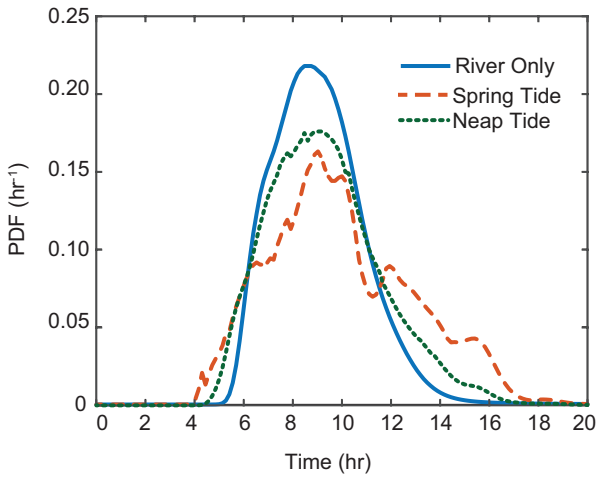

Figure 5.12: PDFs of RTDs for the river-only, spring-, and neap-tide cases for the boundary in Figure 5.3. The spring and neap tide cases are each an average of the PDFs for falling, rising, high, and low tide tracer releases.

The river-only case had the most peaked RTD of the three tested cases (Figure 5.12). Accordingly, the tail of the river-only distribution is the shortest, indicating that the introduction of tides increase the prevalence of extreme values in the RTD. In general, tides acted to increase the dispersion of the RTD (Figure 5.12). The median water residence time for the spring tide case was 9.5 hrs

and the IQR was 4.1 hrs. For the neap tide case, the median was 9.0 hrs and the IQR was 3.1 hrs. The spring tide IQR is larger than that of the neap tide model run because the tidal amplitude is larger during spring tide, which causes a more flow reversal than that associated with a smaller tidal amplitude. Interestingly, tides also decreased the minimum residence times observed (Figure 5.12). Water residence times were increased by tides due to the increased basinward discharge and velocities associated with ebb tide.

Marginal RTDs were calculated for various transects along Gadwall Pass and Tim Island to examine the influence of hydrological connectivity on local RTD (Figure 5.13). In Gadwall Pass, the marginal RTDs are very narrow and highly-peaked (Figure 5.13a,b). The shape of the RTD is as such because the channel is likely advection-dominated due to its relatively high streamwise velocities. All of the tracer that passed through Gadwall Pass exited transect 5 in less than 6 hrs, which is substantially shorter than the median water residence time for the entire WLD network (8.9 hrs). At transect 1, $F = 0.27$, which indicates that 27% of the initial tracer mass passed through transect 1. As the tracer moved downstream, the F value decreased to 0.10 at transect 5 (Figure 5.13b). This decrease means that 63% of the flow that entered Gadwall Pass through transect 1 did not exit Gadwall Pass at transect 5 and likely entered the islands flanking the channel. It is important to note that the measurements of *Hiatt and Passalacqua* [2015] did not extend to the subaqueous channel tips, and thus their estimates of flow reduction are expected to be lower than those calculated here.

Converse to the behavior of the RTD in Gadwall Pass is that of the adjacent Tim Island (Figure 5.13c,d). There was very little flow allocated to the more landward portion of Tim Island ($F = 0.004$ at transect 1). However, the mass of

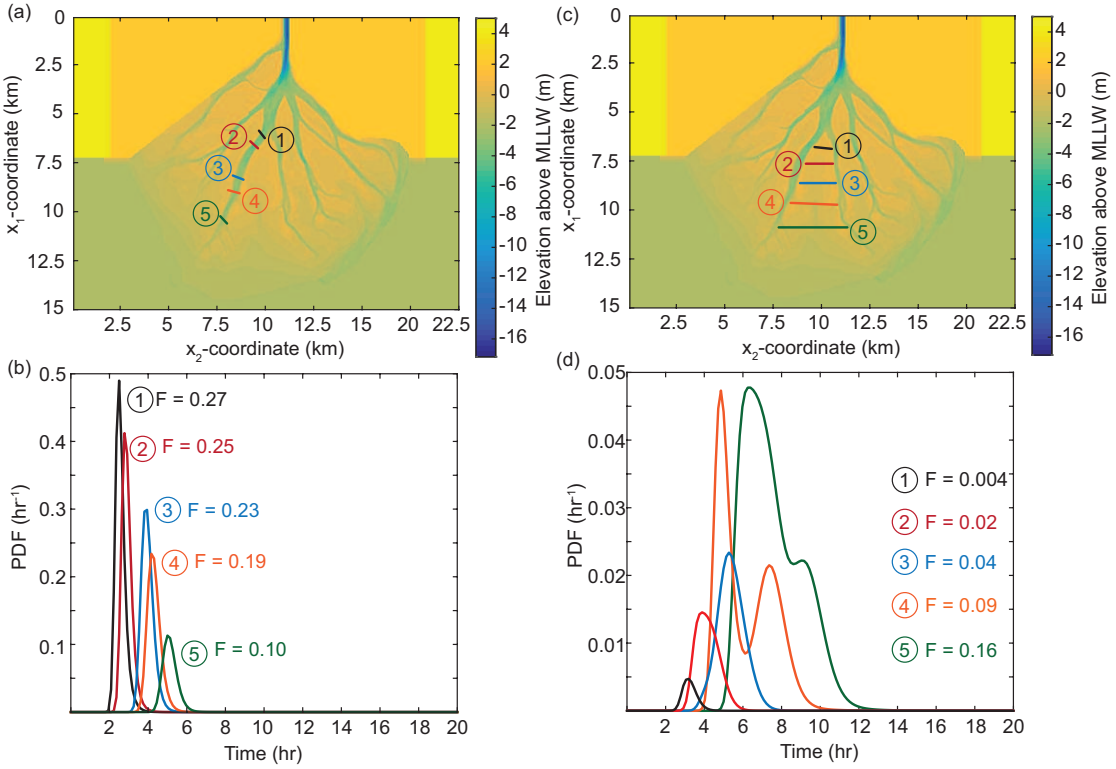

Figure 5.13: Summary of the marginal PDFs of the RTD for Gadwall Pass for the river-only model. (a) Locations of the transects along Gadwall Pass. (b) The marginal PDFs for each location in (a). (c) Same as (a) but for Tim Island. (d) Same as (b) but for Tim Island. The total mass flux passing through each transect (F) is along given. Note the change in y-axis from (b) to (d).

tracer fluxed through the island increased with increasing distance downstream, owing to the channel-island hydrological connectivity via overbank and secondary channel flow. The presence of a large secondary channel produced interesting flow dynamics within the island. The peak for transect 4 on Tim Island occurs slightly before that of transect 3 (Figure 5.13d). This is because a large secondary channel carrying significant flow (see Figure 5.9) was present on the left side of Tim Island between transect 3 and 4. This secondary channel brought fast-moving tracer mass that manifested in the first peak of the bimodal transect 4 RTD. The tracer mass

propagating through transect 3 entered the island slowly via overbank flow, thus the peak of transect 3 lags behind that of 4. The second modal peak in the transect 4 RTD likely comprised the flow through transect 3 and the overbank flow between transects 3 and 4.The large first peak at transect 4 was translated downstream to a peak of similar magnitude at transect 5, where $F = 0.16$ (Figure 5.13). Tim Island received 16% of the total flow entering the WLD due to the significant hydrological connectivity with the adjacent channels. In general, the local RTDs of the channels and islands behave similarly to the case study at Gadwall Pass and Tim Island presented here.

In general, islands acted to increase the dispersion of flow and RTD within the delta. As water moved down the delta, much of the flow was allocated to the interdistributary islands, which caused an increase in F within the islands moving downstream. The channels generally behaved as plug-flow-like systems, in which dispersion was very limited. However, water slowed when it entered the islands and direction change experienced by parcels of water entering the island likely contribute to the increased dispersion associated with the island marginal PDFs (Figure 5.13d). The relatively large dispersion associated with the Tim Island PDFs are also likely associated with the spatial distribution of velocities within the island interior, where the margins of the island experience relatively low velocities compared to the higher-velocity flow along the interdistributary trough [*Shaw et al.*, 2016]. The spatial distribution of RTD within a river delta has important implications for nutrient removal and ecological processes. The relatively low velocities within the islands increase the local RTD, which can enhance nutrient removal [*Lane et al.*, 2004; *Yu et al.*, 2006; *Rivera-Monroy et al.*, 2010].

5.5 Conclusions

In this study, we quantified the flow partitioning, hydrological connectivity, and the water residence time distribution (RTD) at Wax Lake Delta (WLD) in coastal Louisiana. We used boat-mounted acoustic Doppler current profiler measurements of discharge in the major distributary channels at WLD coupled with a two-dimensional hydrodynamic model to quantify the flow partitioning. The RTD was computed by modeling the propagation of a diffusive tracer within the WLD network. We find that the fractional flow partitioning at the network scale is not significantly influenced by the spring-neap nor semidiurnal tidal cycles at WLD. Nearly 55% of the discharge entering the WLD was found to exit the system via the interdistributary islands, which is in agreement with previous studies. Tides had a limited effect on the flow partitioning through the distributary channels. The median water residence time for the WLD under a river-only forcing was found to be 8.9 hours. The median residence time increased to 9.0 and 9.5 hrs for the neap and spring tide cases, respectively. Tides also increased the dispersion of the RTD, due to flow reversals and the flushing out of water by the tidal prism. This study provides the first detailed estimate of RTD in a coastal river delta accounting for the contributions to RTD from distinct system components (i.e., distributary channels and interdistributary islands).

Chapter 6: Conclusions and Future Perspective

6.1 Conclusions

River deltas are composed of distributary channels and interdistributary islands. Previous to this dissertation, deltaic channels and islands had been studied in isolation at different spatial and temporal scales. This dissertation identifies the importance of hydrological connectivity and links for the first time coupled channel-island processes in river deltas. The results presented in this dissertation advance our understanding of the morphological and ecological evolution of river deltas, which has significant implications for the design and management of coastal restoration projects. Below I address the research questions posed in Chapter 1 and discuss the scientific contributions of this work. I also include avenues of future research that would advance the topics covered in this dissertation.

How is water partitioned among channels and islands in a river delta network?

Hydrological connectivity refers to the transport of water, sediment, and nutrients through an ecosystem [*Bracken et al.*, 2013]. In river deltas, water, sediment, and nutrients pass through a network of distributary channels and interdistributary islands. The studies presented in this dissertation show that the interdistributary islands receive a significant percentage of the water discharge entering a natural, prograding river delta. This discovery of significant channel-island hydrological connectivity leads to interesting insights into the functioning and evolution of river

deltas, contributes to the growing body of literature on hydrological connectivity [e.g., *Bracken et al.*, 2013; *Fryirs*, 2013], and addresses the importance of analyzing connectivity in coastal systems.

Chapter 3 focused on characterizing and quantifying channel-island hydrological connectivity at Wax Lake Delta (WLD) in coastal Louisiana. Using discharge measurements taken with an acoustic Doppler current profiler, I quantified the partitioning of water from a distributary channel to the surrounding islands (23–54%) at WLD and identified the importance of deltaic islands in routing of water through and within the delta network. I coupled these measurements with a dye tracer study within a distributary island, and found that water travel times significantly increase when water is routed to the island interiors. These measurements laid the groundwork for the development of a conceptual framework for hydrological connectivity in river deltas, in which I identified elements of structural and process-based connectivity for coastal river deltas. Within the framework, the channel-island hydrological connectivity manifests itself via overbank flow and secondary channels that connect the distributary channels to the island interiors. Tides modulate the flow directions within secondary channels, influencing the hydrological connectivity between the distributary channels and the islands. Travel times within the deltaic islands are relatively long relative to their channel counterparts, owing to flow reversals due to tides and wind, and transient storage within vegetation patches. In Chapter 5, I used numerical modeling to support the measurements at WLD, and found that nearly 55% of the flow enters the islands for the entire WLD network.

The groundwater component of hydrological connectivity was not addressed in this dissertation. Fluctuations in water level due to tides and storms can mod-

ulate the groundwater flow between distributary channels and interdistributary islands [*O'Connor and Moffett*, 2015]. Recent numerical modeling experiments suggest that much of the water entering a distributary network passes through the hyporheic zone, which has implications for hydrological connectivity, residence times distributions, and biochemical processes [*Sawyer et al.*, 2015]. Further work should address the connectivity between the surface water and groundwater systems in river deltas to fully characterize river delta hydrological connectivity.

How does the hydrological connectivity between delta channels and islands influence channel-island hydraulics, water residence time distributions, and nitrate removal? What are the environmental controls on hydrological connectivity in river deltas?

The hydrological connectivity between distributary channels and deltaic islands exerts strong controls on the water residence time distributions (RTD) and, subsequently, nitrate removal. To formalize the hydrological connectivity framework, I analyzed the environmental controls on hydrological connectivity, channel-island hydraulics, water residence times, and nitrate removal within a channel-island complex using numerical modeling in Chapter 4. I found that hydraulic roughness due to vegetation within the island interiors is a primary control on the hydrological connectivity in a channel-island complex. Subsequently, RTD is strongly influenced by the amount of water entering the island interiors and the hydraulic roughness of the island. Changes in river discharge did not significantly alter the fraction of water exchanged between the channel and islands, likely because water levels in backwater zones are relatively insensitive to changes in river discharge [*Chatanantavet et al.*, 2012]. Tides acted to significantly lengthen the RTD, but

had a limited effect on the fraction of water exchanged between the channel and the islands. I coupled the modeled residence time distributions with a simple model to estimate nitrate removal, and found the fractional nitrate removal to be ∼0–87% depending on river discharge, tides, and hydraulic roughness. The modeled nitrate removals compare well with those estimated from field work.

In Chapter 4, it was found that hydrological connectivity is controlled by the relative hydraulic roughness between the channel and island interiors. Increasing roughness causes a decrease in the exchange between the channel and the island, which localizes flow in the channel and increases velocities. Accordingly, low relative roughness enhances channel-island hydrological connectivity, which can cause flow deceleration within the channel. This result has important implications for the morphological evolution of river deltas. Vegetation in tidal marshes can cause erosion in neighboring channels [*Bouma et al.*, 2007; *Temmerman et al.*, 2007]. Channel shallowing due to adverse slopes in river deltas can cause local acceleration of the flow causing erosion of distributary channels [*Shaw et al.*, 2016], but hydrological connectivity between the channel and the island can cause decreases in the channel velocity. In Chapter 5, tides were shown to modulate the velocity within a secondary channel, leading to highly localized rapid flows during low tide and spatially uniform, relatively slow flows during high tide. The tidal modulation of flow velocities in secondary channels likely plays a role in whether or not these channels extend by erosion or fill via deposition. The controls on hydrological connectivity identified and quantified in this dissertation improve the understanding of the relationships between off-channel and in-channel hydraulics that influence delta evolution.

This dissertation used a uniform roughness to parameterize increased drag

within vegetation. However, since the spatial distribution of vegetation patches significantly alters flow velocities and patterns [*Vandenbruwaene et al.*, 2011], the spatial heterogeneity in vegetation patches likely plays a key role in hydrological connectivity in river deltas. This notion should be addressed in future studies.

The role of hydrological connectivity in delta RTD is important for predicting the environmental impacts of coastal restoration projects. River diversions will alter RTD and nutrient transport in their receiving basins, which can have significant ecological effects [*Rivera-Monroy et al.*, 2010]. The coupled field and modeling study I presented in Chapter 4 suggests that quantifying RTD is essential for predicting nitrate removal at the channel-island complex scale, which has been suggested by other studies [e.g., *Yu et al.*, 2006]. Estimates of RTD are lacking in coastal Louisiana [*Rivera-Monroy et al.*, 2010] and this dissertation provides first estimates of RTD at the channel-island and network scales. Additionally, this dissertation also provides the first analysis of how RTD varies among distinct system components (i.e., the channels and the islands), which is important because nutrient removal processes are likely to be more efficient within the wetlands of the deltaic islands. This dissertation focused on a detailed analysis of hydrological connectivity and RTD, but used a very simple model to quantify nitrate removal. Further work should more formally address nitrate removal processes.

How does the structure of the delta network influence network-scale flow partitioning and water residence time distributions at Wax Lake Delta? Do tides influence the flow partitioning?

Most studies of flow partitioning are focused on single bifurcations. In Chapter 5, I used numerical modeling and field measurements to assess the network-scale flow

partitioning and RTDs at WLD. The modeled results compared well with the flow measurements from WLD. I found that tides had little effect on the fractional allocation of water through the delta network and the RTD is tied to the structure of the distributary channel network and channel-island hydrological connectivity. Previously, estimates of RTD in coastal Louisiana were lacking and there remained the question of how the RTDs of distinct system components influence the RTD of the large-scale system [*Rivera-Monroy et al.*, 2010]. This dissertation provides the first detailed estimate of RTD in a coastal river delta incorporating the contributions from distinct system components (i.e., channels and islands), which provides an important first step in evaluating the nutrient removal capacity of coastal river deltas and engineered river diversions.

Bibliography

Ali, G. A., and A. G. Roy (2009), Revisiting hydrologic sampling strategies for an accurate assessment of hydrologic connectivity in humid temperate systems, *Geography Compass*, *3*(1), 350–374, doi:10.1111/j.1749-8198.2008.00180.x.

Allen, Y., B. Couvillion, and J. Barras (2011), Using multitemporal remote sensing imagery and inundation measures to improve land change estimates in coastal wetlands, *Estuaries Coasts*, *34*(1), 190–200, doi:10.1007/s12237-011-9437-z.

Allison, M. A., and E. A. Meselhe (2010), The use of large water and sediment diversions in the lower Mississippi River (Louisiana) for coastal restoration, *Journal of Hydrology*, *387*(34), 346 – 360, doi:http://dx.doi.org/10.1016/j.jhydrol.2010.04.001.

Baptist, M., V. Babovic, J. R. Uthurburu, M. Keijzer, R. Uittenbogaard, A. Mynett, and A. Verwey (2007), On inducing equations for vegetation resistance, *Journal of Hydraulic Research*, *45*(4), 435–450, doi:10.1080/00221686.2007.9521778.

Barbier, E. B., I. Y. Georgiou, B. Enchelmeyer, and D. J. Reed (2013), The value

of wetlands in protecting southeast Louisiana from hurricane storm surges, *PLoS ONE*, *8*(3), e58715, doi:10.1371/journal.pone.0058715.

Batker, D., I. de la Torre, R. Costanze, P. Sweeden, J. D. Jr, R. Bourmans, and K. Bagstad (2010), Gaining ground: Wetlands, hurricanes and the economy: The value of restoring the Mississippi River Delta, *Technical report*, Earth Economics, Tacoma, WA.

Bertoldi, W., and M. Tubino (2007), River bifurcations: Experimental observations on equilibrium configurations, *Water Resour. Res.*, *36*, W10437, doi:10.1029/2007WR005907.

Boesch, D. F., M. N. Josselyn, A. J. Mehta, J. T. Morris, W. K. Nuttle, C. A. Simenstad, and D. J. P. Swift (1994), Scientific assessment of coastal wetland loss, restoration and management in Louisiana, *J. Coastal Res.*, (Special Issue No. 20), 1–103.

Bolla Pittaluga, M., R. Repetto, and M. Tubino (2003), Channel bifurcation in braided rivers: Equilibrium configurations and stability, *Water Resour. Res.*, *39*, 1046, doi:10.1029/2001WR001112.

Bornette, G., C. Amoros, and N. Lamouroux (1998), Aquatic plant diversity in riverine wetlands: the role of connectivity, *Freshwater Biol.*, *39*(2), 267–283, doi:10.1046/j.1365-2427.1998.00273.x.

Bouma, T., L. van Duren, S. Temmerman, T. Claverie, A. Blanco-Garcia, T. Ysebaert, and P. Herman (2007), Spatial flow and sedimentation patterns within patches of epibenthic structures: Combining field, flume and modelling exper-

iments, *Continental Shelf Research*, *27*(8), 1020 – 1045, doi:http://dx.doi.org/10.1016/j.csr.2005.12.019.

Bowden, W. B. (1987), The biogeochemistry of nitrogen in freshwater wetlands, *Biogeochemistry*, *4*(3), 313–348, doi:10.1007/BF02187373.

Boyer, E. W., R. W. Howarth, J. N. Galloway, F. J. Dentener, P. A. Green, and C. J. Vörösmarty (2006), Riverine nitrogen export from the continents to the coasts, *Global Biogeochem. Cy.*, *20*(1), doi:10.1029/2005GB002537.

Bracken, L., J. Wainwright, G. Ali, D. Tetzlaff, M. Smith, S. Reaney, and A. Roy (2013), Concepts of hydrological connectivity: Research approaches, pathways and future agendas, *Earth Sci. Rev.*, *119*, 17–34, doi:http://dx.doi.org/10.1016/j.earscirev.2013.02.001.

Bracken, L. J., and J. Croke (2007), The concept of hydrological connectivity and its contribution to understanding runoff-dominated geomorphic systems, *Hydrol. Process.*, *21*(13), 1749–1763, doi:10.1002/hyp.6313.

Buschman, F. A., A. J. F. Hoitink, M. van der Vegt, and P. Hoekstra (2010), Subtidal flow division at a shallow tidal junction, *Water Resour. Res.*, *46*(12), 1459–1472, doi:10.1029/2010WR009266.

Buschman, F. A., M. van der Vegt, A. J. F. Hoitink, and P. Hoekstra (2013), Water and suspended sediment division at a stratified tidal junction, *J. Geophys. Res.: Oceans*, *118*(3), 1459–1472, doi:10.1002/jgrc.20124.

Carle, M. V., C. E. Sasser, and H. H. Roberts (2013), Accretion and vegetation community change in the Wax Lake Delta following the historic

2011 Mississippi River flood, *J. Coastal Res.*, *31*(3), 569 – 587, doi:10.2112/JCOASTRES-D-13-00109.1.

Carvajal, C., R. Steel, and A. Petter (2009), Sediment supply: The main driver of shelf-margin growth, *Earth-Sci. Rev.*, *96*(4), 221 – 248, doi:http://dx.doi.org/10.1016/j.earscirev.2009.06.008.

Castro, M., C. Driscoll, T. Jordan, W. Reay, and W. Boynton (2003), Sources of nitrogen to estuaries of the United States, *Estuaries*, *26*(3), 803–814, doi:10.1007/BF02711991.

Casulli, V., and E. Cattani (1994), Stability, accuracy and efficiency of a semi-implicit method for three-dimensional shallow water flow, *Computers & Mathematics with Applications*, *27*(4), 99–112.

Casulli, V., and R. T. Cheng (1992), Semi-implicit finite difference methods for three-dimensional shallow water flow, *International Journal for numerical methods in fluids*, *15*(6), 629–648.

Chatanantavet, P., M. P. Lamb, and J. A. Nittrouer (2012), Backwater controls of avulsion location on deltas, *Geophys. Res. Lett.*, *39*(1), L01402, doi:10.1029/2011GL050197.

Costanza, R., O. Prez-Maqueo, M. L. Martinez, P. Sutton, S. J. Anderson, and K. Mulder (2008), The value of coastal wetlands for hurricane protection, *AMBIO*, *37*(4), 241–248.

Day, G., W. E. Dietrich, J. C. Rowland, and A. Marshall (2008), The depositional

web on the floodplain of the Fly River, Papua New Guinea, *J. Geophys. Res.: Earth Surf.*, *113*(F1), doi:10.1029/2006JF000622.

Day Jr., J., L. Britsch, S. Hawes, G. Shaffer, D. Reed, and D. Cahoon (2000), Pattern and process of land loss in the Mississippi Delta: A spatial and temporal analysis of wetland habitat change, *Estuaries*, *23*(4), 425–438, doi: 10.2307/1353136.

Day Jr., J., D. Boesch, E. Clairain, G. Kemp, S. Laska, W. Mitsch, K. Orth, H. Mashriqui, D. Reed, L. Shabman, C. Simenstad, B. Streever, R. Twilley, C. Watson, J. Wells, and D. Whigham (2007), Restoration of the Mississippi Delta: Lessons from Hurricanes Katrina and Rita, *Science*, *315*, 1679–1684, doi:10.1126/science.1137030.

DeLaune, R., A. Jugsujinda, J. West, C. Johnson, and M. Kongchum (2005), A screening of the capacity of Louisiana freshwater wetlands to process nitrate in diverted Mississippi River water, *Ecol. Eng.*, *25*(4), 315–321, doi:http://dx.doi.org/10.1016/j.ecoleng.2005.06.001.

Dettmann, E. H. (2001), Effect of water residence time on annual export and denitrification of nitrogen in estuaries: A model analysis, *Estuaries*, *24*(4), 481–490, doi:10.2307/1353250.

Diaz, R. J., and R. Rosenberg (2008), Spreading dead zones and consequences for marine ecosystems, *Science*, *321*(5891), 926–929, doi:10.1126/science.1156401.

Dunne, T., L. A. K. Mertes, R. H. Meade, J. E. Richey, and B. R. Forsberg (1998), Exchanges of sediment between the flood plain and channel of the Amazon River

in Brazil, *Geol. Soc. Am. Bull.*, *110*(4), 450–467, doi:10.1130/0016-7606(1998)110⟨0450:EOSBTF⟩2.3.CO;2.

Edmonds, D., C. Paola, D. Hoyal, and B. Sheets (2011a), Quantitative metrics that describe river deltas and their channel networks, *J. Geophys. Res.: Earth Surf.*, *116*, F04022, doi:10.1029/2010JF001955.

Edmonds, D., J. B. Shaw, and D. Mohrig (2011b), Topset-dominated deltas: A new model for river delta stratigraphy, *Geology*, *39*(12), 1175–1178, doi:10.1130/G32358.1.

Edmonds, D. A. (2012), Stability of backwater-influenced river bifurcations: A study of the Mississippi-Atchafalaya system, *Geophys. Res. Lett.*, *39*(8), doi:10.1029/2012GL051125.

Edmonds, D. A., and R. L. Slingerland (2007), Mechanics of river mouth bar formation: Implications for the morphodynamics of delta distributary networks, *J. Geophys. Res.: Earth Surf.*, *112*(F2), F02034, doi:10.1029/2006JF000574.

Ericson, J. P., C. J. Vrsmarty, S. L. Dingman, L. G. Ward, and M. Meybeck (2006), Effective sea-level rise and deltas: Causes of change and human dimension implications, *Global Planet. Change*, *50*(12), 63 – 82, doi:http://dx.doi.org/10.1016/j.gloplacha.2005.07.004.

Erler, D. V., B. D. Eyre, and L. Davison (2008), The contribution of anammox and denitrification to sediment N2 production in a surface flow constructed wetland, *Environmental Science & Technology*, *42*(24), 9144–9150, doi:10.1021/es801175t.

Falcini, F., N. S. Khan, L. macelloni, B. P. Horton, C. B. Lutken, K. L. McKee, R. Santoleri, C. Li, G. Volpe, M. DÉmidio, A. Salusti, and D. J. Jerolmack (2012), Linking the historic 2011 Mississippi River flood to coastal wetland sedimentation, *Nature Geosci*, *5*(11), 803–807, doi:http://dx.doi.org/10.1038/ngeo1615.

Fisk, H. (1952), Geological investigation of the Atchafalaya Basin and the problem of Mississippi River diversion, U.S. Army Corps. of Engineers, Mississippi River Commission, Vicksburg, Mississippi.

Fryirs, K. (2013), (Dis)connectivity in catchment sediment cascades: a fresh look at the sediment delivery problem, *Earth Surf. Process. Land.*, *38*(1), 30–46, doi:10.1002/esp.3242.

Fryirs, K. A., G. J. Brierley, N. J. Preston, and J. Spencer (2007), Catchment-scale (dis)connectivity in sediment flux in the upper Hunter catchment, New South Wales, Australia, *Geomorphology*, *84*(34), 297 – 316, doi:http://dx.doi.org/10.1016/j.geomorph.2006.01.044.

Gagliano, S., K. Meyer-Arendt, and K. Wicker (1984), Land loss in the Mississippi River deltaic plain, *Trans. - Gulf Coast Assoc. Geol. Soc.*, *31*, 295–300.

Geleynse, N., M. Hiatt, H. Sangireddy, and P. Passalacqua (2015), Identifying environmental controls on the shoreline of a natural river delta, *J. Geophys. Res.: Earth Surf.*, *120*(5), 877–893, doi:10.1002/2014JF003408.

Gomez, J. D., J. L. Wilson, and M. B. Cardenas (2012), Residence time distributions in sinuosity-driven hyporheic zones and their biogeochemical effects, *Water Resour. Res.*, *48*(9), doi:10.1029/2012WR012180.

Grace, S. F. (1932), The principal diurnal constituent of tidal motion in the Gulf of Mexico, *Geophysical Supplements to the Monthly Notices of the Royal Astronomical Society*, *3*(2), 70–83.

Gross, E. S., L. Bonaventura, and G. Rosatti (2002), Consistency with continuity in conservative advection schemes for free-surface models, *International Journal for Numerical Methods in Fluids*, *38*(4), 307–327.

Hardy, R., S. Lane, and D. Yu (2011), Flow structure at an idealized bifurcation: a numerical experiment, *Earth Surf. Processes Landforms*, *36*, 2083–2096, doi: 10.1002/esp.2235.

Heisler, J., P. Glibert, J. Burkholder, D. Anderson, W. Cochlan, W. Dennison, Q. Dortch, C. Gobler, C. Heil, E. Humphries, A. Lewitus, R. Magnien, H. Marshall, K. Sellner, D. Stockwell, D. Stoecker, and M. Suddleson (2008), Eutrophication and harmful algal blooms: A scientific consensus, *Harmful Algae*, *8*(1), 3 – 13, doi:http://dx.doi.org/10.1016/j.hal.2008.08.006.

Henderson, F. (1966), *Open Channel Flow*, 522 pp., Macmillan, New York, NY.

Henry, K., and R. Twilley (2014), Nutrient biogeochemistry during the early stages of delta development in the Mississippi River deltaic plain, *Ecosystems*, *17*(2), 1–17, doi:10.1007/s10021-013-9727-3.

Hiatt, M., and P. Passalacqua (2015), Hydrological connectivity in river deltas: The first-order importance of channel-island exchange, *Water Resour. Res.*, *51*, 2264–2282, doi:10.1002/2014WR016149.

Hodges, B. R. (2004), Accuracy order of crank-nicolson discretization for hydrostatic free-surface flow, *Journal of Engineering Mechanics*, *130*(8), 904–910.

Hodges, B. R. (2014), A new approach to the local time stepping problem for scalar transport, *Ocean Model.*, *77*, 1 – 19, doi:http://dx.doi.org/10.1016/j.ocemod.2014.02.007.

Hodges, B. R., and F. J. Rueda (2008), Semi-implicit two-level predictor–corrector methods for non-linearly coupled, hydrostatic, barotropic/baroclinic flows, *International Journal of Computational Fluid Dynamics*, *22*(9), 593–607.

Hodges, B. R., J. Imberger, A. Saggio, and K. B. Winters (2000), Modeling basin-scale internal waves in a stratified lake, *Limnology and oceanography*, *45*(7), 1603–1620.

Howarth, R. W., R. Marino, J. Lane, and J. J. Cole (1988), Nitrogen fixation in freshwater, estuarine, and marine ecosystems. 1. Rates and importance, *Limnology and Oceanography*, *33*(4 part 2), 669–687, doi:10.4319/lo.1988.33.4part2.0669.

Hoyal, D., and B. Sheets (2009), Morphodynamic evolution of experimental cohesive deltas, *J. Geophys. Res.: Earth Surf.*, *88*, F02009, doi:10.1029/2007JF000882.

Hyfield, E. C., J. W. Day, J. E. Cable, and D. Justić (2008), The impacts of re-introducing Mississippi River water on the hydrologic budget and nutrient inputs of a deltaic estuary, *Ecol. Eng.*, *32*(4), 347 – 359, doi:http://dx.doi.org/10.1016/j.ecoleng.2007.12.009.

Jadhav, R. S., and S. G. Buchberger (1995), Effects of vegetation on flow through free water surface wetlands, *Ecological Engineering*, *5*(4), 481 – 496, doi:http://dx.doi.org/10.1016/0925-8574(95)00039-9.

Jerolmack, D., and J. Swenson (2007), Scaling relationships and evolution of distributary networks on wave-influenced deltas, *Geophys. Res. Lett.*, *34*, L23402, doi:10.1029/2007GL031823.

Kadlec, R. (1990), Overland flow in wetlands: Vegetation resistance, *Journal of Hydraulic Engineering*, *116*(5), 691–706, doi:10.1061/(ASCE)0733-9429(1990)116:5(691).

Keddy, P., D. Campbell, T. McFalls, G. Shaffer, R. Moreau, C. Dranguet, and R. Heleniak (2007), The wetlands of Lakes Pontchartrain and Maurepas: Past, present and future, *Environ. Rev.*, *15*(1), 43–77.

Kim, W., D. Mohrig, R. Twilley, C. Paola, and G. Parker (2009), Is it feasible to build new land in the Mississippi River Delta?, *EOS*, *90*(42), 373–374.

Kleinhans, M., and R. Hardy (2013), River bifurcations and avulsions, *Earth Surf. Processes Landforms*, *38*, 317–318, doi:10.1002/esp.3354.

Kleinhans, M., A. Wilburs, and W. ten Brinke (2007), Opposite hysteresis of sand and gravel transport upstream and downstream of a bifurcation during a flood in the River Rhine, the Netherlands, *Neth. J. Geosci.*, *86*, 273–285.

Kleinhans, M. G., R. I. Ferguson, S. N. Lane, and R. J. Hardy (2013), Splitting rivers at their seams: bifurcations and avulsion, *Earth Surface Processes and Landforms*, *38*(1), 47–61, doi:10.1002/esp.3268.

Kolker, A. S., M. D. Miner, and H. D. Weathers (2012), Depositional dynamics in a river diversion receiving basin: The case of the West Bay Mississippi River Diversion, *Estuar. Coast. Shelf Sci.*, *106*, 1–12, doi:http://dx.doi.org/10.1016/j.ecss.2012.04.005.

Lane, R., J. W. Day, and B. Thibodeaux (1999), Water quality analysis of a freshwater diversion at Caernarvon, Louisiana, *Estuaries*, *22*(2), 327–336, doi:10.2307/1352988.

Lane, R., H. Mashriqui, G. Kemp, J. Day, J. Day, and A. Hamilton (2003), Potential nitrate removal from a river diversion into a Mississippi delta forested wetland, *Ecol. Eng.*, *20*, 237–249, doi:10.1016/S0925-8574(03)00043-0.

Lane, R., C. Madden, J. Day, and D. Solet (2011), Hydrologic and nutrient dynamics of a coastal bay and wetland receiving discharge from the Atchafalaya River, *Hydrobiologia*, *658*, 55–66, doi:10.1007/s10750-010-0468-4.

Lane, R. R., J. W. Day, D. Justić, E. Reyes, B. Marx, J. N. Day, and E. Hyfield (2004), Changes in stoichiometric Si, N and P ratios of Mississippi River water diverted through coastal wetlands to the Gulf of Mexico, *Estuarine, Coastal and Shelf Science*, *60*(1), 1 – 10, doi:http://dx.doi.org/10.1016/j.ecss.2003.11.015.

Larsen, L., J. Choi, M. Nungesser, and J.W.Harvey (2012), Directional connectivity in hydrology and ecology, *Eco.l Appl.*, *22*, 2204–2220, doi:http://dx.doi.org/10.1890/11-1948.1.

Leonard, L. A., and A. L. Croft (2006), The effect of standing biomass on flow velocity and turbulence in Spartina alterniflora canopies, *Estuarine, Coastal and*

Shelf Science, *69*(34), 325 – 336, doi:http://dx.doi.org/10.1016/j.ecss.2006.05.004.

Leonardi, N., A. Canestrelli, T. Sun, and S. Fagherazzi (2013), Effect of tides on mouth bar morphology and hydrodynamics, *Journal of Geophysical Research: Oceans*, *118*(9), 4169–4183, doi:10.1002/jgrc.20302.

Liang, M., N. Geleynse, D. A. Edmonds, and P. Passalacqua (2015), A reduced-complexity model for river delta formation – Part 2: Assessment of the flow routing scheme, *Earth Surf. Dynam.*, *3*(1), 87–104, doi:10.5194/esurf-3-87-2015.

Louisiana Coastal Protection and Restoration Authority (2012), Louisiana's Comprehensive Master Plan for a Sustainable Coast, *Technical report*, The State of Louisiana, Baton Rouge, LA.

Luhar, M., J. Rominger, and H. Nepf (2008), Interaction between flow, transport and vegetation spatial structure, *Environmental Fluid Mechanics*, *8*(5), 423–439, doi:10.1007/s10652-008-9080-9.

Luketina, D. (1998), Simple tidal prism models revisited, *Estuar. Coast. Shelf Sci.*, *46*(1), 77 – 84, doi:http://dx.doi.org/10.1006/ecss.1997.0235.

Luu, T., J. Garnier, G. Billen, T. Le, J. Nemery, D. Orange, and L. Le (2012), N, P, Si budgets for the Red River Delta (northern Vietnam): how the delta affects river nutrient delivery to the sea, *Biogeochemistry*, *107*(1-3), 241–259, doi:10.1007/s10533-010-9549-8.

Marani, M., C. Da Lio, and A. D'Alpaos (2013), Vegetation engineers marsh mor-

phology through multiple competing stable states, *Proceedings of the National Academy of Sciences*, *110*(9), 3259–3263, doi:10.1073/pnas.1218327110.

Mariotti, G., F. Falcini, N. Geleynse, M. Guala, T. Sun, and S. Fagherazzi (2013), Sediment eddy diffusivity in meandering turbulent jets: Implications for levee formation at river mouths, *J. Geophys. Res.: Earth Surf.*, *118*(3), 1908–1920, doi:10.1002/jgrf.20134.

Meselhe, E. A., I. Georgiou, M. A. Allison, and J. A. McCorquodale (2012), Numerical modeling of hydrodynamics and sediment transport in lower mississippi at a proposed delta building diversion, *Journal of Hydrology*, *472473*, 340 – 354, doi:http://dx.doi.org/10.1016/j.jhydrol.2012.09.043.

Mitsch, W., and J. Gosselink (1993), *Wetlands*, 2nd ed., John Wiley and Sons, New York, NY.

Mitsch, W. J., J. W. Day, J. W. Gilliam, P. M. Groffman, D. L. Hey, G. W. Randall, and N. Wang (2001), Reducing nitrogen loading to the Gulf of Mexico from the Mississippi River Basin: Strategies to counter a persistent ecological problem, *BioScience*, *51*(5), 373–388, doi:10.1641/0006-3568(2001)051[0373:RNLTTG]2.0.CO;2.

Morisawa, M. (1985), Topologic properties of delta distributary networks, *Models in Geomorphology*, pp. 239–268.

Morton, R. A., N. A. Buster, and M. D. Krohn (2002), Subsurface controls on historical subsidence rates and associated wetland loss in southcentral Louisiana, *Gulf Coast Assoc. Geol. Soc. Trans.*, *52*(767).

Mueller, D., C. Wagner, M. Rehmel, K. Oberg, and F. Rainville (2013), Measuring discharge with acoustic Doppler current profilers from a moving boat (ver. 2.0, December 2013): US Geological Survey Techniques and Methods, book 3, chap. A22, p. 95, available at http://pubs.usgs.gov/tm3a22/.

Muto, T. (2001), Shoreline autoretreat substantiated in flume experiments, *J. Sed. Res.*, *71*(2), 246–254, doi:10.1306/091400710246.

Nardin, W., D. Edmonds, and S. Fagherazzi (2016), Influence of vegetation on spatial patterns of sediment deposition in deltaic islands during flood, *Advances in Water Resources*, doi:http://dx.doi.org/10.1016/j.advwatres.2016.01.001, in press.

Neill, C., and L. A. Deegan (1986), The effect of Mississippi River Delta lobe development on the habitat composition and diversity of Louisiana coastal wetlands, *Am. Midl. Nat.*, *116*(2), 296–303.

Nepf, H. M. (1999), Drag, turbulence, and diffusion in flow through emergent vegetation, *Water Resources Research*, *35*(2), 479–489, doi:10.1029/1998WR900069.

Nepf, H. M. (2012), Hydrodynamics of vegetated channels, *Journal of Hydraulic Research*, *50*(3), 262–279, doi:10.1080/00221686.2012.696559.

Nepf, H. M., and E. R. Vivoni (2000), Flow structure in depth-limited, vegetated flow, *Journal of Geophysical Research: Oceans*, *105*(C12), 28,547–28,557, doi:10.1029/2000JC900145.

Nittrouer, J. A., M. A. Allison, and R. Campanella (2008), Bedform transport

rates for the lowermost mississippi river, *J. Geophys. Res.: Earth Surf.*, *113*(F3), doi:10.1029/2007JF000795.

Nixon, S., J. Ammerman, L. Atkinson, V. Berounsky, G. Billen, W. Boicourt, W. Boynton, T. Church, D. Ditoro, R. Elmgren, J. Gabber, A. Giblin, R. Jahnke, N. Owens, M. Pilson, and S. Seitzinger (1996), The fate of nitrogen and phosphorus at the land-sea margin of the North Atlantic Ocean, *Biogeochemistry*, *35*, 141–180, doi:10.1007/BF02179826.

NOAA (2016), National Oceanic and Atmospheric Administration (NOAA) Tides and Currents, available online at http://tidesandcurrents.noaa.gov/ (Last accessed March 31, 2016).

Noe, G., C. Hupp, and N. Rybicki (2013), Hydrogeomorphology influences soil nitrogen and phosphorus mineralization in floodplain wetlands, *Ecosystems*, *16*(1), 75–94, doi:10.1007/s10021-012-9597-0.

O'Connor, M. T., and K. B. Moffett (2015), Groundwater dynamics and surface watergroundwater interactions in a prograding delta island, Louisiana, USA, *Journal of Hydrology*, *524*, 15 – 29, doi:http://dx.doi.org/10.1016/j.jhydrol.2015.02.017.

Ortiz, A. C., A. Ashton, and H. Nepf (2013), Mean and turbulent velocity fields near rigid and flexible plants and the implications for deposition, *Journal of Geophysical Research: Earth Surface*, *118*(4), 2585–2599, doi:10.1002/2013JF002858.

Paola, C., R. Twilley, D. Edmonds, W. Kim, D. Mohrig, G. Parker, E. Viparelli, and V. Voller (2011), Natural processes in delta restoration: Applica-

tion to the Mississippi Delta, *Ann. Rev. Mar. Sci.*, *3*, 67–91, doi:10.1146/annurev-marine-120709-142856.

Parker, G., and O. Sequeiros (2006), Large scale river morphodynamics: Application to the Mississippi delta, in *River flow 2006: Proceedings of the International Conference on Fluvial Hydraulics*, edited by R. Ferreira, E. Alves, J. Leal, and A. Carsodo, CRC Press, Lisbon, Portugal.

Passalacqua, P., S. Lanzoni, C. Paola, and A. Rinaldo (2013), Geomorphic signatures of deltaic processes and vegetation: The Ganges-Brahmaputra-Jamuna case study, *J. Geophys. Res. Earth Surf.*, *118*, 1838 – 1849, doi:10.1002/jgrf.20128.

Pethick, J., and J. D. Orford (2013), Rapid rise in effective sea-level in southwest Bangladesh: Its causes and contemporary rates, *Global Planet. Change*, *111*(0), 237 – 245, doi:http://dx.doi.org/10.1016/j.gloplacha.2013.09.019.

Pongruktham, O., and C. Ochs (2015), The rise and fall of the Lower Mississippi: effects of hydrologic connection on floodplain backwaters, *Hydrobiologia*, *742*(1), 169–183, doi:10.1007/s10750-014-1983-5.

Pringle, C. (2003), What is hydrologic connectivity and why is it ecologically important?, *Hydrol. Processes*, *17*(13), 2685–2689, doi:10.1002/hyp.5145.

Rabalais, N., R. Turner, D. Justić, Q. Dortch, W. W. Jr., and B. S. Gupta (1996), Nutrient changes in the Mississippi River and system responses on the adjacent continental shelf, *Estuaries*, *19*(2B), 386–407, doi:10.2307/1352458.

Rabalais, N., R. Turner, and W. Wiseman Jr. (2002a), Gulf of Mexico hypoxia,

a.k.a. The Dead Zone, *Ann. Rev. Ecol. Syst.*, *33*, 325–363, doi:10.1146/annurev.ecolsys.33.010802.150513.

Rabalais, N., R. Turner, B. S. Gupta, D. Boesch, P. Chapman, and M. Murrell (2007), Hypoxia in the Northern Gulf of Mexico: Does the science support the plan to reduce, mitigate, and control hypoxia?, *Estuaries Coasts*, *30*(5), 753–772, doi:10.1007/BF02841332.

Rabalais, N., R. Diaz, L. Levin, R. Turner, D. Gilbert, and J. Zhang (2010), Dynamics and distribution of natural and human-caused hypoxia, *Biogeosciences*, *7*, 585–619.

Rabalais, N. N., R. E. Turner, and D. Scavia (2002b), Beyond science into policy: Gulf of Mexico hypoxia and the Mississippi River, *BioScience*, *52*(2), 129–142.

Rabalais, N. N., R. E. Turner, Q. Dortch, D. Justić, V. J. Bierman, and W. J. Wiseman (2002c), Nutrient-enhanced productivity in the northern Gulf of Mexico: past, present and future, *Hydrobiologia*, *475*(1), 39–63, doi:10.1023/A:1020388503274.

Rivera-Monroy, V., P. Lenaker, R. Twilley, R. Delaune, C. Lindau, W. Nuttle, E. Habib, R. Fulwiler, and E. Castaneda-Moya (2010), Denitrification in coastal Louisiana: A spatial assessment and research needs, *J. Sea Res.*, *63*, 157–172, doi:10.1016/j.seares.2009.12.004.

Roberts, H., R. Cunningham, G. Kemp, and S. Majersky (1997), Evolutions of sedimentary architecture and surface morphology: Atchafalaya and Wax Lake Deltas, Louisiana (1973-1994), *Gulf Coast Assoc. Geol. Soci. Trans.*, *47*, 477–484.

Roberts, H., J. Coleman, S. Bentley, and N. Walker (2003), An embryonic major delta lobe: A new generation of delta studies in the Atchafalaya-Wax Lake Delta system, *Gulf Coast Assoc. Geol. Soci. Trans.*, *53*, 690–703.

Roberts, H. H. (1997), Dynamic changes of the holocene mississippi river delta plain: The delta cycle, *Journal of Coastal Research*, *13*(3), 605–627.

Roberts, J., and T. D. Roberts (1978), Use of the butterworth low-pass filter for oceanographic data, *J. Geophys. Res.: Oceans*, *83*(C11), 5510–5514, doi: 10.1029/JC083iC11p05510.

Rosenberg, R. (1985), EutrophicationThe future marine coastal nuisance?, *Mar. Pollut. Bull.*, *16*(6), 227 – 231, doi:http://dx.doi.org/10.1016/0025-326X(85) 90505-3.

Rowland, J. C., W. E. Dietrich, and M. T. Stacey (2010), Morphodynamics of subaqueous levee formation: Insights into river mouth morphologies arising from experiments, *J. Geophys. Res.: Earth Surf.*, *115*(F4), F04007, doi: 10.1029/2010JF001684.

Sassi, M., A. Hoitink, B. de Brye, B. Vermeulen, and E. Deleersnijder (2011), Tidal impact on the division of river discharge over distributary channels in the Mahakam Delta, *Ocean Dynam.*, *61*(12), 2211–2228, doi:10.1007/ s10236-011-0473-9.

Sassi, M. G., A. J. F. Hoitink, B. Vermeulen, and H. Hidayat (2013), Sediment discharge division at two tidally influenced river bifurcations, *Water Resour. Res.*, *49*(4), 2119–2134, doi:10.1002/wrcr.20216.

Sawyer, A. H., D. A. Edmonds, and D. Knights (2015), Surface water-groundwater connectivity in deltaic distributary channel networks, *Geophys. Res. Letters*, doi: 10.1002/2015GL066156.

Scavia, D., N. N. Rabalais, R. E. Turner, D. Justi, and W. J. Wiseman (2003), Predicting the response of Gulf of Mexico hypoxia to variations in Mississippi River nitrogen load, *Limnology and Oceanography*, *48*(3), 951–956, doi:10.4319/lo.2003.48.3.0951.

Shaw, J., and D. Mohrig (2014), The importance of erosion in distributary channel network growth, Wax Lake Delta, Louisiana, USA, *Geology*, *42*, 31–34, doi: 10.1130/G34751.1.

Shaw, J., D. Mohrig, and S. Whitman (2013), The morphology and evolution of channels on the Wax Lake Delta, Louisiana, USA, *J. Geophys. Res.: Earth Surf.*, *108*, doi:10.1002/jgrf.20123.

Shaw, J. B., D. Mohrig, and R. W. Wagner (2016), Flow patterns and morphology of a prograding river delta, *Journal of Geophysical Research: Earth Surface*, doi:10.1002/2015JF003570.

Slingerland, R., and N. Smith (1998), River avulsions and their deposits, *Annu. Rev. Earth Planet. Sci.*, *32*, 257–285, doi:10.1146/annurev.earth.32.101802.120201.

Smart, J., and V. Moruzzi (1972), Quantitative properties of delta channel networks, *Z. Geomorph.*, *16*(3), 283–300.

Smith, C. J., R. D. DeLaune, and W. H. Patrick (1985), Fate of riverine nitrate

entering an estuary: I. Denitrification and nitrogen burial, *Estuaries*, *8*(1), 15–21, doi:10.2307/1352117.

Smith, V. H. (2003), Eutrophication of freshwater and coastal marine ecosystems a global problem, *Environ. Sci. Pollut. Res.*, *10*(2), 126–139, doi:10.1065/espr2002.12.142.

Stelling, G., and M. Zijlema (2003), An accurate and efficient finite-difference algorithm for non-hydrostatic free-surface flow with application to wave propagation, *International Journal for Numerical Methods in Fluids*, *43*(1), 1–23.

Syvitski, J., and Y. Saito (2007), Morphodynamics of deltas under the influence of humans, *Global Planet. Change*, *57*, 261–282, doi:10.1016/j.gloplacha.2006.12.001.

Syvitski, J., A. Kettner, I. Overeem, E. Hutton, M. Hannon, G. Brakenridge, J. Day, C. Vorosmarty, Y. Saito, L. Giosan, and R. Nicholls (2009), Sinking deltas due to human activities, *Nat. Geosci.*, *2*, 681–686, doi:10.1038/ngeo629.

Syvitski, J. P., A. J. Kettner, A. Correggiari, and B. W. Nelson (2005), Distributary channels and their impact on sediment dispersal, *Marine Geol.*, *222223*, 75–94, doi:http://dx.doi.org/10.1016/j.margeo.2005.06.030.

Tejedor, A., A. Longjas, I. Zaliapin, and E. F. Georgiou (2014a), Delta channel networks: 1. A graph-theoretic approach for connectivity analysis and steady-state flux solutions, *Water Resour. Res.*, *this issue*.

Tejedor, A., A. Longjas, I. Zaliapin, and E. F. Georgiou (2014b), Delta channel

networks: 2. Metrics of topologic and dynamic complexity for delta comparison, physical inference and vulnerability assessment, *Water Resour. Res.*, *this issue*.

Temmerman, S., T. Bouma, J. Van de Koppel, D. Van der Wal, M. De Vries, and P. Herman (2007), Vegetation causes channel erosion in a tidal landscape, *Geology*, *35*(7), 631–634, doi:10.1130/G23502A.1.

Templet, P. H., and K. J. Meyer-Arendt (1998), Louisiana wetland loss: A regional water management approach to the problem, *Environmental Management*, *12*(2), 181–192, doi:10.1007/BF01873387.

Tessler, Z. D., C. J. Vörösmarty, M. Grossberg, I. Gladkova, H. Aizenman, J. P. M. Syvitski, and E. Foufoula-Georgiou (2015), Profiling risk and sustainability in coastal deltas of the world, *Science*, *349*(6248), 638–643, doi:10.1126/science.aab3574.

Tetzlaff, D., C. Soulsby, P. J. Bacon, A. F. Youngson, C. Gibbins, and I. A. Malcolm (2007), Connectivity between landscapes and riverscapes - a unifying theme in integrating hydrology and ecology in catchment science?, *Hydrol. Process.*, *21*(10), 1385–1389, doi:10.1002/hyp.6701.

Tockner, K., D. Pennetzdorfer, N. Reiner, F. Schiemer, and J. V. Ward (1999), Hydrological connectivity, and the exchange of organic matter and nutrients in a dynamic riverfloodplain system (Danube, Austria), *Freshwater Biol.*, *41*(3), 521–535, doi:10.1046/j.1365-2427.1999.00399.x.

Trigg, M. A., P. D. Bates, M. D. Wilson, G. Schumann, and C. Baugh (2012), Floodplain channel morphology and networks of the middle Amazon River, *Water Resour. Res.*, *48*(10), W10504, doi:10.1029/2012WR011888.

Turner, R., and M. Boyer (1997), Mississippi river diversions, coastal wetland restoration/creation and an economy of scale, *Ecol. Eng.*, *8*(2), 117 – 128, doi: http://dx.doi.org/10.1016/S0925-8574(97)00258-9.

Turner, R., and N. Rabalais (1994), Coastal eutrophication near the Mississippi River Delta, *Nature*, *368*, 619–621, doi:10.1038/368619a0.

Turner, R., N. Rabalais, and D. Justić (2006), Predicting summer hypoxia in the northern Gulf of Mexico: Riverine N, P, and Si loading, *Marine Poll. Bull.*, *52*(2), 139–148, doi:http://dx.doi.org/10.1016/j.marpolbul.2005.08.012.

Turner, R. E., N. N. Rabalais, and D. Justić (2008), Gulf of Mexico hypoxia: Alternate states and a legacy, *Environ. Sci. Technol.*, *42*(7), 2323–2327, doi: 10.1021/es071617k, pMID: 18504960.

Twilley, R. R., and V. Rivera-Monroy (2009), Sediment and nutrient tradeoffs in restoring mississippi river delta: Restoration vs eutrophication, *Journal of Contemporary Water Research & Education*, *141*(1), 39–44, doi:10.1111/j. 1936-704X.2009.00035.x.

USGS (2016), U.S. Geological Survey (USGS) water data for the nation, available online at http://waterdata.usgs.gov/nwis/ (last accessed February 20, 2016).

Vandenbruwaene, W., S. Temmerman, T. J. Bouma, P. C. Klaassen, M. B. de Vries, D. P. Callaghan, P. van Steeg, F. Dekker, L. A. van Duren, E. Martini, T. Balke, G. Biermans, J. Schoelynck, and P. Meire (2011), Flow interaction with dynamic vegetation patches: Implications for biogeomorphic evolution of a tidal landscape, *Journal of Geophysical Research: Earth Surface*, *116*(F1), doi:10.1029/2010JF001788.

Walling, D. (1983), The sediment delivery problem, *J. Hydrology*, *65*(13), 209 – 237, doi:http://dx.doi.org/10.1016/0022-1694(83)90217-2.

Walling, D. E., P. N. Owens, and G. J. Leeks (1998), The role of channel and floodplain storage in the suspended sediment budget of the River Ouse, Yorkshire, UK, *Geomorphology*, *22*(34), 225–242, doi:http://dx.doi.org/10.1016/S0169-555X(97)00086-X.

Wolinsky, M. A., D. A. Edmonds, J. Martin, and C. Paola (2010), Delta allometry: Growth laws for river deltas, *Geophysical Research Letters*, *37*(21), n/a–n/a, doi:10.1029/2010GL044592.

Wright, L. (1977), Sediment transport and deposition at river mouths: A synthesis, *Geol. Soc. Am. Bull.*, *88*, 857–868.

Yu, K., R. DeLaune, and P. Poeckx (2006), Direct measurement of denitrification activity in a Gulf coast freshwater marsh receiving diverted Mississippi River water, *Chemosphere*, *65*, 2449–2455, doi:10.1016/j.chemosphere.2006.04.046.

Zak, D. R., and D. F. Grigal (1991), Nitrogen mineralization, nitrification and denitrification in upland and wetland ecosystems, *Oecologia*, *88*(2), 189–196, doi:10.1007/BF00320810.

Zektser, I., and H. A. Loaiciga (1993), Groundwater fluxes in the global hydrologic cycle: past, present and future, *Journal of Hydrology*, *144*(14), 405 – 427, doi:http://dx.doi.org/10.1016/0022-1694(93)90182-9.

Zhang, J., D. Gilbert, A. J. Gooday, L. Levin, S. W. A. Naqvi, J. J. Middelburg, M. Scranton, W. Ekau, A. Peña, B. Dewitte, T. Oguz, P. M. S. Monteiro,

E. Urban, N. N. Rabalais, V. Ittekkot, W. M. Kemp, O. Ulloa, R. Elmgren, E. Escobar-Briones, and A. K. Van der Plas (2010), Natural and human-induced hypoxia and consequences for coastal areas: synthesis and future development, *Biogeosciences*, *7*(5), 1443–1467, doi:10.5194/bg-7-1443-2010.

Zolezzi, G., W. Bertoldi, and M. Tubino (2006), Morphological analysis and prediction of river bifurcations, in *Braided Rivers: Process, Deposits, Ecology and Management*, *Special Publication Number 36 of the International Association of Sedimentologists*, vol. 36, edited by G. Sambrock Smith, J. Best, C. Bristow, and G. Petts, pp. 233–256, Blackwell Publishing Ltd., Oxford, UK, doi: 10.1002/9781444304374.ch11.